Holistic and Adaptive Robotic Welding

Charalampos Loukas

Department of Electronic and Electrical Engineering

Centre for Ultrasonic Engineering

University of Strathclyde

A thesis submitted for the degree of

Doctor of Philosophy

July 2022

Copyright

This thesis is the result of the author's original research. It has been composed by the author and has not been previously submitted for examination which has led to the award of a degree.

The copyright of this thesis belongs to the author under the terms of the United Kingdom Copyright Acts as qualified by University of Strathclyde Regulation 3.50. Due acknowledgement must always be made of the use of any material contained in, or derived from, this thesis.

Signed:

Date: 07/09/22

Acknowledgements

Abstract

Welding is an integral process of the heavy-manufacturing sector, with the welding market projected to reach $28.66 billion by 2028, alongside an expected 60% global shortage of manual welders by 2025. The upcoming deficit of skilled labour and the need for increased production demand can be addressed by investigating, developing, and integrating automated welding solutions in the production line. The current level of automation in the welding sector is characterized by manual robot programming of welding paths, utilization of custom fixed welding cells and cumbersome allocation of welding parameters.

As such, the capability of the current automated welding solutions is limited to cope with highly customized parts, fixed user specifications, and low volume production, making Small to Medium Enterprises (SMEs) reluctant to adopt robotic welding technology. A viable future for manufacturing can be secured by introducing, sensor-enabled robotic welding systems which are able to realize flexibility and increased degree of adaption between jobs, ensuring repeatable high-quality weldments under minimum human input and supervision.

This thesis presents on novel research and a series of contributions to the field of automated robotic arc welding through the conceptualization, design, development, and deployment of a holistic and adaptive robotic welding system, demonstrating fully automated multi-pass welding for single-sided V-groove geometries. The proposed flexible robotic welding solution is underpinned by a novel real-time and purely sensor-driven motion module. The integration of a multi-pass welding system allows the

automated sequence and adaptive generation of the welding schedule and allocation of welding parameters, based on a novel cost-function concept with immediate effects on the direct automated robotic welding costs. The developed advancements of a user-initiated approach for dynamic localization of the specimen in the scene, generation of welding paths along with the adaption of the torch based on the welding configuration, enhance the flexibility of the system by eliminating programming overhead between tasks and minimizing human input. The developed technology demonstrator features automated and enhanced welding capabilities that can be applied with immediate application in nuclear, offshore and oil and gas sectors.

Contents

List of Figures

List of Tables

Abbreviations

CAD	Computer Aided Design
CAM	Computer Aided Manufacturing
CCD	Charged Coupled Device
CMOS	Complementary Metal-Oxide Semiconductor
cRIO	Compact Reconfigurable Input Output
CTWD	Contact Tip to Work Distance
CV	Constant Voltage
DLL	Dynamic Link Library
FCAW	Flux Cored Arc Welding
FOV	Field of View
FPS	Frames Per Second
FPGA	Field Programmable Gate Array
GenICam	Generic Interface for Cameras
GMAW	Gas Metal Arc Welding
GUI	Graphical User Interface
HAZ	Heat Affected Zone
HDR	High Dynamic Range
HVM	High Value Manufacturing
ICP	Iterative Closest Point

IBVS	Image Based Visual Servoing
KRC	Kuka Robot Controller
LC	Linear Controller
LTI	Liquid Testing Inspection
MAG	Metal Active Gas
MIG	Metal Inert Gas
MTI	Magnetic Testing Inspection
NDE	Non-Destructive Evaluation
NDT	Non-Destructive Testing
OLP	Offline Programming
OP	Online Programming
PAUT	Phased Array Ultrasonic Testing
PBVS	Position Based Visual Servoing
POC	Proof of Concept
QR	Quick Response
RGB	Red Green Blue
ROI	Region of Interest
ROInv	Return of Investment
RSI	Robot Sensor Interface
RTI	Radiography Testing Inspection
SAIC	Sensor Adaptive Input Controller
SAW	Submerged Arc Welding

SDK	Software Development Kit
TCP	Tool Centre Point
TIG	Tungsten Inert Gas
UDP	User Datagram Protocol
UT	Ultrasonic Testing
VS	Visual Servoing
VT	Visual Testing
WAAM	Wire Arc Additive Manufacturing
WPS	Welding Procedure Specification
XML	Extensible Markup Language

Chapter 1

Introduction

1.1. Context of Research

The manufacturing sector in the UK recorded product sales of £396.6 billion in 2019, which accounted for 45% of the total exports [1]. The transformation drivers behind this growth, which put the UK as the 9th largest manufacturer worldwide, can be found in the embracement of new technology and achieving greater innovation [2]. As welding is an integral aspect of heavy manufacturing, the scarcity of skilled labour due to a high volume of recent staff retirement and hazardous working conditions, is seen as the biggest challenge that the heavy engineering segment is facing since 1989 [2]. Moreover, the impact of the COVID-19 pandemic has been staggering in the supply chain, with rising inflation also putting manufacturing in a vulnerable position due to uncertainty in costs and demand.

It is estimated that in 2020 the global welding market was $20.23 billion and is projected to grow to $28.66 billion by 2028 [3]. In contrast, there is a predicted 60% global shortage in welding professionals between 2015 and 2025 where labour wages occupy the largest portion of manufacturing costs [4].

Therefore, to retain the UK at the forefront of manufacturing, ensuring it is globally competitive and meets the government's 2050 net-zero target [5], flexible automated solutions and technologies require to be researched and incorporated into the production line [3]. Adopting digital technologies and freeing up workers for more customized tasks can mitigate the upcoming deficit in the skills gap [2]. These technologies are shaped by the Industry 4.0 revolution [6,7], with the common characteristic of the integration of smart sensors in the production process to achieve systems interconnectivity for increased uptime [8].

Innovations in arc welding such as the integration of robotic welding, and replacing current tedious, repetitive and manual processes, are key factors driving automation in the welding sector [9]. Robotic welding systems often involve measuring and identifying the component to be welded, controlling the welding process and documenting the produced result [10]. Achieving operational excellence by performing high-quality repeatable welds is a key aim and robotic welding can decrease labour costs, minimize human exposure to hazardous conditions and decrease production time. Moreover, integrating emerging technological advancements such as cloud-based operation management and big data performance analysis for robotic welding systems can lead to efficient management of the manufacturing process and resources [11,12].

Despite the massive integration of robotic welding in High-Value Manufacturing (HVM) sectors, such as oil and gas, marine and automotive, these systems are often only viable and programmed to perform repetitive welding in customized cells [13]. As a result, the capability of the current automated welding systems is limited due to the need to meet the

demands for highly customized parts and user specifications [10,14]. Variable welding joint configurations, high tolerance requirements, misalignments during fabrication fitting and gap width variation, increase the complexity and adaption requirements for automated robotic welding systems. As such, SMEs owing to variable and low volume production, are still struggling to adopt robotic welding technology. In addition, the large initial capital investment for hardware procurement, software integration and maintenance, compared to manual welding equipment further restrains the growth of automated robotic welding [15].

Conversely, large companies can scale up quickly, to meet the balance between demand and output, but still, there is a need to ensure sufficient accommodation of the user requirements and justify the initial capitalization towards tangible Return of Investment (ROInv). Therefore, highly flexible systems are required that can adapt to the environment and to the welding process while still being user friendly. Following the advancements being made in Industry 4.0, the call for automated sensor-enabled robotic welding systems has become paramount.

In order to meet these goals, this thesis proposes the following developments related to sensory-guided robotic path programming and a sophisticated welding process adaption system for high-integrity weldments.

The integration of sensors to provide feedback to the robotic welding system and the operator before and during welding seeks to increase the production flexibility and degree of adaption to the welding process. Traditional robotic welding systems rely on human input to program the robotic welding path and allocate welding parameters, as the current

progress is not sufficient to cope with uncertainties in the welding surroundings. Intelligent path planning can be realized from sensors' input and hence, downtime between different welding tasks can be decreased, replacing current cumbersome programming methods [16] and the need for experienced robotic programmers on the production floor. To minimize human intervention in the robotic welding systems and move welders to more customized tasks, it must be ensured that there is a high degree of sophisticated programming to deliver adaptive path planning and real-time control of the welding process resulting in high-quality repeatable weldments.

The maturity of automated robotic welding and its wide adoption in industrial environments can be enabled by delivering increased reliability and improved lifecycle to the products. These requirements are determined by the intended service of the weldments and the presence of defects. The defects can decrease the lifetime of assets, adding further delay to the overall production process through rework or even leading to scrappage when failing to pass acceptance standards [17]. Digitization of the welding procedure in terms of providing an automated weld monitoring system can provide early in-process indication of defects during welding, applying pre-trained learning algorithms to compensate for deviations between ideal and non-ideal conditions [18,19].

Successful design, implementation and deployment of such technology can reduce human input before and during welding. This would be particularly advantageous for the welders since the nature of the welding work often requires welding in areas where human access is limited, ergonomically constrained or there is an associated risk of exposure to harmful substances and increased temperature [20]. Minimizing reliance on the human factor and

bringing forward the full automation of robotic welding systems can decrease the probability of injuries, increasing the health and safety standards in the manufacturing sector.

However, the previous does not remove the requirement for human oversight in the welding process. Skilled welders are essential to associate built experience with the overall welding process. The welder's know-how must be studied, translated, and programmed into automated robotic welding systems to act as an experienced welding technologist.

1.2. Problem Statement

As robotic welding is adopted in the welding sector to fulfil repeatable tasks, there is an increased need to introduce flexibility, reliability and ease between programming and execution. The current situation of an upcoming large deficit in human labour and low interest in the welding profession enhances the research aim from engineering organisations for the development and acquisition of smart robotic welding systems that can achieve high-quality repeatable welds for various welding configurations.

As an example, in organisations that operate in large shipyards where manufacturing processes takes place, automation of arc welding through deployment of automated welding solutions can serve the repetitive welding jobs and decrease the dependence of large organisations to rely on subcontractors of varying skillset.

Babcock International Group is a leading UK engineering organisation which serves as the industrial partner in this research project and have a proud history of bringing forward

and applying innovation in the land, aviation, nuclear and marine sector [21]. Through the large-scale marine engineering infrastructures that it owns, it can perform upgrades to almost 75% of the Royal Navy fleet including warships and nuclear submarines.

Each ship of the Royal Navy fleet after some years of active service must undergo a refit process, to survey and upgrade the hull structure, which based on the maturity level will require a different amount of welding. Type 23 refit projects to repair ageing frigates (seen in Figure 1.1), aim to extend the service of those assets [22]. The nature of the required repetitive and monotonous tasks that are needed to complete these upgrades lends itself to seeking and integrating automated solutions of robotic welding to aid welders and redistribute their workload among the various jobs.

Figure 1.1. Royal Navy warships undergo a refit process after some years of active service [22]

The development of a holistic and adaptive robotic welding system aligns with the maintenance procedure requirements during drydocking of warships and for projects similar to the Type 23 refits. A lot of repetitive multiple welding passes must take place manually, usually in tight spaces. Currently utilized manual welding processes are of low efficiency, with a minority of time being spent in welding. These welding configurations are often in the enclosed spaces of frigates and submarines. As can be seen in Figure 1.2 and Figure 1.3 which depict insert samples from a frigate, fixed electrical and mechanical infrastructure exists nearby to the welding joints which cannot be readily removed restricting the working volume. Owing to current working conditions with limited space for work and ergonomic difficulties adds more work shifts, where reliance on sub-contracted welders to supplement the workload can result in varying weld quality. Therefore, the use of a holistic robotic welding system to handle the more standard repetitive welding tasks can make skilled welders available for more complicated and creative tasks.
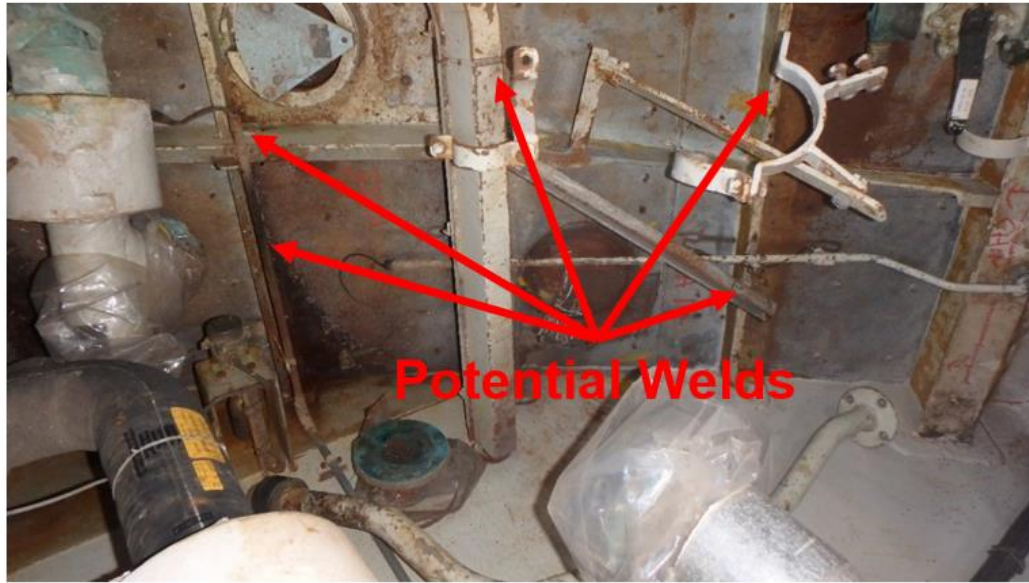
Figure 1.2. Enclosed space with potential welds in a frigate. The picture belongs to Babcock International PLC

Figure 1.3. Fixed electrical infrastructure cannot be removed totally, introducing further requirements for the use of a holistic automated welding system. The picture belongs to Babcock International PLC

The integration of automated robotic systems offers the potential to decrease safety risks related to injuries, exploiting the benefits of utilizing robotic arms for high positional accuracy, increased precision and overall accelerating the maintenance procedure.

Due to those conditions and further specifications from the industrial partner a series of research goals were generated that can be fulfilled by developing a holistic and sensor-enabled robotic welding system.

1.3. Research Goals

The research goals in this thesis are:

1. Establish the state-of-the-art in automated robotic welding in terms of robotic path planning, vision sensing and multi-pass planning.
2. Investigate the feasibility of a holistic robotic welding system.
3. Develop an adaptive sensor-enabled robotic motion module based on real-time positional corrections.
4. Develop an adaptive multi-pass welding system to serve the autonomous generation of welding schedule for single-sided V-groove geometries.
5. Develop algorithmic processes for autonomous localization of the welding specimen, adaption of the welding torch and generation of welding path.
6. Develop a fully autonomous robotic welding suite to serve as a transferable technology package for future scale robotic platforms.

1.4. Contributions to Knowledge

This thesis presents unique and novel contributions with direct academic and industry-focused merits, related to automated robotic arc welding. More specifically, this work has

focused on the investigation and development of a holistic and adaptive robotic arc welding system for automated multi-pass arc welding for single sided V-groove joints.

The two main critical elements that enabled the realisation of the proposed system, was the integration of a sensory-driven motion module for automated path and kinematics generation along with an offline multi-pass sequence planning strategy based on the geometric characteristics of the groove geometry. As a result, minimum downtime is spent (less than 3 min) between different welding tasks, removing the user from the requirement to plan manually or adjust the welding path based on CAD drawings. The adaption of the welding schedule per welding groove geometry following the operational plan eliminated the cumbersome and time-consuming task for an operator to manually allocate the welding parameters per welding pass. Moreover, the developed algorithmic advancements for a user-initiated workpiece localization and adaption of the welding process to each welding configuration achieved maximum heat concentration for all three degrees of orientation in (cartesian space), bringing forward features commonly applied in manual welding resulting in high-integrity weldments as verified through experimental trials (Chapters 4, 5).

The realization of such an arc welding system required the transformation of a commercial and small articulated arm to a welding robot able to fit with the small spaces found within frigates (Section 1.2). The custom-made bracket for the robotic arm made feasible to integrate a series of sensors (laser scanner, cameras) in such a compact way to drive the inspection of the welding joints and deployment of robotic arc welding. Moreover, to increase the flexibility of the robotic system a magnetic base was designed to mount the

robot in metallic surfaces close to the welding joints. Lastly, the electrical isolation of the sensitive electronics of the system and the welding base during welding was achieved through plastic tubes (Section 3.2.2).

The described technology was complemented by the development of a Graphical User Interface (GUI) (Section 3.3) consisting of different modalities (vision sensing, welding, robot motion) to allow the user to initiate, inspect and control the welding dynamics and robot kinematics by performing changes in real-time if needed. The developed software package can be integrated in different robotic arms; irrespective of size and manufacturer.

A novel sensor-enabled robotic motion module was developed for multi-axis robotic platforms. The full external control, generation, and deployment of kinematics in real-time were achieved through sensory input.

The following bullet points summarize the described novelty and critical contributions achieved within this thesis:

- An off-the-shelf articulated robotic arm was transformed into a holistic robotic welding system (Chapter 3).

- A novel sensor-enabled robotic motion module was developed for multi-axis robotic platforms. The full external control, generation, and deployment of kinematics in real-time were achieved through sensory input (Chapter 3).

- A novel and adaptive weld parameter and pass deposition multi-pass system was developed. It can accommodate the automatic generation of the welding schedule

based on the V-groove characteristics and on a novel cost function concept with direct savings in automated robotic welding costs (Chapter 4).

- Automatic localization of the welding specimen in combination with the autonomous adaption of the welding torch and compensation for human and vision sensing error was achieved for the first time. The developed algorithms lead to the generation of accurate welding paths and the extraction of geometric characteristics (Chapter 5).

- A novel robotic software suite was developed for automated welding as a transferable technology package, with immediate applicability in a variety of robotic platforms in terms of scale and manufacturer (Section 3.3).

1.5. Thesis Structure

Chapter 2 introduces the theoretical background, upon which this thesis is built, exploring the fundamentals of fusion welding in robotic welding, robotic path planning programming approaches, the use of vision sensing in robotic welding and the need for Non-Destructive Evaluation (NDE) of the weldments with a particular focus in Ultrasonic Testing (UT). Chapter 3 presents the transformation and the development of a holistic and modular robotic welding system which enables flexible robotic welding. A novel real-time motion control module is established, facilitating the sensor-guided motion for autonomous welding, and eliminating the need for manual robot programming.

The novel algorithmic system for adaptive weld path planning and pass sequencing based on a user-driven cost function concept is introduced and presented in Chapter 4. The

offline multi-pass welding schedule is generated based on the geometric characteristics of the joint geometry, achieving direct savings in automated robotic welding costs in terms of arc time, filler wire consumption and number of welding passes.

Chapter 5 presents the development of the algorithmic processes for user-initiated autonomous workpiece localization, the adaptation of the welding torch relative to the specimen's pose and the compensation of the introduced human and vision sensing error for accurate extraction of welding path and geometric characteristics. The autonomous sensory-driven approach was deployed and experimentally validated to showcase automated multi-pass robotic welding for single-sided V-grooves. Finally, Chapter 6 summarizes the undertaken work and concludes this thesis with future work and suggested future developments.

1.6. Lead Author Publications Arising From This Thesis

- **C. Loukas**, V. Williams, R. Jones, M. Vasilev, C.N. MacLeod, G. Dobie, J. Sibson, S.G. Pierce, A. Gachagan, A cost-function driven adaptive welding framework for multi-pass robotic welding, Journal of Manufacturing Processes. 67 (2021) 545–561. July 2021

- **C. Loukas**, V. Warner, R. Jones, C.N. MacLeod, M. Vasilev, E. Mohseni, G. Dobie, J. Sibson, S.G. Pierce, A. Gachagan, A sensory-driven approach towards automated robotic multi-pass arc welding (Journal of Materials and Design)

1.7. Co-Author Publications Arising From This Thesis

1.7.1. Journal Papers

- M. Vasilev, C.N. MacLeod, **C. Loukas**, Y. Javadi, R.K.W. Vithanage, D. Lines, E. Mohseni, S.G. Pierce, A. Gachagan, Sensor-Enabled Multi-Robot System for Automated Welding and In-Process Ultrasonic NDE, Sensors. 21 (2021) 5077.

- R. Zimermann, E. Mohseni, M. Vasilev, **C. Loukas**, R.K.W. Vithanage, C.N. Macleod, D. Lines, Y. Javadi, M.P. Espirindio E Silva, S. Fitzpatrick, S. Halavage, S. Mckegney, S.G. Pierce, S. Williams, J. Ding, Collaborative Robotic Wire + Arc Additive Manufacture and Sensor-Enabled In-Process Ultrasonic Non-Destructive Evaluation, Sensors. 22 (2022) 4203.

- R. McMillan, M. Tabatabaeipour, R. Hampson, **C. Loukas**, T. Zhao, R.S. Edwards, C. Macleod, G. Dobie, Characterization of EMAT Guided Wave Reflectivity on Welded Structures for use in Ranging, IEEE Sensors Journal. (2022) 1–1.

- E. Duernberger, C. MacLeod, D. Lines, C. Loukas, M. Vasilev, Adaptive optimisation of multi-aperture ultrasonic phased array imaging for increased inspection speeds of wind turbine blade composite panels, NDT & E International. 132 (2022) 102725.

- D.I. Lines, Y. Javadi, E. Mohseni, M. Vasilev, C.N. MacLeod, C. Mineo, R.W. Vithanage, Z. Qiu, R. Zimermann, **C. Loukas**, E. Foster, S.G. Pierce, A. Gachagan, A flexible robotic cell for in-process inspection of multi-pass welds,

Insight - Non-Destructive Testing and Condition Monitoring. 62 (2020) 526–532.

- R.K.W. Vithanage, E. Mohseni, D. Lines, **C. Loukas**, E. Foster, C.N. MacLeod, S.G. Pierce, A. Gachagan, J. Ding, S. Williams, Development of a phased array ultrasound roller probe for inspection of wire + arc additive manufactured components, Journal of Manufacturing Processes. 80 (2022) 765–774.

1.7.2. Conference Papers

- Y. Javadi, C. Macleod, D. Lines, M. Vasilev, E. Mohseni, E. Foster, Z. Qiu, R. Vithanage, R. Zimermann, **C. Loukas**, G. Pierce, A. Gachagan, In-process inspection of multi-pass robotic welding, Review of Progress in Quantitative Non-destructive Evaluation. (2019)
- D.I. Lines, Y. Javadi, E. Mohseni, M. Vasilev, C.N. MacLeod, R.W. Vithanage, Z. Qiu, R. Zimermann, **C. Loukas**, S.G. Pierce, A. Gachagan, Flexible robotic cell for in-process inspection of multi-pass welds, (NDT 2019) 12.

1.8. Other Output Arising From this Thesis

- Presentation in Advances in Welding and Additive Manufacturing Research Conference organised by the American Welding Society (2022) with title "Driving Towards Flexible and Automated Robotic Multi-Pass Arc Welding"
- Poster presentation for the Advanced Manufacturing and Material Annual Showcase Strategic Theme in University of Strathclyde (2019)

Chapter 2

Research Background

2.1. Welding Technology

Welding at its core is a highly dynamic joining process where two or more materials are brought together to be one part under increased heat, pressure or both [23]. Heat is employed which originates from a local source such as an electric arc, laser beam or plasma to melt the base material, and usually, a filler material of the same type as the parent material is added to the produced weld pool. When the weld pool solidifies, the Heat Affected Zone (HAZ) cools down to form the joint which can be characterized by high structural integrity and can approach or exceed the strength of the base material [24]. Welding as a manufacturing process has been essential since the last half of the nineteenth century when technological advancements such as the use of carbon arc to melt metals and experimentation with consumable metal electrodes gave space to the first US patent for welding in 1889 [24].

Among the different types of welding, arc welding has evolved for over 100 years [25]. The different types of arc welding can be categorized based on the electrode type that is utilized, which can be consumable or non-consumable [24]. Among the most common techniques, Gas Metal Arc Welding (GMAW) widely known as Metal Inert Gas (MIG)

and Metal Active Gas (MAG) utilize a consumable solid filler wire. The distinction between MIG and MAG originates from the shielding gas (inert or active) that is used to protect the metal from becoming contaminated or oxidized, ranging from pure Argon or combinations of Argon and CO_2. In addition, when the flux is contained inside the hollow core of the welding wire, the welding process is defined as Flux Cored Arc Welding (FCAW). During welding, the flux reacts to the high temperatures, releasing a protective gas to the weld pool, eliminating the need for shielding gas while achieving higher deposition rates due to increased current [24].

GMAW is suitable for both thin and thick sections resulting in high deposition rates and increased productivity [24–26]. The power source of these welders can be synergically controlled for a given gas mixture, wire material and diameter and in absolute wire feed speed or current mode, depending on which parameter the welder will control. The power source of the GMAW process is Constant Voltage (CV) regulated, meaning that the distance of the tip of the wire to the specimen is kept constant during welding and that is the arc length. The operator can vary the wire feed speed and the position of the wire to the joint configuration, while the welding equipment to achieve constant voltage output will re-adjust the wire extension to keep the arc length constant. A wide variety of metals can be welded, which range from carbon steels, low alloy steels, stainless, aluminium, copper, and nickel alloys. Figure 2.1 shows the molten weld pool that is formed due to the local source of heat that is employed to melt the parent and filler metal, surrounded by the shielding gas during GMAW welding.
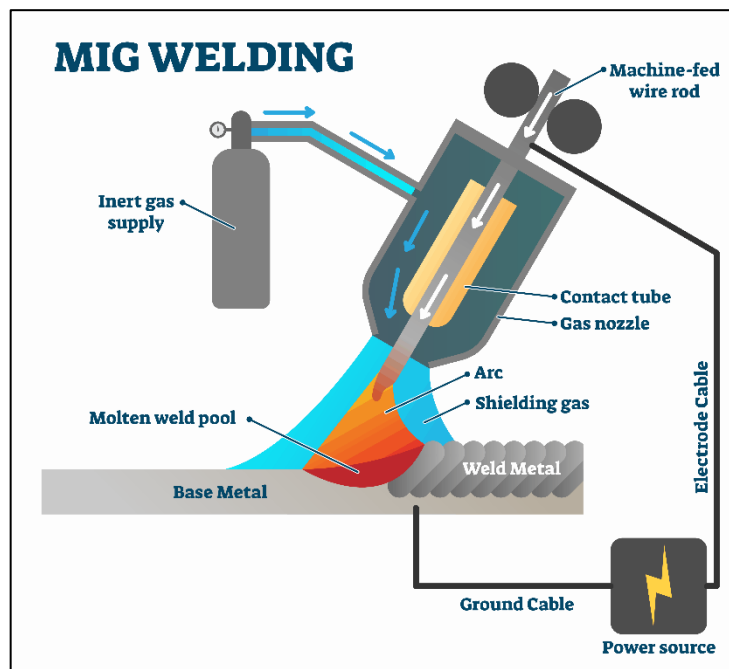
Figure 2.1. MIG/MAG arc welding process

Additionally, Submerged Arc Welding (SAW) utilize a consumable filler material, where an arc is submerged below a deposited flux shielding and is not usually visible during welding. SAW is an arc welding process known for increased deposition rates and arc currents in the range of 300 to 1000 Amps.

A different arc welding process which employs the heat input between a non-consumable tungsten electrode and the workpiece is the Gas Tungsten Arc Welding (GTAW). In that process, the molten weld pool is protected by an inert shielding gas such as Argon and Helium. Although the produced welds are clean with no slag inclusions, this method has a lower deposition rate compared to MIG/MAG [24,25]. Due to the industrial partner requirements and the welding procedures that used by their organization, here this work has focused on the use of MAG arc welding with a solid filler consumable wire.

2.1.1. Joint Configurations

In structures consisting of weldments, loads are distributed between the welds of the joints. The type of the selected joint geometry is determined by the geometric requirements of the assembly and the type of loading [24]. As can be seen in Figure 2.2 [27], the basic joint designs are summarized as butt, corner, edge, lap and tee joints. The selection of the joint type also aligns with the requirement for the least amount of deposited weld metal to meet the strength requirements for load distribution [24].
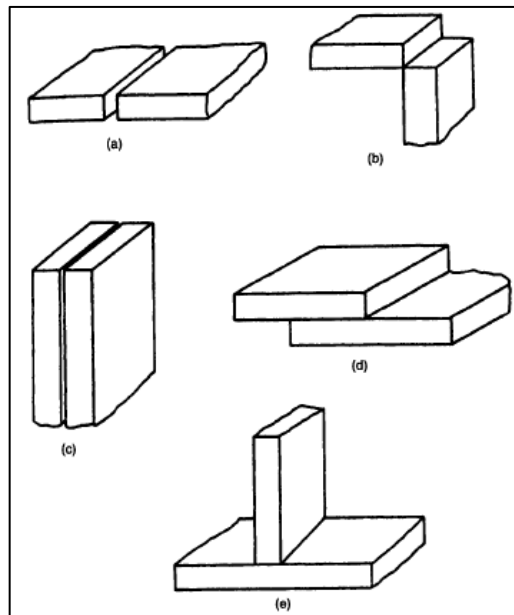
Figure 2.2. Five basic types of weld joint geometries. (a) butt joint, (b) corner joint, (c) edge joint, (d) lap joint and (e) tee joint

For thick butt joints, above 6-7 mm, the edges are mechanically prepared - machined, bevelled - to a particular geometry to provide adequate access for the welding torch and achieve even heat input flow and penetration between filler and parent metal [24,25]. These mechanically prepared geometries, which are shown in Figure 2.3 [24], can be

19

single-sided or double-sided for example with double V's, and single or double U's. In this work, due to the industrial partner requirements single-sided V-groove joints were used to validate automated robotic arc welding.
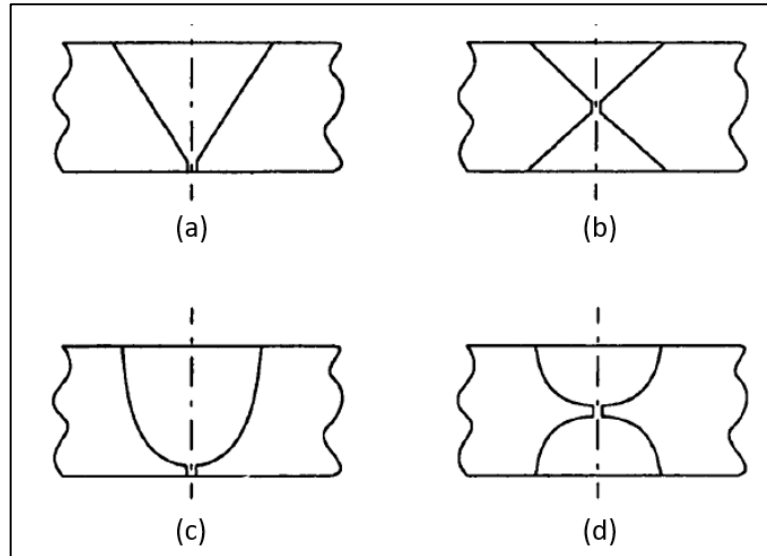
Figure 2.3. Butt joint geometries are prepared for welding. (a) single-sided -V, (b) double -V, (c) single-U, (d) double-U

2.1.2.   Multi-Pass Welding Notation

In the maritime, oil and gas, and offshore industries, the thickness of the V-groove joints requires more than a single pass, usually manually or semi-autonomously deposited, resulting in low efficiency and productivity [28]. These joints must be fit and prepared for welding by a weld fitter prior to welding, following a specific Welding Procedure Specification (WPS) procedure.

Figure 2.4 introduces the terminology for multi-pass welding of a single-sided V-groove open root gap assembly. The root pass refers to the initial welding pass used to join parent metals together, where usually during FCAW welding, a non-permanent ceramic backing

strip can be used to support the root surface and achieve even penetration [25]. The hot pass is the second welding pass used to reshape the root pass, achieve sidewall fusion and fill any inconsistencies caused by improper penetration of the former pass [29]. Filler passes serve the remaining weld groove area until the cap passes, which are deposited to reinforce the weld groove and provide a clean finish to the top weld face. Welding passes which are deposited at the same height offset relative to the top of the root face form a welding layer. The vertical root face (landing) is used to achieve proper fusion with the root sides during root pass and to avoid resulting in burn-through due to excessive heat.
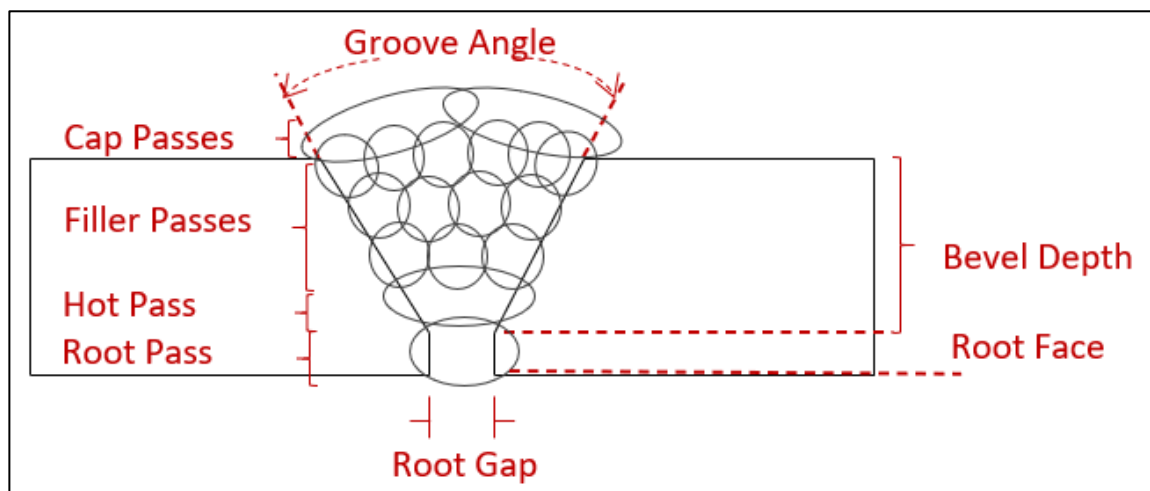
Figure 2.4. V-Groove joint characteristics and multi-pass welding notation

2.1.3.   Welding Environment and Challenges

Despite the progress and massive utilization of welding technology in manufacturing, the actual welding environment still imposes difficulties to welders. During welding, high concentrations of fumes, gases, dust, infra-red and ultra-violet radiation are produced along with substances, such as nickel and chromium, which have an adverse effect on the human respiratory system and may lead to lung cancer and asthma [20].

The welder's environment also is affected by the available volume of work. Lack of space during welding can amplify the exposure to toxic fumes and increase the ambient temperature. Those unpleasant conditions can be met in enclosed spaces, as it happens in the pre-fabrication of double hull structures which prevent the outflow of cargo in the shipbuilding industry [30]. Nonetheless, during the maintenance of such structures, there is limited space for work. Fixed infrastructure that cannot be removed totally can increase the possibilities for injuries while working in a confined area. The fact that other manufacturing processes often take place in parallels, such as grinding, brazing, and cutting of workpieces, can increase the overall associated risk with manual welding.

Due to those environmental and safety concerns, high labour costs, and the fact that many current older tradesmen are retiring [31], there is an increased shortage of skilled welders over the last years. As such, the life span of future assets can be reduced, and the amount of required rework to increase [32].

2.2. Automated Welding

Automated welding solutions can alleviate issues of repeatability, flexibility, quality, and increased production demand. The bulk production of repeatable welds in multi-pass welding of known joint geometries can be delivered through automated welding systems. Such a solution would free welders to be utilized in more complex and creative tasks where a high degree of customization and experience is required and can provide capacity for more welding jobs.

Based on the Degrees of Freedom (DoF) that current automated fusion welding solutions exhibit, these can be differentiated into rectilinear and articulated robotic systems as can be seen in Figure 2.5 (a) [33] and (b) [34,35]. Rectilinear robots (gantry systems) offer a constrained boxed working envelope, ranging from two to three DoFs to enable volume coverage. Alternatively, articulated robots with six or more DoFs mimic human arms, utilizing revolving wrists connected through joints and controlled by servo motors to offer a spherical working volume. Hence, increased flexibility, wider coverage, and speed are introduced with articulated systems.

These articulated robotic manipulators exploit the interest for specific applications that require welding automation, due to multiple DoFs, increased pose repeatability, persistent quality, and enhanced duty cycles. However, the high initial capital investment for the automated welding solutions relative to manual welding equipment is a limiting factor, making SMEs reluctant to adopt these approaches. The current solutions offered by robotic manufacturers require control devices, special training for operators and the need for custom made welding cells that satisfy accurate part placement relative to the welding system. To drive down the cost of those solutions there is a need to increase their working autonomy, thus, to be able to adapt to different welding configurations without adversely affecting the production cycle.
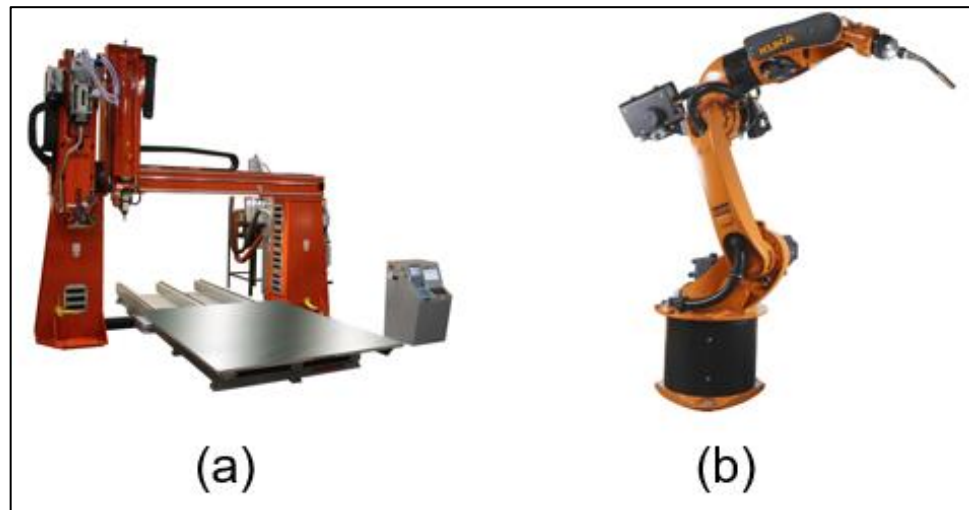
Figure 2.5. Welding robotic systems are classified based on the degrees of freedom (a) Rectilinear robotic system, (b) Articulated robotic arm designed for welding

2.2.1.   Welding Autonomy and Robot Programming

A limited degree of autonomy is exhibited in bespoke solutions for automated robotic welding as the robot has to follow predefined motions in a controlled environment [36]. Regarding the ability of the robotic system to receive feedback from the environment, autonomy is differentiated between operational and decisional.

Robots that can perform a series of repetitive tasks such as spot-welding in automotive manufacturing production lines, in a well-defined volume are characterized with operational autonomy. In contrast, when decisional autonomy is met, the robotic system can sense its environment, acquire and process sensory data, and transform it into actuator actions [37].

2.2.1.1.   Online Programming

Operational autonomy can be achieved through Online Programming (OP) (teach-and-playback). OP is a manual process that consists of the operator's input to define points in space, driving the robotic arm to the points of interest and teaching these into a program. In that way, the robotic path is populated, where afterwards the generation and deployment of kinematics takes place into the robot controller with a pre-selected speed and acceleration [38]. This lead-through method requires robotics knowledge for the generation of kinematics and awareness of possible collisions-singularities. Hence, drawbacks arise, such as mandatory downtime and lack of flexibility. The robot must be utilized during programming and manual re-programming is required to adapt even for slight changes on the same workpiece. As a result, OP is an overall time-consuming and cumbersome programming process.

Although OP is characterized as a time-consuming method to teach robotic motion with an unfavourable ratio between programming and production time, it is predominantly used in SMEs [16,39]. Aiming to decrease the programming load, the introduction of kinesthetic guidance [40] is described as a walk-through programming approach where the operator manually moves the robot arm to the points of interest with the help of additional probe devices, such as tracked pens and laser pointers [39,41–43]. Although this interactive approach minimizes the required knowledge for robot kinematics by incorporating a simulation model, it still requires the user input to optimize the robotic pose and define points in space which is not always possible for large robots due to safety concerns and close interaction [40].

2.2.1.2. Offline Programming

Another approach to achieve operational autonomy is Off-Line Programming (OLP), which relies on the utilization of accurate Computer-Aided Design (CAD) of the workpiece and working cell, without eliminating but still requiring the tedious programming overhead [44]. The working load is shifted to a software engineer, who plans the path and simulates the entire manufacturing process, making sure that there is no collision between the component and the workpiece or any joint singularities. In that way, downtime is minimized as programming can be achieved side by side with production, incorporating robotic simulation. This approach can decrease production cycle time, especially through the existence of Computer-Aided Manufacturing (CAM) solutions which makes it easier to translate CAD data to the robotic controller [45,46].

While this process may be faster to generate the trajectory of the robot relative to OP method, it is still sensitive to the accuracy of the inputted CAD data. Additional cumbersome calibration procedures are required to compensate for deviations between the design and the actual workpiece. SMEs are limited from adopting such technology due to the commercial cost, need for training and robotics knowledge. Integrated welding solution packages from robotic manufacturers making use of CAD, gather common characteristics, as is the manual input to create or validate the sequence of welding tasks as well as the requirement of a custom welding cell where a free-collision model of the cell and workpiece must be provided [47–49].

2.2.1.3.   Visual Servoing Programming

Decisional autonomy can be realized from autonomous programming which combines the features of OP or OLP programming and actions on signal inputs from integrated sensors. In that way, the robot can superpose its path, interact with the environment, and adjust programmed motions.

Path planning generated from Visual Servoing (VS), guides the robotic arm with respect to a target object based on received feedback from a vision system and splits into two main control methods, Position and Image-Based Visual Servoing (PBVS, IBVS) [50,51]. The accuracy and robustness depend on the extraction of the visual features and the capabilities of the vision system [52] and are characterized by high computation load to calculate inverse kinematics and deploy real-time image processing algorithms for pose estimation of the objects [53]. The intrinsic and extrinsic camera parameters and the propagation of error through the pose estimation can affect the repeatability and accuracy of this control scheme, resulting in unpredicted robotic motion [54,55]

2.2.1.4.   Sensor Guided Programming

An alternative approach to achieve decisional autonomy for automated robotic welding systems is the use of sensor-guided path planning. The shift from the mass repetitive fabrication of large scale workpieces to more one-off custom products with specific requirements and constraints in small batch production [56], establishes the requirement for intelligent and sensor-enabled welding solutions able to identify and adjust dynamically to the welding environment.

Hence, to overcome these limitations which are introduced from an unstructured environment, the use of sensors such as optical and tactile, mainly to introduce feedback on the robot programming task, constitutes sensor-guided programming [16]. Global methods such as drawing manually with a marker pen the robotic path in the workpiece are observed in [57–59]. Following the image processing algorithms for edge detection, vision and force-torque sensing are combined to generate a 3D robotic path. As an alternative, approaches where the operator interacts to mark a path in the image instead of on the workpiece, the starting point and the direction of motion, deliver a more interactive programming process [60,61]. Stereo vision is used in [62,63] for the generation of welding paths, by extracting 3D coordinates from distinct features such as corners and edges in combination with structured light sensors, plane fitting and reconstruction of the images. 3D reconstruction through structured light sensors is utilized to adapt to OLP methods by optimizing the position and orientation (pose) of the end-effector [64,65]. Local approaches developed to adjust deviations relative to pre-planned robotic paths employing optical triangulation sensors for seam tracking are widely researched [66–70].

Among the main advantages of the sensor-guided approaches are the integration of motion programming within the production process and the consideration of the actual workpiece geometry rather than the CAD design [71]. This strategy proves to be a more flexible robotic programming approach relative to OP, OLP and VS, effective in providing automation capability [23].

Table 2.1 illustrates the degree of autonomy that characterize robotic welding systems along with the types of programming approaches.

Table 2.1. Level of automated welding approaches along with robotic programming techniques

Robotic Autonomy	Programming techniques
Operational	• Online Programming (OP) (Use of teach pendant to program robotic motion) • Off-Line Programming (OLP) (Import CAD of welding assembly to robot simulator)
Decisional	• Visual Servoing • Sensor Guided

2.2.2.   Vision Sensing

An integral part of sensor guided programming is the use of sensors that can collect and introduce feedback to the programming process from the existing welding environment. Automated robotic welding systems utilize a series of sensing modalities, such as arc [72,73], acoustic [74], vibration [75] and vision sensing [76–79]. Vision sensing technology can be divided into passive and active vision as to whether an external light source is utilized. More specifically, active vision systems use a light source (laser beam) to project onto the surface workpiece a thin luminous straight line and a Charged Coupled Device (CCD) or Complementary Metal-Oxide Semiconductor (CMOS) camera sensor images the projection [80]. On the other hand, for passive vision systems, usually a monocular or a stereo system is utilized with two cameras to extract image features from the welding scene.

The integration of vision sensors, such as 3D or 2D cameras is of special attention to the automated robotic welding community, due to the non-contact nature of the sensing modality. Image processing and pattern recognition algorithmic advancements over the last few years make vision sensors a suitable candidate to locate the welding specimen in the scene [76,81,82], identify the weld seam path [78,83–85] and monitor the weld pool geometry [86–89] for assessing penetration and abnormalities during welding. However, these methods can suffer from noise that is introduced from the environment due to varying lighting conditions and low contrast with the workbench when using mid alloy steel, which is not the case when aluminium is used. Moreover, active vision methods using structured light sensors are affected by low reflection due to steel surface attributes (i.e. low reflectivity index) and discontinuities introduced from poor joint machining, possible spatter and fumes during welding. Based on these considerations, the laser beam can be scattered to the welding joint and captured with a low signal-noise ratio from the camera sensor, appearing distorted [90]. Laser scanners also tend to be more expensive than cameras, since they can offer higher accuracy in the range of μm.

2.2.2.1. Workpiece Localization and Seam Tracking

The initial step of an automated robotic welding task is to guide the robotic arm to a suitable position for welding, which is the result of identifying the specimen in the scene. Following that, the seam of the welding groove must be extracted accurately to drive the welding torch along the groove, adapting the pose of the torch to achieve proper fusion with the base plates, mimicking manual welding techniques. An important aspect in both

processes is the identification of features able to identify and construct the pose of the specimen relative to the welding system.

Among the different methods for feature extraction toward workpiece localization, edge and corner detection [78,79,82], image segmentation [77,78] and the use of a predefined Region of Interest (ROI) have been explored [91,92] (Figure 2.6). Although these methods prove to be resilient in a controlled environment, when considering the production floor they are often affected by poor or variable lighting, surface contrast, and lack of suitable fitting of welding joints to match the CAD design.
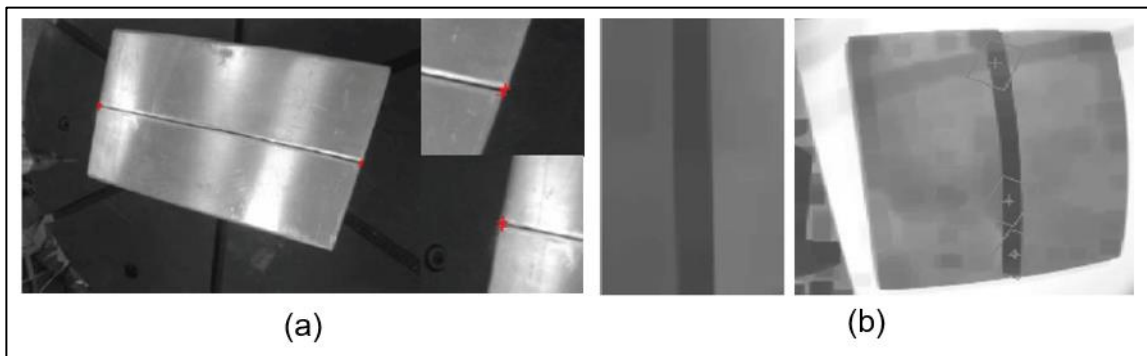
Figure 2.6. Workpiece Localization: (a) Corner detection for estimation of start-end points of weld groove, (b) Template matching of the seam to localize the workpiece in the welding scene

Seam tracking methods are known as local methods constrained to the welding specimen's region, since the information of the location of the workpiece relative to the robotic welding systems is already known. These can be categorized as ROI; structured light; and, arc methods.

Similarly, to workpiece localization techniques, the ROI methods for seam tracking utilize a region of interest around the groove edges of the weld pool which is used online during welding to identify the seam path (Figure 2.7). Vision processing methods, such as binary segmentation using an adaptive threshold to eliminate the background image [93] and edge detection algorithms (i.e. Canny, Sobel) with median filtering can reveal the edges of the welding specimen [94].
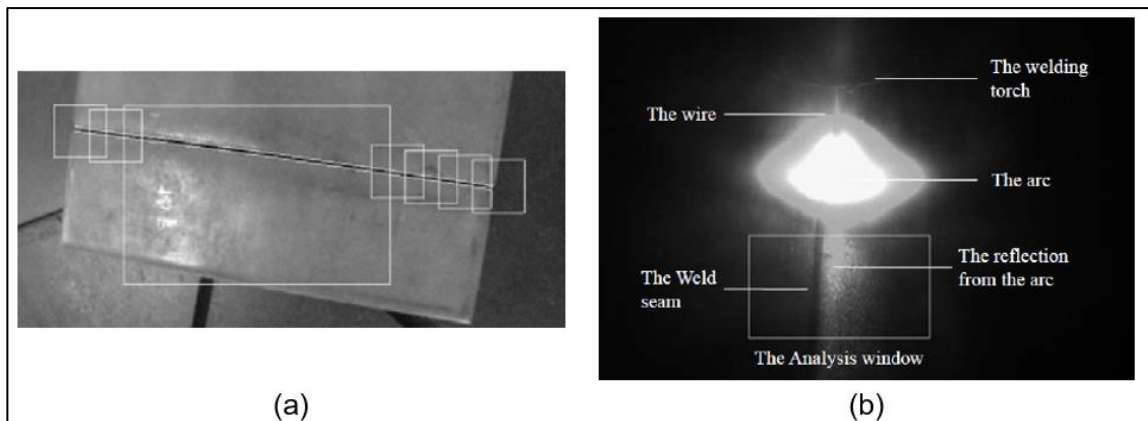
Figure 2.7. ROI methods used for seam tracking

Arc sensing, as the name implies, this approach can be used during welding to identify the seam path, utilizing the variation of the Contact Tip to Work Distance (CTWD) while the welding torch weaves and travels along the welding groove. Varying the CTWD, introduces small variations in current and arc-length (voltage), where these variations can last between 100-200 ms [72]. This feedback can be used to superpose the motion of the end-effector during welding. Arc sensing is preferred for SAW, since there is no visual contact with the arc, molten pool and edges of the joint [72]. Although this method can provide relevant information for the seam, it cannot be used in all processes or materials

such as Aluminium, since the changes in the current are not significant enough to generate feedback and the thickness of the material must be above 2 mm [95].

Structured light methods utilize laser triangulation sensors for seam tracking, which are quite popular due to fast acquisition rates (up to 5000 Hz); simple deployment for feature extraction [72]; and, integration with automated welding systems [68,69,96].

The quality of the surface reflected signal affects the accuracy of laser scanners. This depends on the characteristics of the surface (reflectivity index), ambient light conditions, angle of incidence and distance between the laser and the specimen [97]. The accuracy of feature extraction for off the shelf laser scanner systems can range from 0.025 mm for Arc-Eye Vision System and Servo Robot [98,99], to 0.05 mm for Meta Vision [100]. Micro Epsilon's latest commercial systems can achieve 0.2 mm accuracy and 0.5 mm for Liburdi and Wise Technologies [101,102]. Nonetheless, the operating specification of the industrial scanners provided by the manufacturers is generated in a controlled environment, where usually these results differ from the actual field of operation.

2.2.2.2. Hand-Eye and Camera Calibration

Workpiece localization hinders the estimation of the rigid body transformation between the workpiece and the robot's end-effector (welding torch). As the extraction of features and the estimation of the pose can be separated, hand-eye calibration is a method to determine the pose (orientation and translation) between the end-effector and the vision system [103]. Integrating hand-eye calibration into robotic systems provide the means to interact with the environment and relate robot kinematics to the vision system, enabling

image-guided systems. Different applications based on hand-eye calibration, ranging from robotic welding [103,104], drilling [105], grinding [106], and medical inspection [107] deliver vision control tasks.

Figure 2.8 describes the coordinate transformations of a hand-eye robotic welding system where the camera is mounted on the end-effector (eye on hand).
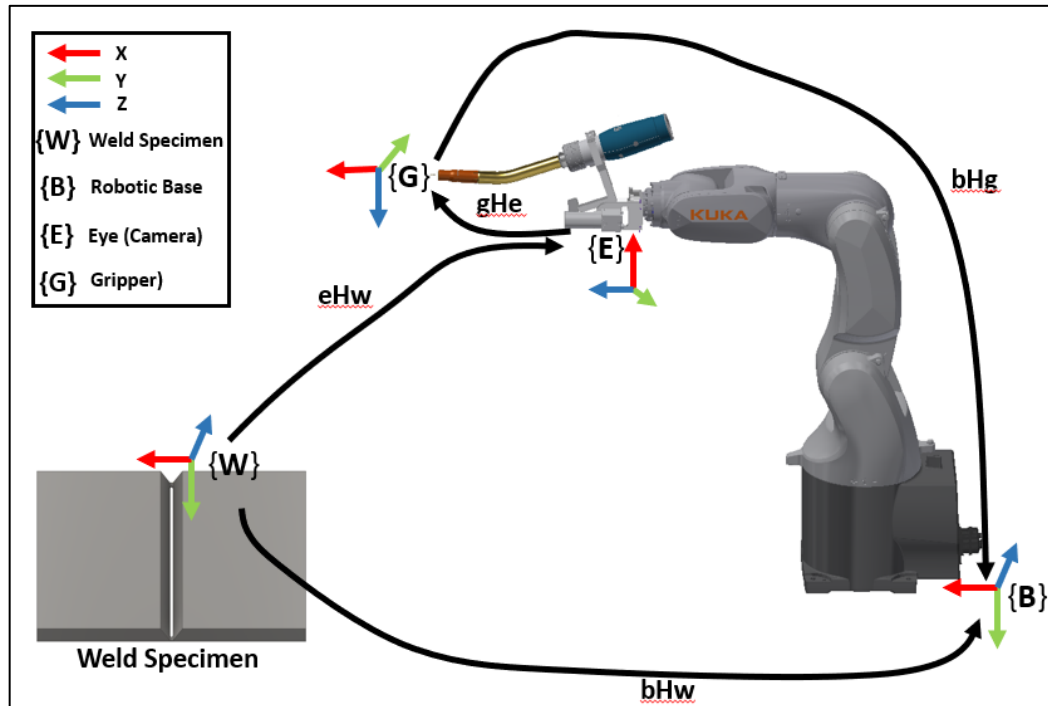
Figure 2.8. Hand-Eye calibration and relative coordinate transformations. Letters B, E, G and W stand for robotic Base, Eye (camera) frame, Gripper and Weld specimen respectively

The following transformations are defined, where:

- bHg: Transformation matrix 4x4 describing the pose of the welding torch (end-effector) relative to the active motion frame of the robot
- eHw: Transformation matrix 4x4 describing the pose of the weld specimen relative to the camera ("eye") frame

- bHw: Transformation matrix 4x4 describing the pose of the weld specimen relative to the active motion frame of the robot
- gHe: Transformation matrix 4x4 describing the pose of the camera frame relative to the weld torch frame

The direction of the arrows that represents the different transformations between the coordinate frames, are defined relative to the "last" coordinate frame where the pose is defined (i.e. gHe the pose of the eye is defined relative to the gripper)

The homogeneous equation $AX = XB$, where A describes the robot motion and B the camera induced motion from the welding torch, can be used to solve the hand-eye transformation X [108,109]. In this approach, the robot is guided through different positions, within the Field of View (FOV) of the camera and the robot's working envelope to obtain poses of an object with known dimensions, usually from a checkerboard. For every position two transformations are known, (bHg, eHw), and are recorded. The result of the calibration which is the gHe transformation can be used to find the pose of the weld specimen relative to the robot motion frame (base) as given by Equation (2.1)

$$bHw = bHg \cdot gHe \cdot eHw \qquad (2.1)$$

In parallel, the calibration of the camera system to compensate for the lens, radial and tangential distortion, due to non-perfect alignment of the lens with the centre of the principal axis can be estimated from the collected frames of the hand-eye calibration procedure utilizing the pinhole camera model [110]. The result is the intrinsics matrix K described by Equation (2.2) and the radial and tangential distortion coefficients k_1, k_2, k_3, p_2, p_3 which define the camera parameters.

$$K = \begin{bmatrix} f_x & 0 & c_x \\ 0 & f_y & c_y \\ 0 & 0 & 1 \end{bmatrix} \qquad (2.2)$$

Where:

- (f_x, f_y) $stands\ for\ the\ focal\ point\ of\ the\ camera$
- (c_x, c_y) $stands\ for\ the\ principal\ point\ of\ the\ camera$

Following the estimation of gHe and the camera calibration, where both remain constant unless there is an offset of the camera system relative to the welding torch, including the focus of the lens, the extraction of the pose of the specimen relative to the camera (eHw) and the pose of the welding-torch relative to the active motion frame (bHg) are required. bHg is extracted from the robot controller and only eHw which is the extrinsics of the camera needs to be estimated. The process describing the estimation of eHw transformation takes place in Section 5.3.1. A pose estimation method from 2D to 3D camera system requires the extraction of distinguishable image features, at least three non-collinear points able to define a coordinate frame related to the pose of the specimen.

2.3. Non-Destructive Evaluation

During welding and depending on the control of the welding process, unintentional flaws and defects may arise on the weldments, having an adverse effect on the structural integrity and the lifetime of the components. Hence, early evaluation of the welding result can increase the lifespan of assets and the repeatability of the automated welding systems [32].

There exist non-destructive and destructive methods for assessing weld quality. A commonly used destructive method which requires cutting a piece of the weldment for metallographic inspection is acid etching [111]. Alternatively, Non-Destructive Testing (NDT) methods can be utilized to inspect the surface and internal structure of the welded joints without damaging the component.

Since welding quality is determined from the final application where the welded assembly is utilized, there are established acceptance standards, defining limits related to the presence and size of flaws. BS EN ISO 5817 refer to the quality level of imperfections for fusion-welded joints in steel [112], while the Def Stan 02-773 is related to the minimum acceptable standards for welds in submarines and surface ships [113]. NDT methods for welds range from Visual Inspection Testing (VT) which can detect flaws on the surface of welds, to Liquid Penetrating Inspection Testing (LTI) and Magnetic Particle Inspection Testing (MTI) which can reveal finer cracks and imperfections around the surface of the weldments. Radiography Inspection (RTI) and UT methods can be used to detect flaws along the volume of the welded joint. Here in this work, evaluation of the welding results and inspection for defects was performed utilizing mainly UT methods due to the industrial partner requirements.

2.3.1.   Ultrasonic Testing

UT is the most commonly used method for NDT inspection for a variety of materials, such as aluminium, mild and stainless steel due to its ability to detect both planar and volumetric defects and its relatively low cost [17]. UT utilizes high-frequency sound waves, between 20 kHz and 20 MHz, which are transmitted from a thin piezoelectric

ceramic disk within a transmitting transducer-called single element transducer. A pulse-echo configuration is used where the generated waves can propagate through solids, liquids, and gas, producing vibrations in the particles and continue to travel through, until they are either reflected or scattered by a boundary with a different medium [17]. If for example in a welded joint, during wave propagation a discontinuity is met, part of the energy is reflected and picked up by a receiving transducer, resulting in an amplitude change of the transmitted wave. Utilizing the received signal and knowing the propagation velocity of the sound on the welded material, the location within the volume that the potential defect exists can be measured.

It is quite common for UT inspection of welds to deploy an angled transducer which generates sound waves in the weld, enabling the waves to reach a defect from the sides. Most of the time defects in welds are not formed parallel to the surface, thus angled beam testing is useful to reveal the presence of these flaws. Figure 2.9 depicts the UT angled beam testing, where a defect which is part of a weld causes the generated beam to reflect back to the transducer [114].
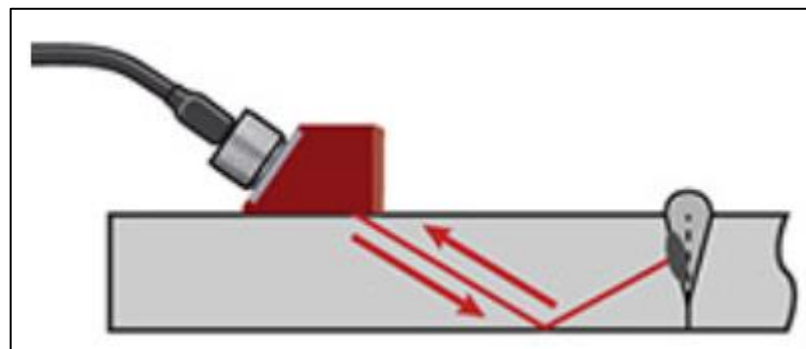
Figure 2.9. UT Angled beam testing [114]

2.3.1.1.   Phased Array Systems

The use of multi-elements in a single transducer assembly forms an array of elements, which offer increased inspection flexibility than conventional single-element transducers [17]. The number of elements usually varies from 16 to 256 and can be pulsed separately in a sequential pattern. The term phased refers to the control of the phase or time delay that each element is pulsed. As can be seen from Figure 2.10, phase control allows combining multiple waves into a single generated wavefront, controlling the direction and shape by steering and focusing the beam. In that way, the resulting beam can be swept over the inspection area at a different range of angles (sectorial scan) enabling the inspection of complex geometries such as Wire Arc Additive Manufacturing (WAAM) components [115,116].
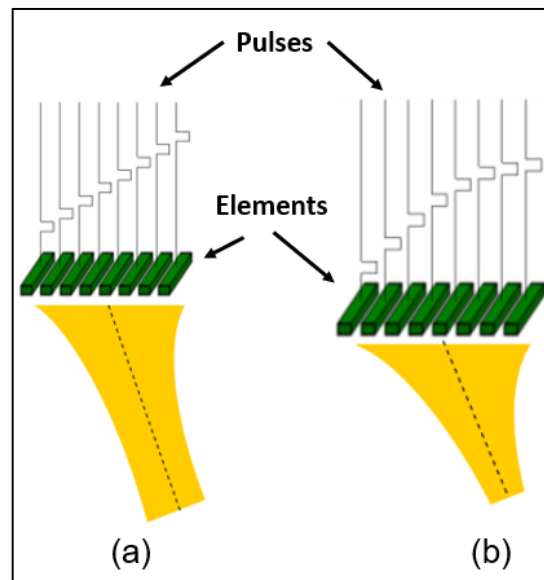
Figure 2.10. Controlling the pulsing of elements phased array systems allows the control of the generated wave beam: (a) Steering the beam, (b) Steering and focusing the beam

A big advancement over conventional single-element transducers is the ability to scan a large area without manually moving the probe to sweep the beam, which can be utilized when there is limited space for NDT inspection. Moreover, electronic control of the generated beam allows focusing to different depths, which is useful for volumetric inspection.

Chapter 3

Holistic Sensor-Enabled Robotic Arc Welding System

3.1. Introduction

State of the art automated welding solutions, which rely on robot controllers to calculate the kinematics and deploy the motion cannot adapt to the welding environment or react to any changes to the workpiece. Research projects, such as MARWIN aimed to provide automated welding capabilities for SMEs [117] and HEPHAESTOS I & II, a candidate for ship repair welding fabricated parts [118], were developed based on the use of CAD data to generate robot paths, 3D reconstruction and vision analysis on a custom welding setup (vision survey system, edge detection) to generate 3D data respectively. Hence, the efficiency of automated welding systems is limited by high product variance for SMEs and unstructured environments.

The efficiency of these systems can be enhanced by accommodating a purely-sensor guided motion where an external-real time controller generates the kinematics based on

the sensor's feedback, without being dependent on commercially available software and communication protocols provided by industrial robotic manufacturers.

This Chapter presents the first, second and last novel elements of this thesis (stated in Section 1.4) which is the transformation of an off-the-shelf robotic arm which was designed initially to assembly electronic components and perform light duty tasks into an automated arc welding system for confined spaces according to the industrial partner's requirements. Additionally, the adaptive character of the developed arc welding system (experimentally verified in Chapter 5) is accomplished from the real-time motion control module which facilitates the sensor-guided motion for automated welding by eliminating the need for manual teaching of robotic paths and human input during welding. Moreover, as part of the software setup, the Tool Centre Point (TCP), camera and Hand-Eye calibration, along with the laser scanner performance assessment are described, (which are used in Chapter 5) for the automated workpiece localization and adaption of the welding system to the welding configuration. This described technology is accompanied by the development of robotic software suite that accommodates the user's real-time interaction with the welding procedure providing the means to control and reconfigure the robotic kinematics and welding dynamics during welding.

3.2. Hardware

3.2.1. Robotic Arm

From a hardware perspective, commercial off-the-self welding robots from industrial robotic manufacturers are characterized by high reachability, ranging from 726 – 3,101 mm and a payload range from 6 – 22 kg [119].

Owing to the industrial partner requirements for the welding environment, associated with this research, which limits the working volume of the robot in a compact space (Section 1.2), it was decided that a small articulated robotic arm with a maximum reach of 541 mm, rated payload of 3 kg, high repeatability of 0.02 mm and working volume of 0.61 m^3 will be employed for the specific research project. Its relative low mass of 26.5 kg allows two operators to carry and place the robot between jobs. Figure 3.1 shows the KUKA KR3 which was procured to be transformed into a welding robot since this robotic arm was initially designed to assemble electronic components.
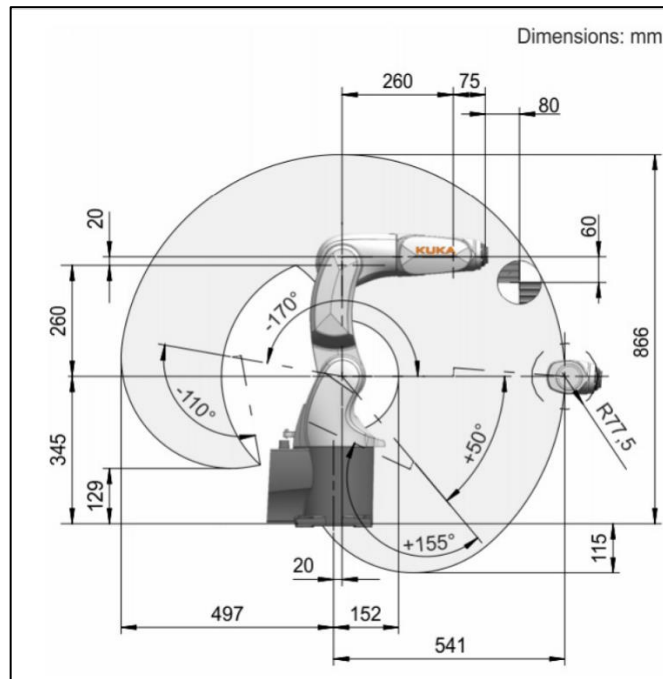
Figure 3.1. KUKA KR3 with a maximum reach of 541 mm and a 3 kg rated payload was transformed into a welding robot

3.2.2.   Transformation to a Welding Robot

To transform the KUKA KR3 arm into a welding robot, a welding bracket was designed and manufactured from Aluminium which provided a good combination of being lightweight material and durable against heat input during welding. The bracket was designed to facilitate three different sensors for path planning purposes and feedback before and during welding and a welding torch that act as an end-effector.

Figure 3.2 illustrates the custom-made welding bracket technical design along with the sensors used for the development of the automated welding system. This configuration resulted from a series of feasibility studies were performed in Coppelia Sim [120], to identify the suitable length for the robotic welding hose and possible singularities that may

44

occur during path planning, due to the custom-made welding bracket. As can be seen in Figure 3.3, concerning the fact that the KUKA KR3 arm was limited for additional weight, it was found that a robotic welding hose of 1.2 m in length and a total weight of 2.35 kg was able to provide a welding working range of $2,100\ cm^2$. Regarding the possible singularities, a feasibility study through the RoboDK environment [121], showed that for a welding specimen that is placed within reach of the welding robot, an angle of $108°$ between the welding bracket and axis five of the arm, would be sufficient to avoid any singularities for automated robotic multi-pass welding of single-sided V-grooves. The simulated robotic path for the investigation of singularities and the angle between the welding bracket and axis five can be seen in Figure 3.4.
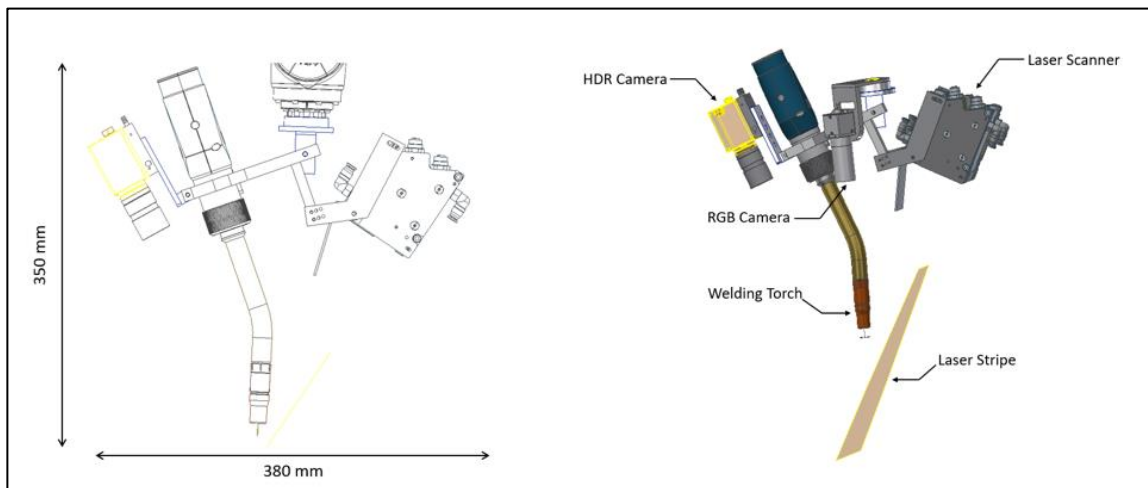
Figure 3.2. Custom welding bracket mount which accommodates a laser scanner, HDR Welding camera, RGB camera and a robotic welding torch

45
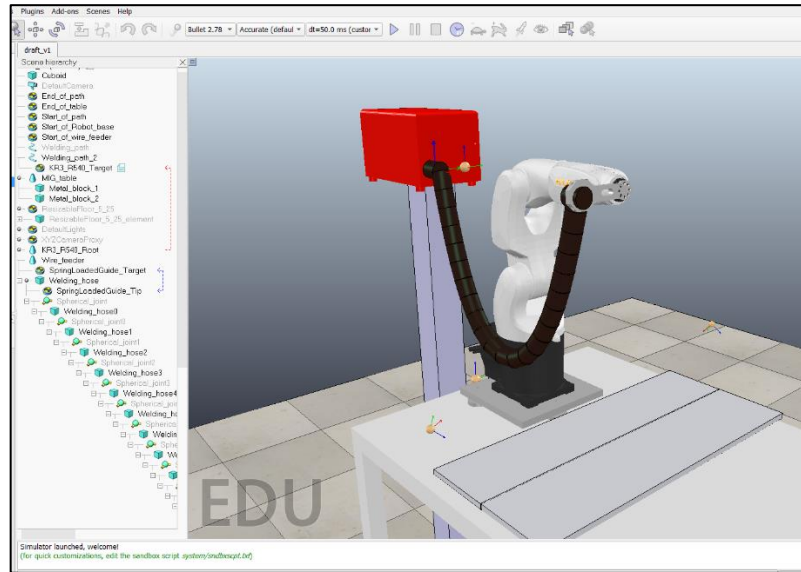
Figure 3.3. A feasibility study performed in Coppelia Sim, provided the length of 1.2 m for the robotic welding hose of the developed holistic sensor-enabled robotic welding system
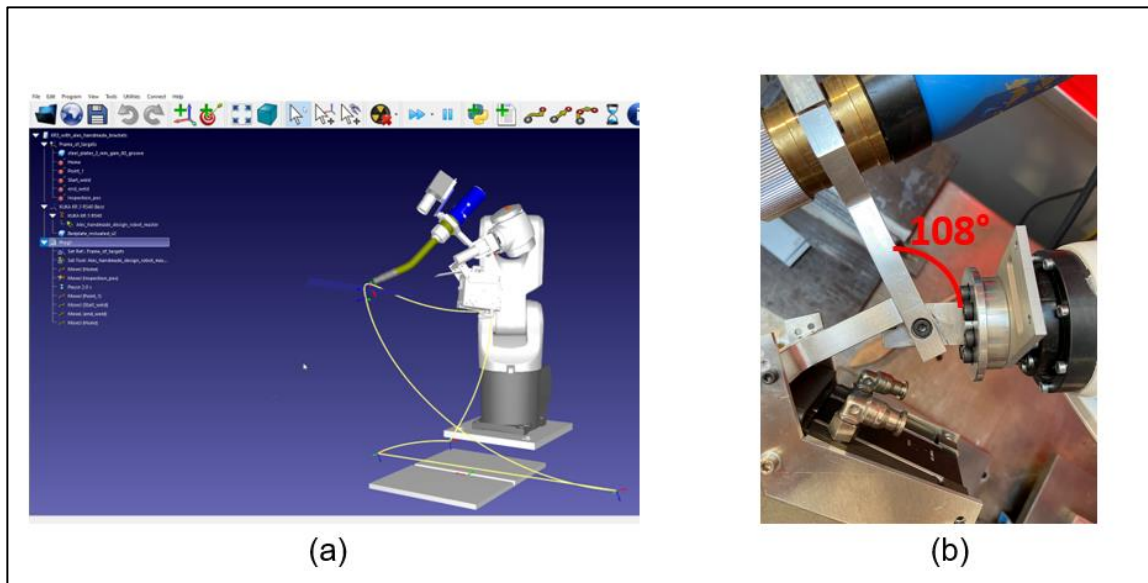
Figure 3.4. (a) Investigation for singularities through RoboDK simulations – path marked with yellow colour, (b) Angle between the welding bracket and axis five of the arm to avoid possible singularities during path planning

In addition, to accommodate the flexible mounting of the robot to different metallic surfaces, a magnetic base was designed and machined in aluminium of 15 mm thickness. The base consists of three manual switched on/off magnets, each one with 70 kg pull-force, securing in place the 26.5 kg arm as depicted in Figure 3.5(a). In that way, the arm can be placed before welding within reach of the joint to be welded, without the need to be fixed in place as happens with commercial welding robots. To ensure electrical isolation between the robotic arm and the welding specimen, during welding, plastic tubes were placed between the bolts as can be seen in Figure 3.5(b). As a result, the existing sensitive robotic electronics and the servo motors which drive the revolving wrists were not affected during welding.
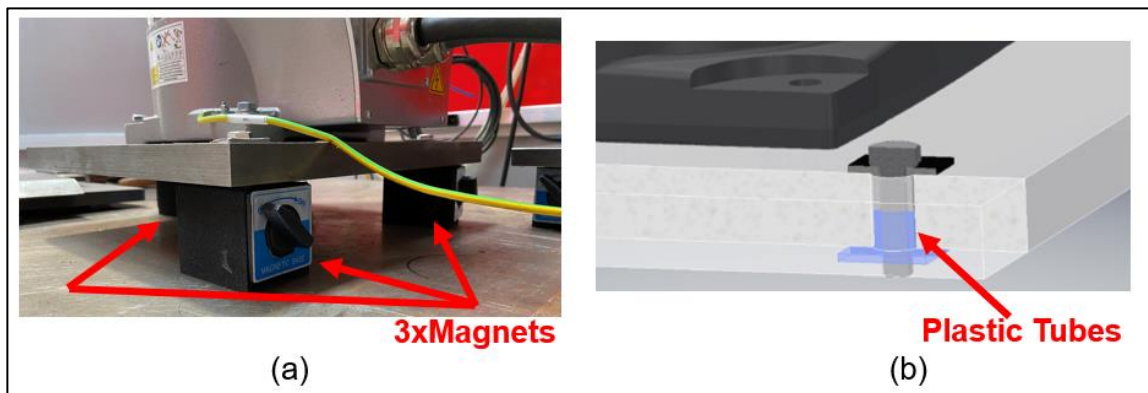
Figure 3.5. (a) Flexible magnetic plate with switch on/off magnets, (b)Electrical isolation between the robotic arm and welding specimen

3.2.3.   Robotic Welding Setup

The developed holistic sensor-enabled robotic welding system for automated multi-pass welding is shown in Figure 3.6 and detailed in Table 3.1.
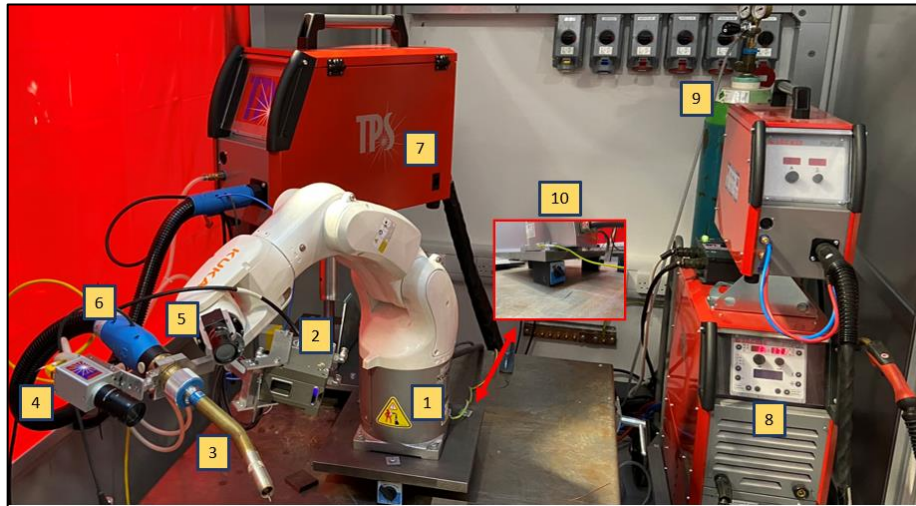
Figure 3.6. Modularized robotic welding setup consisting of a magnetic-based KUKA-KR3, sensors and a flexible mounting robotic wire feeder.

Table 3.1. Robotic and welding equipment layout

#	Equipment
1	KUKA KR3-R540
2	Micro-Epsilon Scan-Control 2910-100/BL
3	TBi Weld Torch 22°
4	XIRIS XVC 1000
5	Blackfly RGB PGE50S5C
6	TBi Weld Torch Hose 1.2m

7	*Jackle Robo Wire Feeder*
8	*Jackle 400V ProPulsWelder*
9	*Gas ArCO$_2$ (80% Ar + 20% CO$_2$)*
10	*3x Magnets (70 Kg Force)*

A laser scanner (2) from Micro-Epsilon was selected due to its high accuracy of 0.2 mm and the utilization of a blue laser diode which makes it insensitive to shiny metallic surfaces due to the lower penetration of its wavelength compared to the red laser diode scanners [122,123]. This sensor is used to extract key points to build the welding reference path and geometric features of the single-sided V-groove geometry which are used as inputs to the multi-pass welding system described in Chapter 4. These data enable adaption of the pose of the welding torch relative to the welding joint, as a manual welder would do to apply a forehand welding technique with solid wire. The XIRIS XVC 1000 (4) High Dynamic Range (HDR) camera is utilized to provide visual feedback on the weld pool during welding. The built-in technology of 140+ dB dynamic range along with the internal Field-Programmable Gate Array (FPGA) image processing enables high-quality weld pool monitoring up to 55 Frames per Second (FPS). A Backfly RGB camera (5) identifies and extracts the pose of the welding joint in the scene relative to the robot motion frame through the Hand-Eye calibration. The machine vision camera can output 22 FPS at the maximum resolution of 2448 x 2048 and relies on the Generic Interface for Cameras (GenICam) programming protocol which allowed a straightforward integration in the developed programming environment.

The available three-phase JACKLE inverter power source of the welder supported pulsed MIG/MAG up to 400V at 50% duty cycle with an interconnected robotic wire feeder [124]. Due to the industrial partner requirements, the selected welding procedure was MAG using a pulsed current to reduce the welding spatter in absolute wire-feed speed synergic mode [125–127]. A constant flow rate of shielding gas mixture $ArCO_2$ (80% Ar + 20% CO_2) at 15 l/min along with a solid filler wire of 1.2 mm diameter with characteristics recorded in Table 3.2 were used.

Table 3.2. Chemical composition of solid wire (%) - (Based on manufacturer certificate)

C	Si	Mn	P	S	Ni	Cr	Mo	Cu	V	Al	N	Ti+Zr
0.081	0.86	1.46	0.011	0.007	0.02	0.04	0.01	0.02	<0.01	<0.01	0.007	0.008

In terms of control, an embedded real-time target cRIO 9032 [16] was utilized (Figure 3.7), featuring a real-time Intel x64 processor and an FPGA on board allowing low-level and real-time parallel computations. For the four expansion slots, an analogue output module NI-9263 [128], an analogue input module NI-9205 [129], a digital output module NI-9476 [130] and a digital input module NI-9425 [131] were used. These modules provided the means to interact with the welder and control the welding dynamics with a scan frequency of 100 ms, which was feasible from the welding equipment. Moreover, the welding power source through the NI-9205 module provided feedback on the welding current, wire feed speed and voltage through 10V differential lines allowing the recording of those data in binary files for each welding pass. Finally, the process diagram in Figure

3.8, summarizes the system architecture along with the signal types between the allocated

equipment.

Figure 3.7. cRIO 9032 was used as a real-time controller for the application of automated robotic welding utilizing four Analogue/Digital modules for reliable interaction between welder and developed software
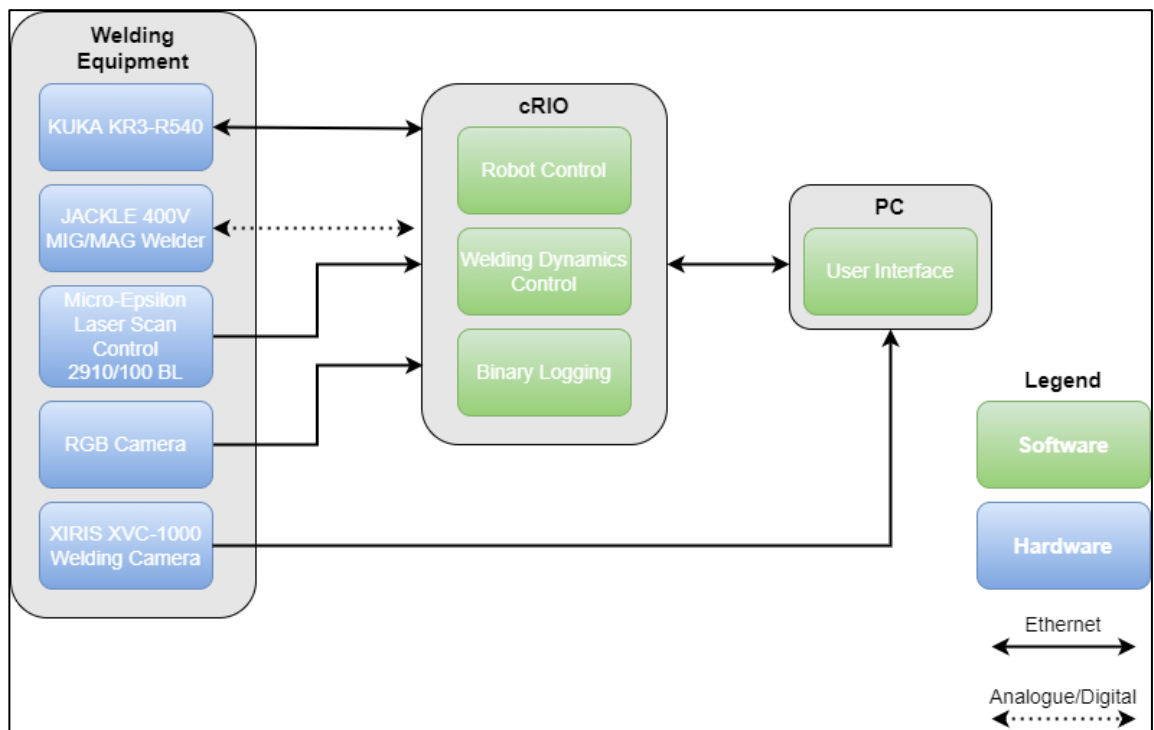
Figure 3.8. A high-level diagram of the automated robotic arc-welding system along with the signal types used between the equipment

3.3. Software

A software suite to control the automated robotic welding system was developed in LabVIEW 17 SP1 programming environment [132] and deployed in the real-time target cRIO 9032. The choice of the language was mainly determined by the reliable communication that LabVIEW offers between different equipment and rapid prototyping in addition to a plethora of available software libraries. Three parallel JKI state machines [133] were utilized to form the backend, where each one was responsible for handling the robot motion control through the laser scanner and RGB camera, the welder dynamics and binary logging of data respectively. The frontend GUI can be seen in Figure 3.9 which

consists of numerous controls, boolean and numeric indicators to enable interaction of the

user with the automated robotic welding process.
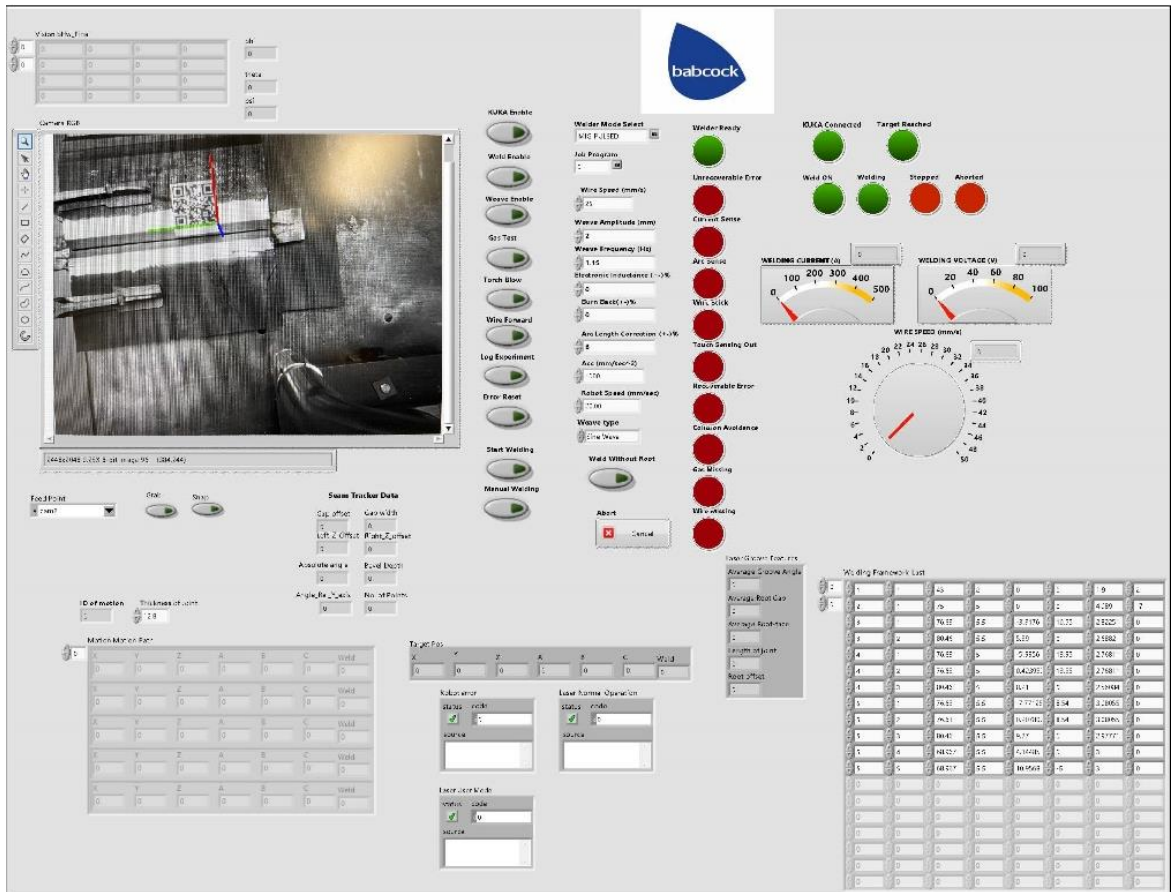
Figure 3.9. Developed GUI for controlling the automated robotic multi-pass arc welding process

Figure 3.10 depicts the vision sensing inspection process prior to welding which

commences automatically with the KUKA enable boolean button and the process

described in Section 5.3.1 is called with the Grab button to extract the welding

configuration pose relative to the robotic system base. Additionally, Figure 3.11 shows

boolean controls and numeric inputs which provide the opportunity to the operator to

control the welding dynamics (wire feed speed, arc length, weave characteristics) and

robot kinematics (speed, acceleration) as well as to abort the whole process. Moreover, Figure 3.12 illustrates the collection of digital outputs from the welding equipment which indicate the behaviour of the welding system during live arc and provide continuous feedback through the numeric indicators regarding the welding process parameters, such as the welding current, voltage and wire feed speed. These numeric indicators are logged in the backend following the internal scan period of the analogue modules of cRIO which was 100 ms.

Lastly, in Figure 3.13 the red dotted rectangular depicts the geometric characteristics of the welding joint which are extracted from the laser-tactile sensing approach (Section 5.3.5) following the compensation for the vision and human error from the placement of the QR code. The green dotted rectangular depicts the generated multi-pass sequence schedule per welding layer consisting of the welding passes, pose of the torch, weaving characteristics and robot speed. That schedule is adapted to the single sided V-groove geometry based on the extracted geometric characteristics and the algorithmic advancements described in Chapter 4.
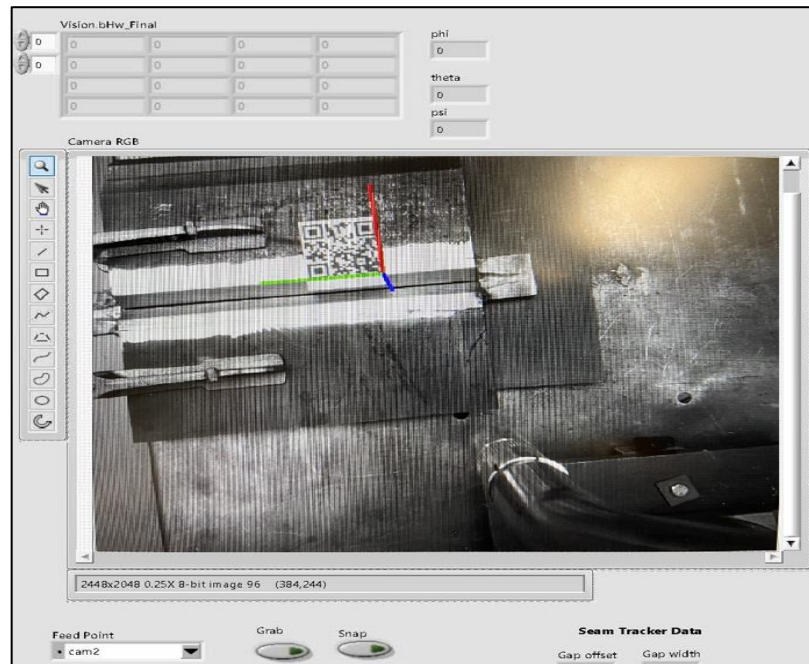
Figure 3.10. User initiated vision sensing process based on Hand-Eye calibration to extract the pose of the welding configuration through the fiducial QR code (Section 5.3.1).
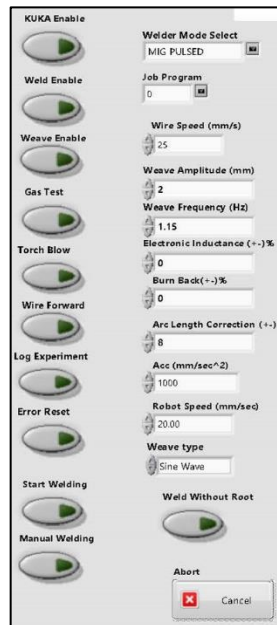
Figure 3.11. Boolean buttons and numeric controls to allow the user to control the welding dynamics and robot kinematics in real-time based on the feedback from the welding camera.

55
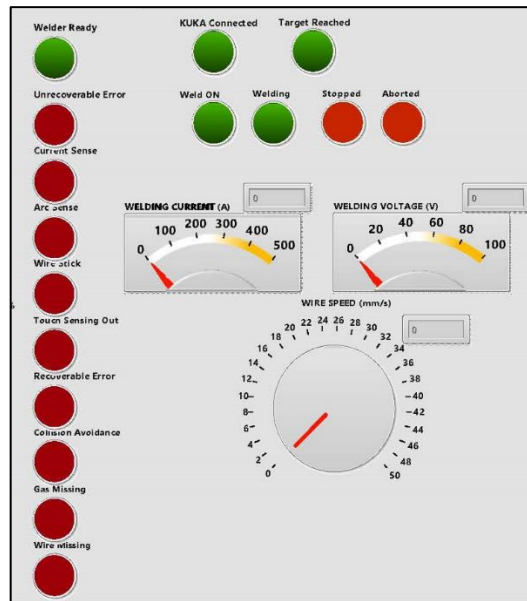
Figure 3.12. Digital outputs from the welder provide continuous feedback to the operator regarding the behaviour of the welding process (stable arc) and indication of welding process parameters (current, wire feed speed, voltage).
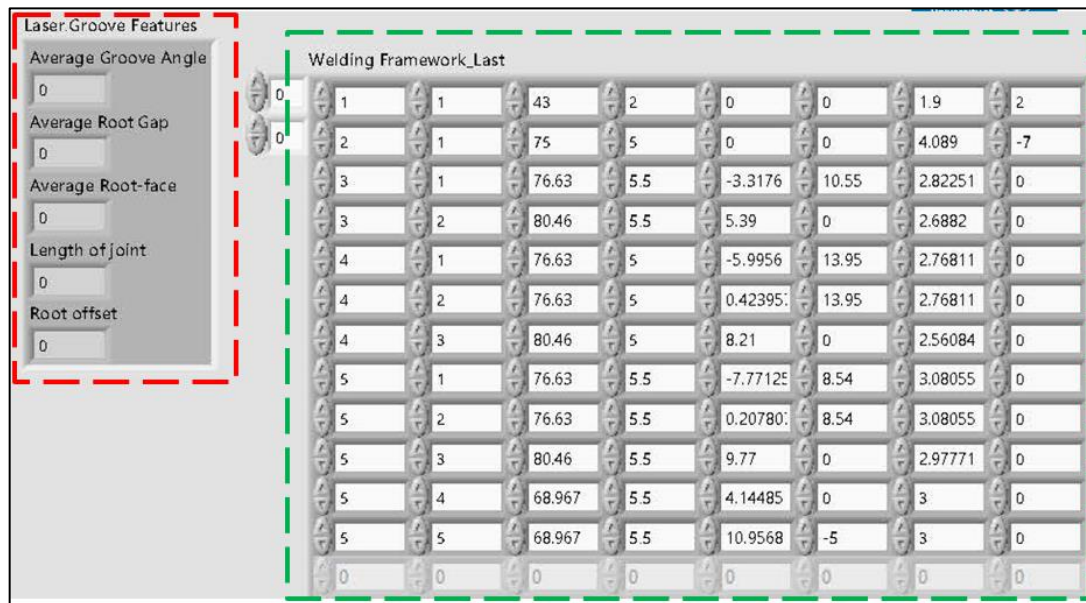
Figure 3.13. Red dotted rectangular contains the extracted geometric characteristics of the V-groove geometry whereas the green dotted rectangular depicts the generated multi-pass welding sequence per welding layer.

3.3.1.   Real-Time Sensor Driven Robotic Control

An integral part of the software suite was the development of a real-time motion control module to enable automated robotic path generation and kinematics deployment. The Robot Sensor Interface (RSI) [134] technology package, which was developed by KUKA to influence a pre-programmed motion based on the sensor's input, was utilized and built upon, to enable a purely sensor-guided external motion control of the holistic automated welding system. This technology package allows cyclical real-time signal processing which executes with an interpolation cycle of 4 ms for KUKA Robot Controller (KRC) 4 robots and at 12 ms for KRC 2 robots.

In previous works, such as in [115], the RSI package was used to control the motion of a robotic arm, through a force-torque sensor's output, while inspecting for defects in a composite wing specimen. In that way, the ultrasonic wheel probe at the end of the flange was able to achieve sufficient contact with the specimen under inspection at a constant set force and compensate for deviations between the CAD model and the actual workpiece. A downside of the proposed method was the generation of the robot path beforehand with a robot program as well as the deployment of kinematics under the KRC 2 controller. Moreover, in [135], a customized toolbox was built in C++ enabling control of 6 DOF-KUKA robots through RSI. The developed functions were compiled under a Dynamic Link Library (DLL), allowing the integration of the Software Development Kit (SDK) into different programming environments e.g. MATLAB, LabVIEW, Python, and C#. However, the developed solution was not able to accommodate real-time correction based

on sensory input such as varying speed, and acceleration essential for weaving adjustment during welding, since the generation of kinematics took place within the KRC.

To overcome, previous limitations and exploit the full external control of the robotic arm, a real-time control module was developed based on the RSI package. A requirement for the application of holistic and adaptive robotic welding, was the autonomous population and adaption of the path planning for the welding torch (end-effector) on the fly, utilizing optical and tactile sensing through the RGB camera, laser scanner, and wire touch sensing modalities. In that way, the KRC 4 did not hold any previous pre-programmed path and the motion was updated in real-time with a positional correction increasing the flexibility and minimizing the programming time for the robotic arm to adapt to a new environment.

To achieve on-the-fly positional corrections as software module performing on-line iterative cycles of position interpolation in cartesian space based upon sensory input was created where the required corrections could then be "actuated" based upon the associated calculations. The developed module consists of a trajectory control algorithm, the utilization of a User Datagram Protocol (UDP) communication scheme through an Extensible Markup Language (XML) string format for data exchange (positional, state of motion, digital I/O) between the KRC and the external embedded target cRIO and an RSI diagram which act as the interface between the cRIO and the KRC as can be seen in Figure 3.14. Additionally, as depicted in Figure 3.15 which describes the positional correction data exchange between the KRC 4 and the cRIO under the XML string format, at every iteration of the interpolation cycle, the current position of the arm RIst and the timestamp (IPOC) of the internal clock of the KRC is sent to the external controller, where in that

case is the cRIO target. Within the same interpolation cycle, the cRIO must respond to keep the connection alive with the same timestamp and provide positional corrections RKorr in the cartesian space format which will be applied from the KRC to the end effector of the robot in the next interpolation cycle. Moreover, a boolean control variable Stop is sent to request the termination of the RSI external control and return the robot to a safe position.
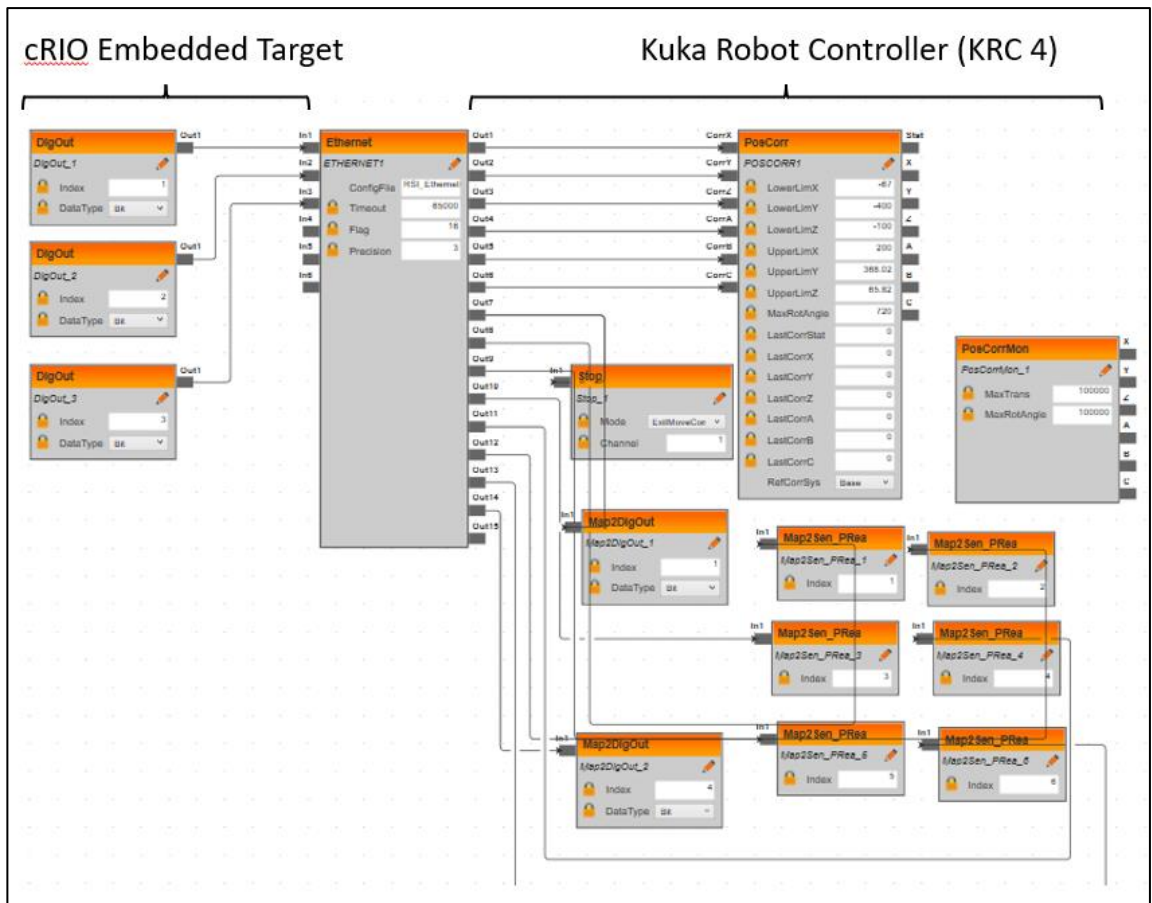
Figure 3.14. Developed RSI diagram which acts as the interface of communication between the cRIO and the KRC 4 controller for motion control of the robotic arm

In terms of positional corrections, the relative type was selected instead of the absolute, which allowed the positional corrections to be applied relative to the current position of the end-effector which was received with the latest timestamp. The relative positional corrections made it easier to apply and align the sensors' input feedback upon the robot motion, as the feedback is streamed continuously to the cRIO and aligned with the latest position of the robot end-effector. Absolute corrections were not considered as would make it difficult from a programming side to synchronise the current robot end-effector position with the sensory input (i.e. laser scanner) and compensate at the same time for a potential error that would propagate from the active motion frame and its pose when applying the sensory feedback. Moreover, the relative positional corrections are characterized by a smaller magnitude which made it safer to be applied to the KRC4 during the development and testing phase of the software module.
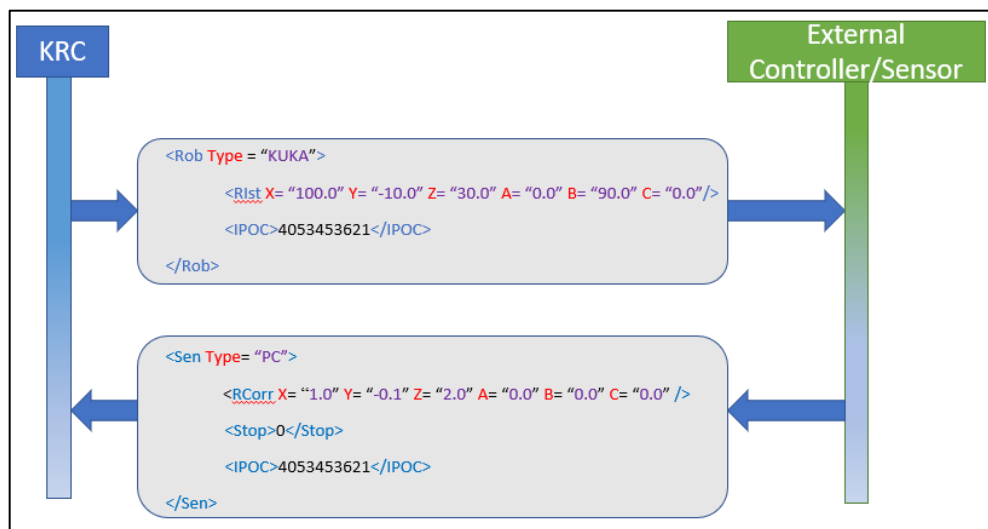
Figure 3.15. Exchange of positional corrections with XML scheme under a UDP connection of 4 ms interpolation rate, between cRIO embedded target and KRC 4

3.3.1.1.   Adaptive Motion Control

The developed trajectory control algorithm which executes at the RSI interpolation cycle-4 ms is presented in the process diagram of Figure 3.16 [136]. It consists of a Linear Controller (LC) which is based on an acceleration/deceleration cruise trajectory profile with setpoint speed **v**, Acceleration **a** is set by the user and generates the required linear increment component d_L between the current end-effector position Pc and target P_T, for each axis in the cartesian space. In Figure 3.17, an example of a linear motion is demonstrated between two points in cartesian space that are 2 m apart using a speed v=2 m/s and acceleration a=4 m/s^2.
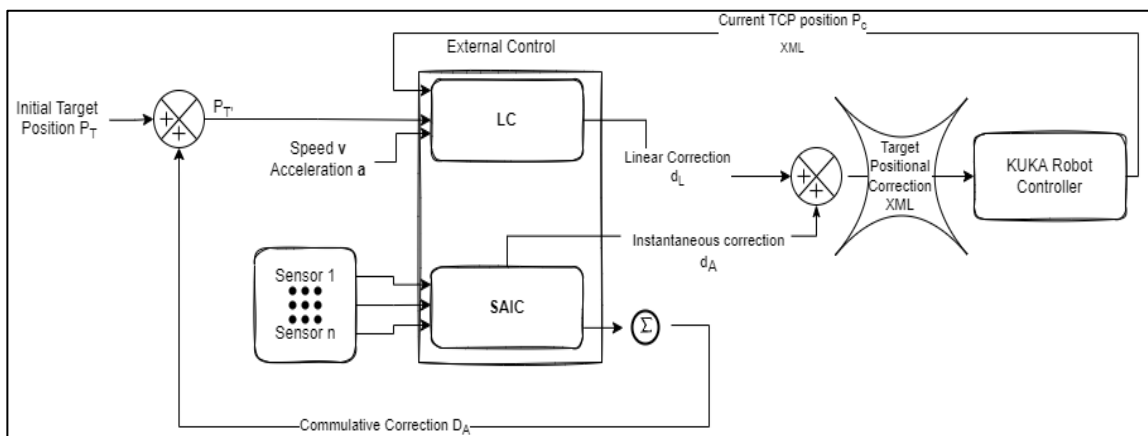
Figure 3.16. Real-time trajectory control algorithm deployed under interpolation cycle rate of 4ms driven from the internal clock of the robotic controller
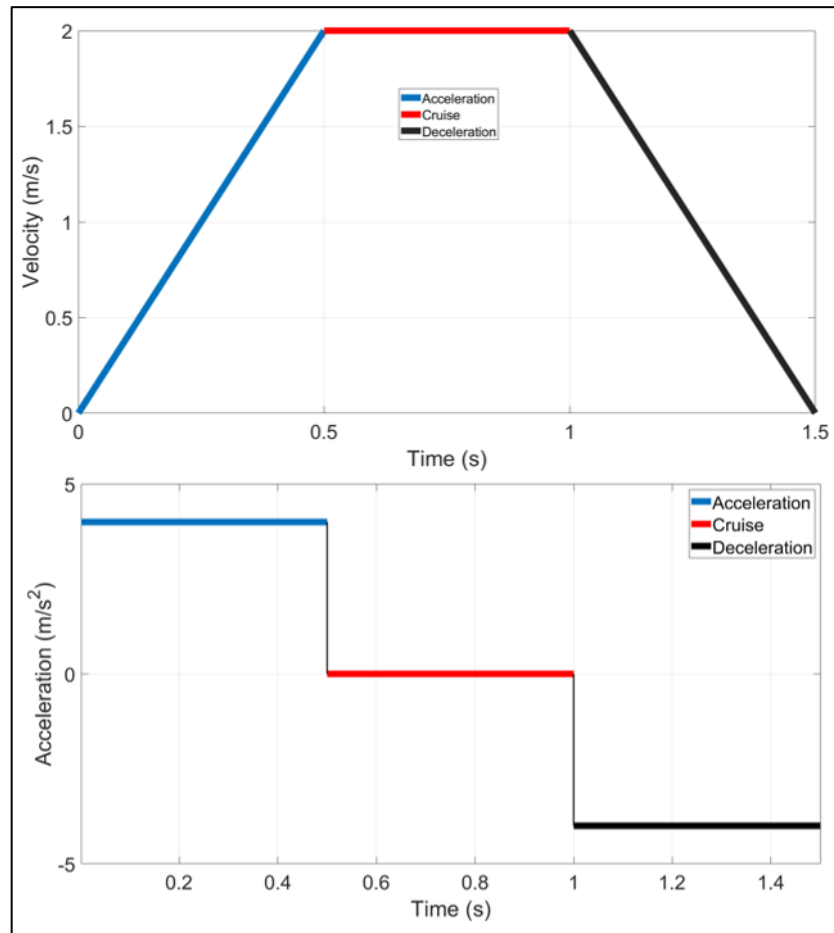
Figure 3.17. Linear motion example executed by the LC controller, for two targets that are 2 m apart, using an acceleration/deceleration profile of 4 m/s² and a cruise speed of 2 m/s

In addition, to integrate and facilitate the multiple sensors' feedback upon the LC, a Sensor Adaptive Input Controller (SAIC) translates and derives the different sensors' feedback to instantaneous adaptive correction $\mathbf{d_A}$ per axis of the cartesian space, and the absolute cumulative correction $\mathbf{D_A}$ adds to the initial target position $\mathbf{P_T}$. In that way, the cumulative correction eliminates any possible distortion to the generated LC trajectory profile due to the summed instantaneous corrections. The benefits arising from this strategy are the generation of an adaptive motion and interaction of the robotic arm to sudden changes in the environment purely on the sensor's feedback. Since the motion control takes place in

the cRIO target, avoiding storing any pre-planned path in the KRC, enables the re-calculation of the whole motion trajectory on-the-fly, whenever a parameter changes, such as the speed or acceleration of the end-effector. Nonetheless, weaving is applied during welding originating by a sinusoidal output in the transverse direction of the welding axis. As this function is characterized by variable frequency and weaving amplitude it can be altered in real-time based on the operator's choice to optimize the welding process and the whole trajectory can be re-calculated to reflect these changes. Moreover, this strategy proves efficient when the motion must adjust based on a control reference variable, such as the welding root penetration depth or the geometrical characteristics of the weld pool [94,137].

Figure 3.18 demonstrate the LC controller process diagram for the cartesian space resulting in the d_L motion component, where the process diagram for the rotations' kinematics is depicted in Figure 3.19.
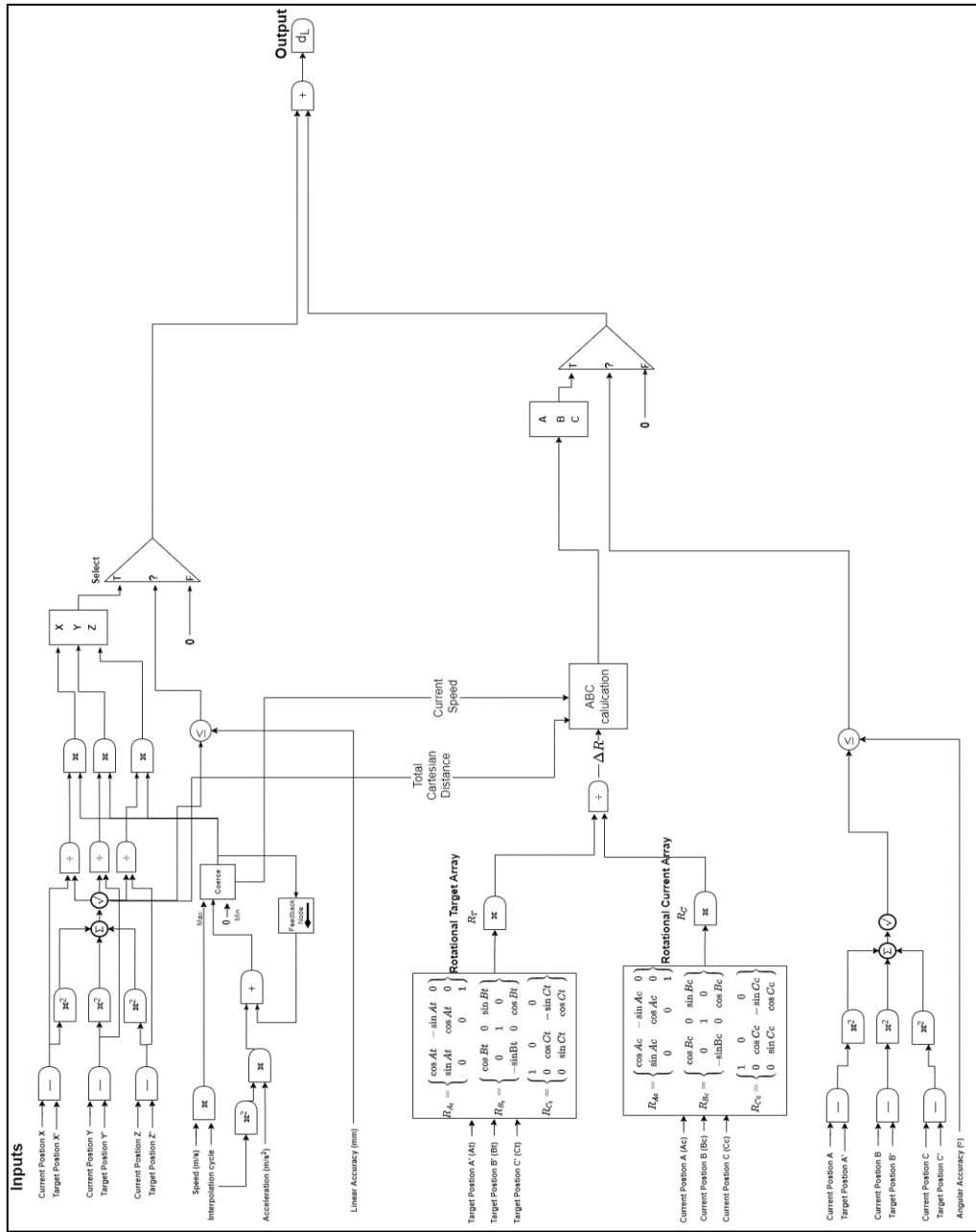
Figure 3.18. LC process diagram for on-the-fly cartesian corrections on the cartesian space based on an acceleration-cruise speed profile

64
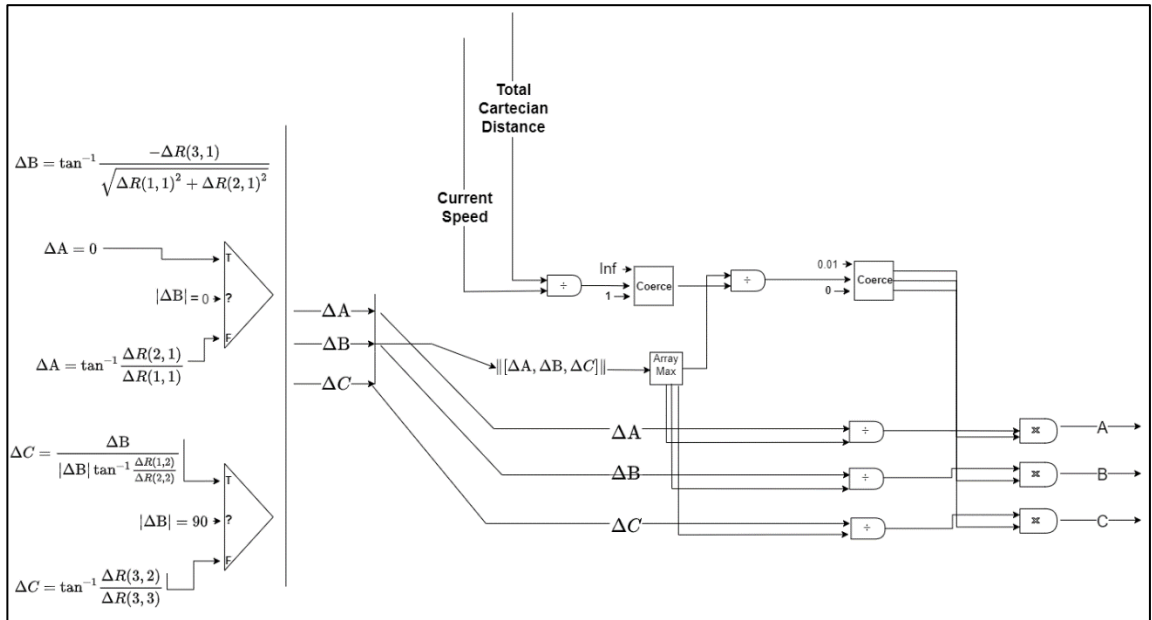
Figure 3.19. Part of LC process diagram - Calculation of A-B-C kinematics and synchronization of orientation with translation X-Y-Z

The developed sensor-enabled motion control algorithm has been integrated and deployed in several KRC 4 and KRC 2 robots in the Sensor Enabled Automation Robotics & Control Hub facilities. These range between different KUKA robotic arms, such as KR90-R2900, KR90-R3100, KR6 Agilus-R900, KR5 Arc HW R1423, including additional external axes such as rotary DKP-400V1 and KUKA KL4000 linear track to cover a wider portfolio of NDE metrology applications [136,138].

3.3.2.   Camera, Hand-Eye & TCP Calibration

To automate the identification and extraction of the pose of the welding specimen relative to the robotic arm and the adaption of its pose relative to the specimen (described in Chapter 5) required the estimation of the rigid body transformation between the RGB camera and the end-effector's TCP.

To achieve that, a TCP calibration followed by a camera calibration to compensate for lens distortion due to the not perfect alignment of the lens with the centre of the principal axis and the establishment of the Hand-Eye calibration were performed.

TCP calibration with the four-point method was used to generate accurately the pose of the welding torch relative to the robotic arm reference motion frame. A fixed pin in place was used as can be seen in Figure 3.20 to move manually the TCP of the welding torch through four unambiguous poses relative to the robot base. The estimated error from the calibration was found to be 1.03 mm after three trials.

Figure 3.20. Four different positions were used relative to a fixed pin in place, to perform TCP calibration of the end-effector welding torch

As described in Section 2.2.2.2, to extract the gHe matrix which describes the rigid transformation between the camera principal centre and the welding torch's TCP frame, a flat checkerboard of square size 22.9 mm was placed within the FOV of the robotic arm as can be seen in Figure 3.21. Thirty different poses were captured, recording (at the same time) the pose of the TCP relative to the robot base frame. These frames were used also as an input for the camera calibration (intrinsics) and distortion coefficient estimation. Camera calibration took place using OpenCV based on [110].
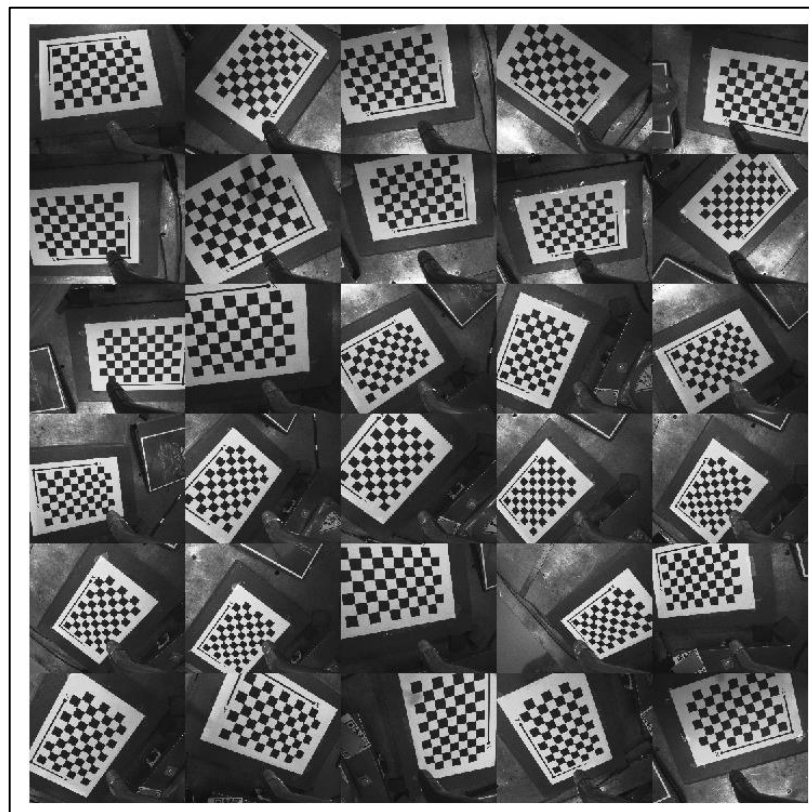
Figure 3.21. Thirty checkerboard poses were used for the Hand-Eye and camera calibration

The Hand Eye calibration matrix using the method developed on [108] resulted in the transformation matrix:

$$gHe = \begin{bmatrix} 0.0317 & -0.0028 & 0.9995 & -236.5988 \\ 0.4691 & 0.8831 & -0.0124 & -48.9340 \\ -0.8826 & 0.4693 & 0.0293 & -18.4055 \\ & 0\ 0\ 0 & & 1 \end{bmatrix}$$

The average translation and rotational error were found to be 1.4181 mm and 0.0049 rads respectively.

Camera calibration resulted in an intrinsics matrix:

$$K = \begin{bmatrix} 2.3597 & 0 & 1.1871 \\ 0 & 2.3582 & 1.0315 \\ 0 & 0 & 1 \end{bmatrix}$$

with radial distortion coefficients

$$k_1 = -0.0775, k_2 = 0.0987, k_3 = -0.0093$$

and a root mean square reprojection error of 0.2727 pixels.
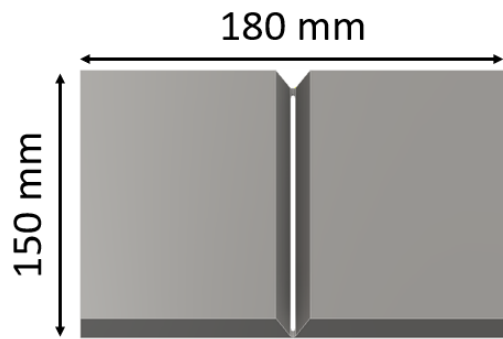
3.3.3. Laser Scanner Error Analysis and Calibration

The laser scanner attached to the welding bracket is an integral part of the robotic motion path planning and for the accurate collection of the geometric features of the V-grooves. Hence, the evaluation of its performance and the calibration of the TCP of the welding torch with the middle of the laser scanner beam is essential. In this Section an investigation takes place to identify fixed steady errors that occur during measurement of the geometric characteristics of the V-groove geometry and identify the optimum incidence and

steepness angle for inspection of a V-groove joint. The following findings are applied to Sections 5.3.4 and 5.3.5 to compensate for the average systematic errors.

A series of experiments using a pair of S-275 grade machined plates, with geometric characteristics recorded in Table 3.3 as a reference, were utilized to determine and reveal the sensor's accuracy level and the repeatability of measurements.

Table 3.3. Machined V-groove specimen for laser scanner error analysis and nominal geometric characteristics

V-Groove Nominal Features	
Groove Angle (°)	60
Root Gap (mm)	2
Root-face (mm)	1
Length of Joint (mm)	150

To determine the optimum range of height from which to extract measurements of the groove features, the welding torch was placed above the V-groove specimen, as can be seen in Figure 3.22. The robotic arm was manually 'jogged' in increments of 1 mm from the teach pendant to cover the distance range of 220-267 mm from the laser scanner to the surface of the specimen in the Z-axis. Between each point, the gap and the groove angle of the V-groove were measured using the laser scanner. Equation (3.1) is used to obtain the observed error ε from the reference values of Table 3.3 and Equation (3.2) expresses the observed error as percentage of the reference values for both gap and angle measurements.

69

$$\varepsilon = |measurement - reference| \tag{3.1}$$

$$e\% = \left(\frac{\varepsilon}{reference}\right) * 100 \tag{3.2}$$

Figure 3.23 shows the gap measured values in mm where the identified average systematic error of 0.32 mm (16% of the reference value of 2 mm) can be seen from the distance between the actual gap reference value and the measured ones. Figure 3.24 provides the percentage error result from the collected values for gap measurement along with a polynomial fit of 4th degree, indicating an optimum measuring range for the laser scanner to be 240-255 mm from the specimen and an average systematic error of 16%. The build error for the two ends of the measuring range (240 mm and 250 mm) falls from 19.5% to 13% with the minimum being 9% at 245 mm. In the same manner, Figure 3.25 and Figure 3.26 depict the results for the groove angle measurements for the same range in the Z axis, indicating an extended measuring range between 222-250 mm. The systematic error in groove angle measurements was 2.33% (1.39°), whereas beyond the 250 mm the average error rise to 3.8%.
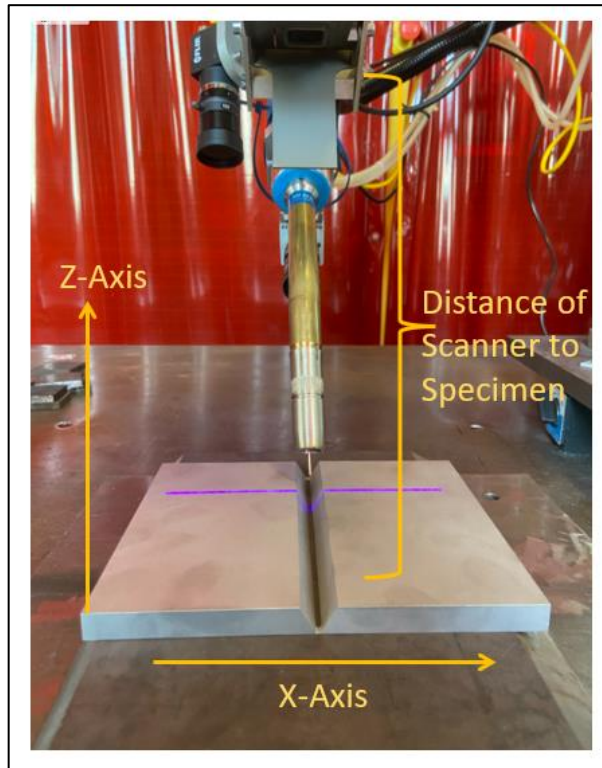
Figure 3.22. Laser performance assessment extracting the gap and groove angle measurement of the V-groove in different heights from the specimen
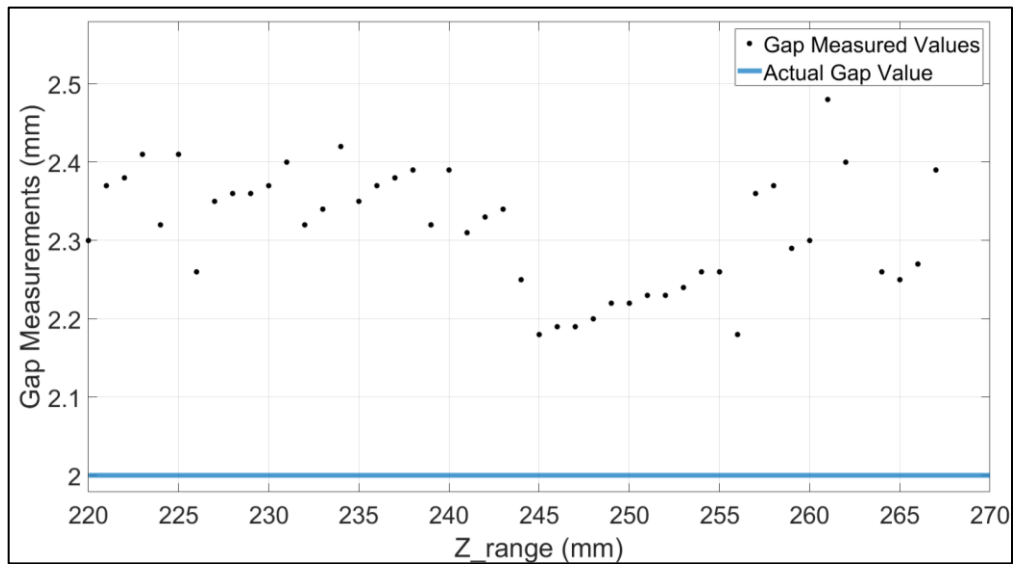
Figure 3.23. Gap measured values (mm) along the Z axis direction, compared to the actual gap value of 2 mm resulted in an average systematic error of 0.32 mm.
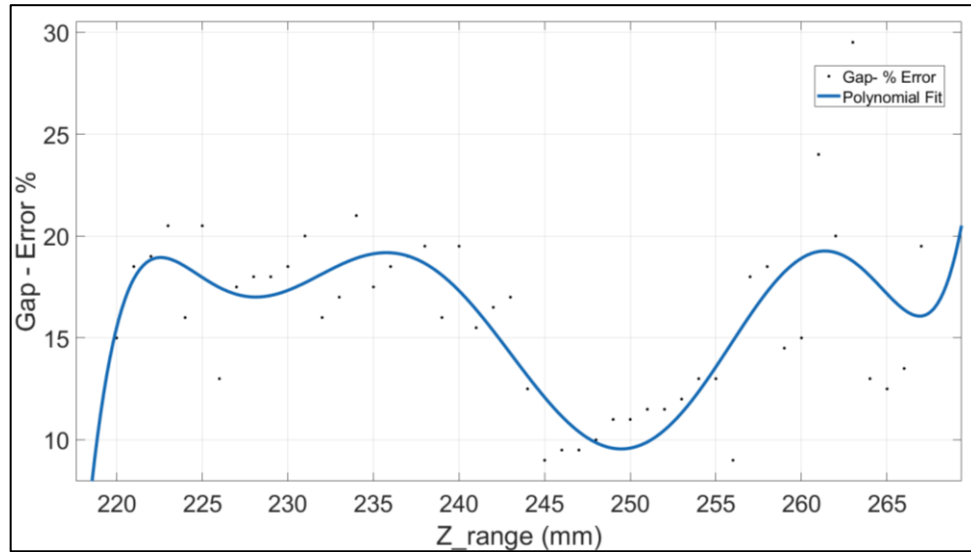
Figure 3.24. Gap measurement error (% of the refence value of 2 mm) in Z-axis direction along with a polynomial fit of 4rth degree. The optimum measuring range is observed between 240-250 mm from the laser scanner to the surface of the specimen and an average systematic error in gap measurement of 16%.
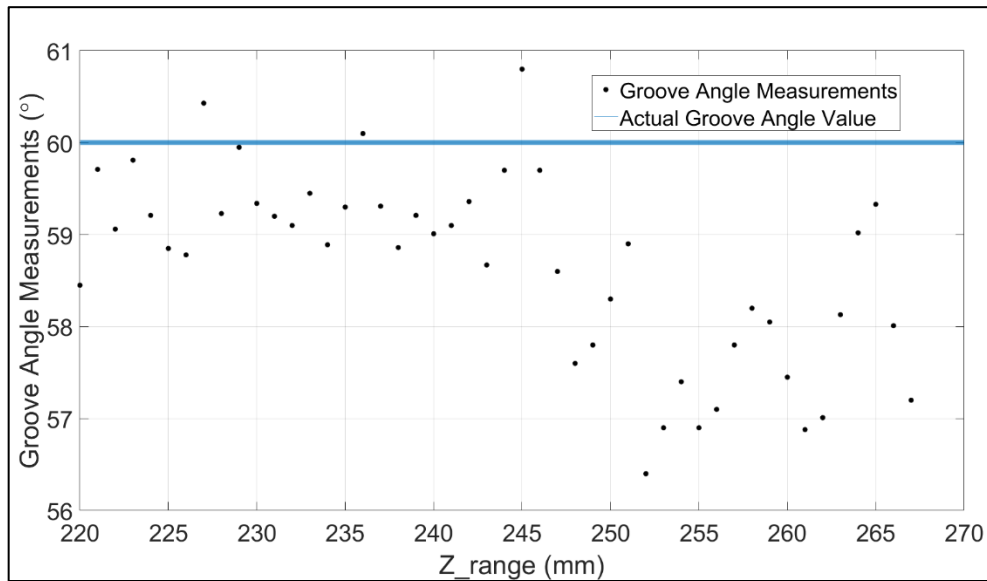
Figure 3.25. Groove angle measured values along the Z-axis direction, compared to the actual groove angle value of 60° resulted in an average systematic error of 1.39°.
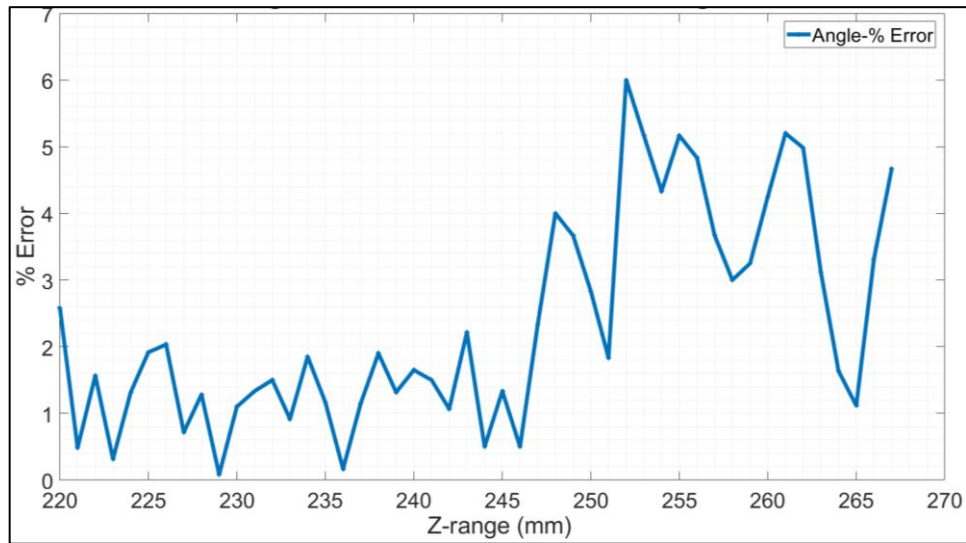
Figure 3.26. Groove angle error (% of the reference value of 60°) measurements along the Z-axis resulted in a systematic measurement error of 2.33 %.

To assess the repeatability of the laser scanner from the optimum measurement range, 50 measurements of groove angle were collected at a 245 mm distance from the laser scanner to the specimen. Figure 3.27 illustrates the % error on groove angle measurement resulting in a standard deviation error of 0.12°.
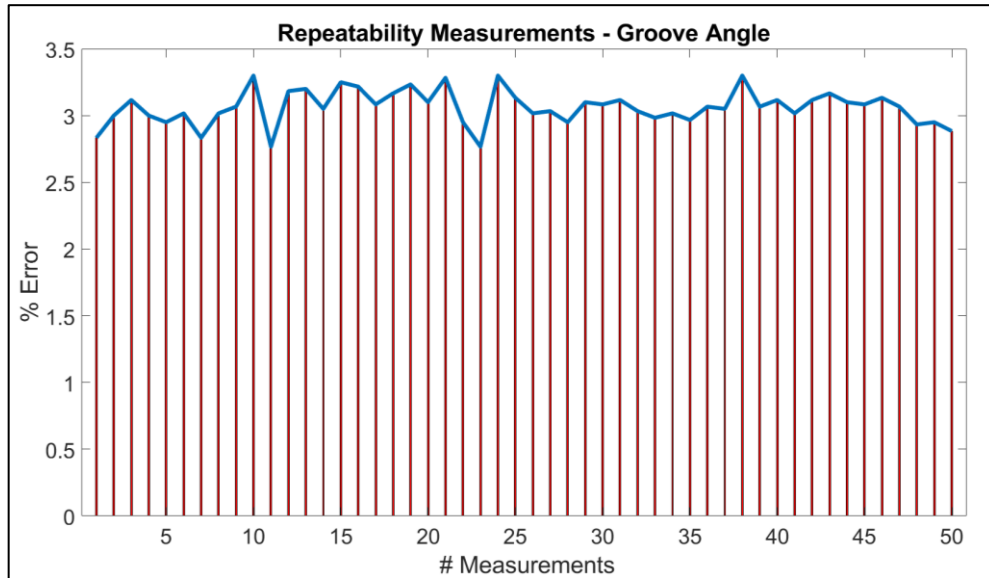
Figure 3.27. Repeatability assessment on groove angle measurement from 245 mm distance from the specimen resulted in a standard deviation error of 0.12°

Lastly, an investigation on the optimum steepness and incidence angle for inspection of the groove for features measurements was performed (Figure 3.28) based on the number of received points in the camera system of the laser scanner. As can be observed in Figure 3.29 and Figure 3.30, it was found that for both the incidence and steepness angle there is a feasible range of 18° around the vertical axis for collecting reliable measurements. Exceeding these angle limits the number of received points drops which marks the flood of camera sensor from the received reflections.

74
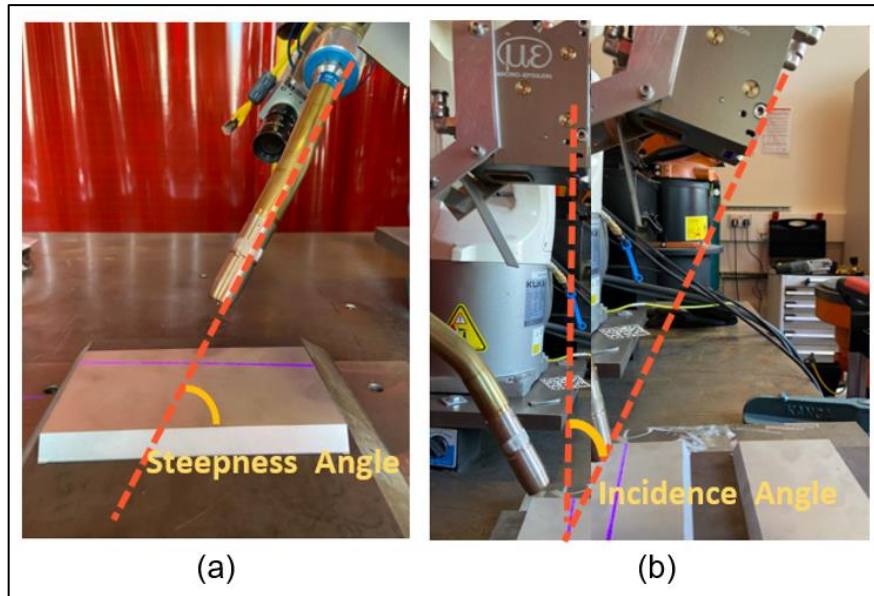
Figure 3.28.Feasibility study to identify optimum laser scanner steepness (a) and incidence angle (b) for measurements extraction.
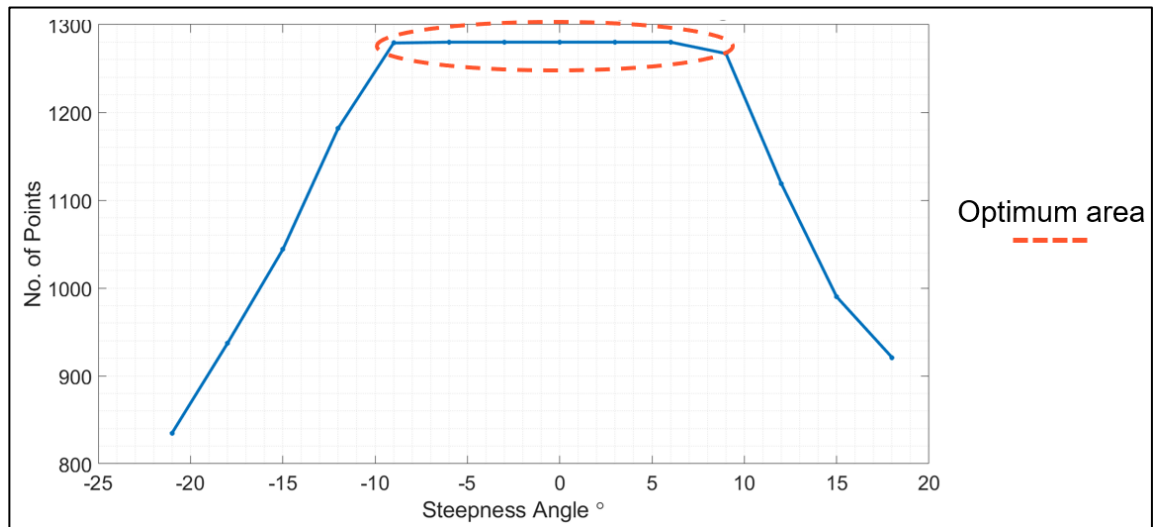
Figure 3.29. Laser scanner performance analysis on the steepness angle of the laser scanner and the V-groove specimen
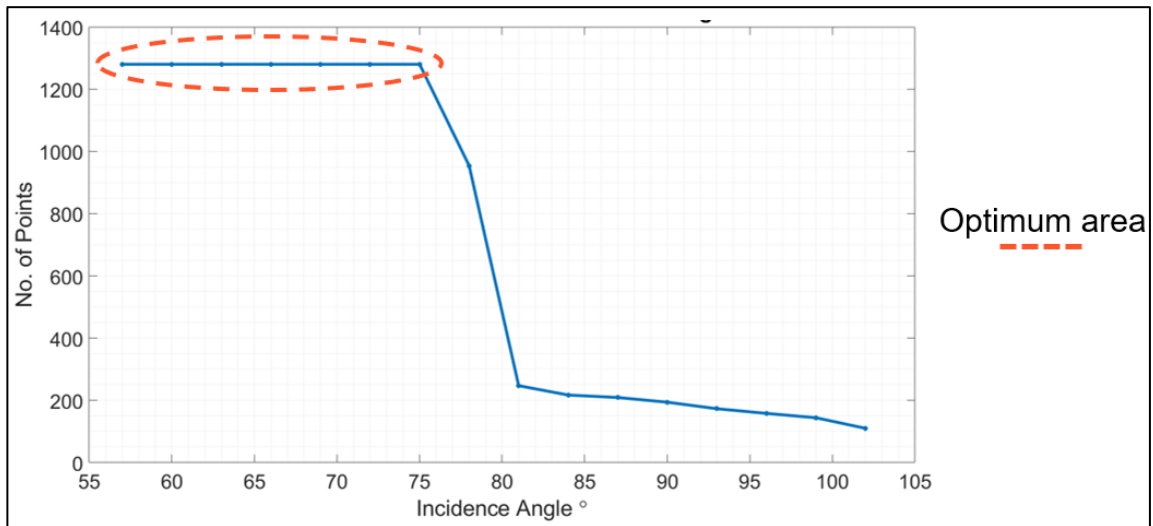
Figure 3.30. Laser scanner performance analysis on the incidence angle of the laser scanner and the V-groove specimen

To calibrate the TCP of the welding torch (tip of the wire) with the middle of the laser beam, the robotic arm is first placed manually inside the V-groove. Based on the above analysis, a 0° steepness angle, and a 10° incidence angle along with an offset of 245 mm of the scanner from the surface are used to calibrate the scanner. The program of the scanner to identify the V-groove start and end points is used to align the TCP with the seam centre by ensuring that the wire of the torch lies in the middle of the seam and there is an equal distance between the left and right indication of the seam from the centre of the groove as can be seen in Figure 3.31. Calibration along the X-axis receives the value of 2.15 mm. Although the welding torch bracket was designed in such a way to align the welding torch's TCP with the middle of the laser scanner, a mechanical machining error still necessitated the need to adjust this calibration value internally in the scanner.

76
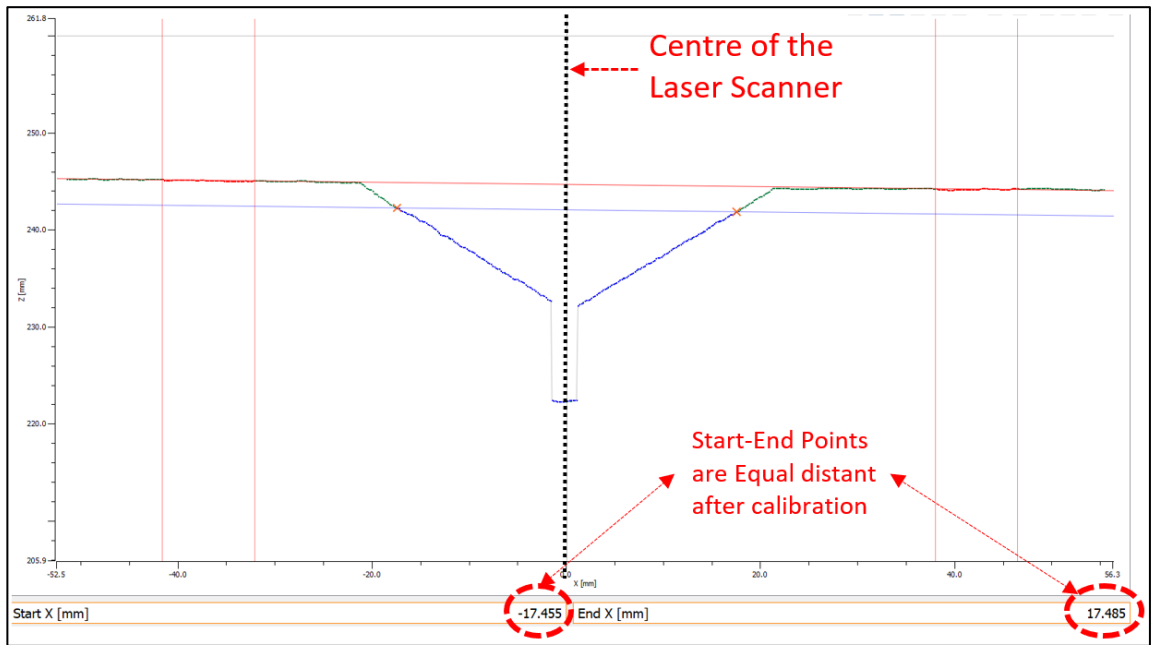
Figure 3.31. The laser scanner calibration process results in equal Start-End points, compensating for the inherent machining errors on the bracketry

3.4. Conclusion

The development of a holistic sensor-enabled robotic welding system was presented in both hardware and software terms. The transformation of a commercial off-the-shelf robotic arm to a welding robot enabled the use of a small commercial robot designed initially to assembly electronic components and perform light duty tasks into a welding system for confined spaces, suitable for the needs of the industrial partner. Following that, the integration of the welding robot into the modularized setup for automated MAG welding is described. The system architecture is based around an embedded real-time cRIO target, utilizing a developed LabVIEW software to achieve reliable parallel handling of signals between the welding and robotic equipment. An integral part of this automated welding system is the development of a real-time external motion control module able to

generate, deploy and adapt the robot kinematics relying solely on a sensor-guided approach, eliminating the need for manual teaching and the use of CAD drawings. Lastly, the establishment of the Hand-Eye calibration along with the optical sensing feedback from the laser scanner allows the welding robot to realize automated identification and adaption of the robotic arm relative to the welding specimen. The above developments are novel elements within this thesis (Section 1.4) which were a key enabler for the successful deployment of automated robotic multi-pass arc welding for single-sided V-grooves.

Chapter 4

A Cost-Function Driven Adaptive Welding System for Multi-Pass Robotic Welding

4.1. Introduction

A dynamic process such as welding, which is challenging to parameterize and to control [139–142], must meet the demand for high production rates, precision, and consistent quality. Automating the process of welding can alleviate issues of increased production demand repeatability, and quality. However, manual teaching of welding paths and welding parameters for multi-pass robotic welding still is a cumbersome and time-consuming task, which decreases the flexibility, adaptability, and potential of such systems.

The realization of a fully automated robotic welding approach demands the development of a system which combines sensor-driven robotic motion alongside with multi-pass sequence planning for the weld joint geometry. Sensor-driven motion introduces flexibility and adaption to the environment where the welding system operates, without the need of special fixtures, reprogramming of motion and customized welding cells.

Sequence planning of multi-pass welding is imperative for automation of welding in the shipbuilding and offshore sector due to the requirement of the thickness of the joints.

This chapter presents a multi-pass welding system that enables automatic planning of the complete multi-pass sequence with different welding parameters per layer. A novel cost-function concept is introduced, which permutates and identifies the welding parameters for each layer through a user-initiated weighting, to deliver the minimum: number of passes; filler material; and, welding arc time, based on application requirements. As such, this approach adapts to varying single sided V-groove geometries, without human intervention, and results in populating the number of layers and passes. These developments are demonstrated alongside a flexible 6-DoF sensor-driven robotic welding demonstrator and verified experimentally by deploying phased array ultrasonic inspection on the manufactured weldments.

4.2. Current State-Of-The-Art in Multi-Pass Sequence Planning

Mathematically describing and approximating the shape geometry of the deposited welding beads requires the development of algorithms to generate sequences of welding parameters and as a result robotic motion paths. In the following works, welding beads are represented as parallelograms and trapeziums geometric shapes, since often the cross-section of these weld beads match these shapes visually.

Using the same welding parameters for all the deposited weld beads, the authors in [28,143,144] simplified the welding sequence generation. Adopting the same welding

parameters for each welding pass, for all the layers, the method of equal height was utilized in [28,143]. This method assumed that every layer had the same height, which could be argued as partially true since the width of the groove increases between the bottom and the top surface of the specimen. Similarly, in [144], the welding sequence schedule was generated utilizing the same welding bead for all the filling layers. This assumption was held since the cross-section area of the weld bead remains constant under the same welding parameters, resulting in the equal area method.

The number of passes per layer can be minimised by selecting different welding parameters between the layers, and the groove can be filled faster than using the same weld bead for each welding pass. In [145], authors related the cross-section area of the weld bead with the value of the wire feed speed, welding torch's speed and diameter of the wire. Depending on where the weld bead was deposited in the groove it was approximated as a trapezium or a parallelogram. This method prompted the user to enter the desired welding parameters per layer and number of passes, generating the robot path and position of weld bead in the groove to aid automation, while mimicking manual welding approaches. The approximation of weld beads as a parabola is discussed in [146]. The welding schedule algorithm assumed that the width of every weld pass in the same layer remains constant and the chosen bead maximizes the occupied cross-section area to result in the minimum number of passes. However, the maximum allowed height for every additional welding layer was not considered, where the user decides the next layer's height as the groove is filled with passes. This call for user's input without the flexible character of adaption, makes the multi-pass welding sequence planning a semi-automatic procedure.

Table 4.1 depicts the current advancements on the state-of-the-art in multi-pass sequence planning along with their limitations:

Table 4.1. Relevant works in multi-pass weld sequence planning and limitations

Relevant works	Different welding parameters per layer	Adapting different welding parameters to varying V-groove geometries	Cap passes planning	Post-Trial Inspection Verification
C.D. Yang et al.[28]	✘	✘	✘	✘
C. Yang et al. [143]	✘	✘	✘	✘
T.-Y.Huang et al.[144]	✘	✘	✓	✓
H. Zhang [145]	✓*	✓*	✘	✘
S.J. Yan et al.[146]	✓**	✓**	✘	✘
This Body of work	✓	✓	✓	✓

* The user prompts to enter the welding parameters per layer. In that way, it can select different welding parameters for different V-groove geometries.

**Welding parameters are provided from a database where the user decides for the initial number of passes and layer's height. The chosen dimensions of the bead must satisfy the stored configurations in the database

4.2.1.   Research Gap

Based on the current state of the art, there is a lack of an automated technique to identify the combination of the welding parameters per layer and the number of welding layers to fill the V-groove geometries without user's input. Zhang et al. in [145] prompted the user to decide for the welding parameters per layer, while in [28,143,144] the same welding bead was utilized in each pass of every layer, which is not efficient in terms of welding time and required heat input. The maximum height and width of the planned passes were not investigated, and as a result, the chosen weld passes could have an irregular cross-

section area relative to the size of the whole groove. Two common points in the above approaches was the use of backing to deposit the root pass, and the fact that the hot pass was treated as a regular filling pass when more heat input is required than the first pass to fill any inconsistencies caused by improper penetration and fusion of the root pass with the base plates [29]. Moreover, cap planning and inspection for defects were only performed in [144] where a micrograph analysis revealed lack of sidewall fusion.

Building and adapting on the work reported in [145], the following advancements and work packages are developed in this Chapter, where Figure 4.1 summarizes and illustrates the novel contribution of the automated multi-pass welding system:

- The observed research gap in the literature was addressed by developing an algorithmic technique to automate the sequence path planning with different welding parameters per layer and identifying the number of passes per layer and number of layers irrespective of the butt joint geometric characteristics.

- A logic is integrated to allow the adaption of the welding parameters for varying single sided V-groove geometries (groove angle, gap size, bevel height) enabling the automated robotic weld path planning. This advancement can eliminate additional time to re-program from scratch the robot motion when the joint geometry changes due to design or operational requirements.

- Additional work is performed to formalize the need for cap planning in the final welding layer for varying V-groove geometries.

- The optimized solution of the sequence of welding parameters per layer is shaped further by introducing the dynamic concept of the cost function. This delivers the combination of welding parameters that will produce the minimum number of passes in the minimum arc welding time, with the minimum spent filler material while taking care of the restrictions on allowed height and weaving width of the weld bead. The size of the bead can increase the residual stress between weld passes, resulting in cracks and increased distortion of the weldments [147,148].
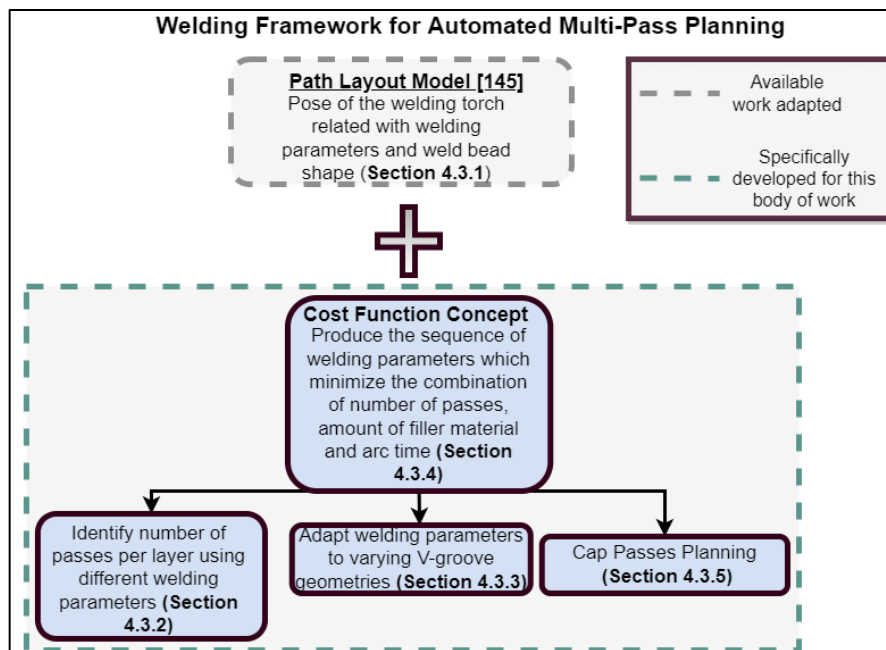
Figure 4.1. Highlighted is the available adapted and newly developed work for this chapter with direct reference to their corresponding section in the chapter

4.3. Proposed Automated Welding System

A mathematical model, relating the cross-section area of beads with the welding parameters, pose of the torch and weaving width, was adopted from [145] and built upon to allow full-process automated welding parameter generation, adaptation and robotic path

generation. The flowchart presented in Figure 4.2 describes each step of the multi-pass welding system as well as the required user input. The following sections in this Chapter explains in detail the implementation of the different steps along with the notation used in the flowchart.
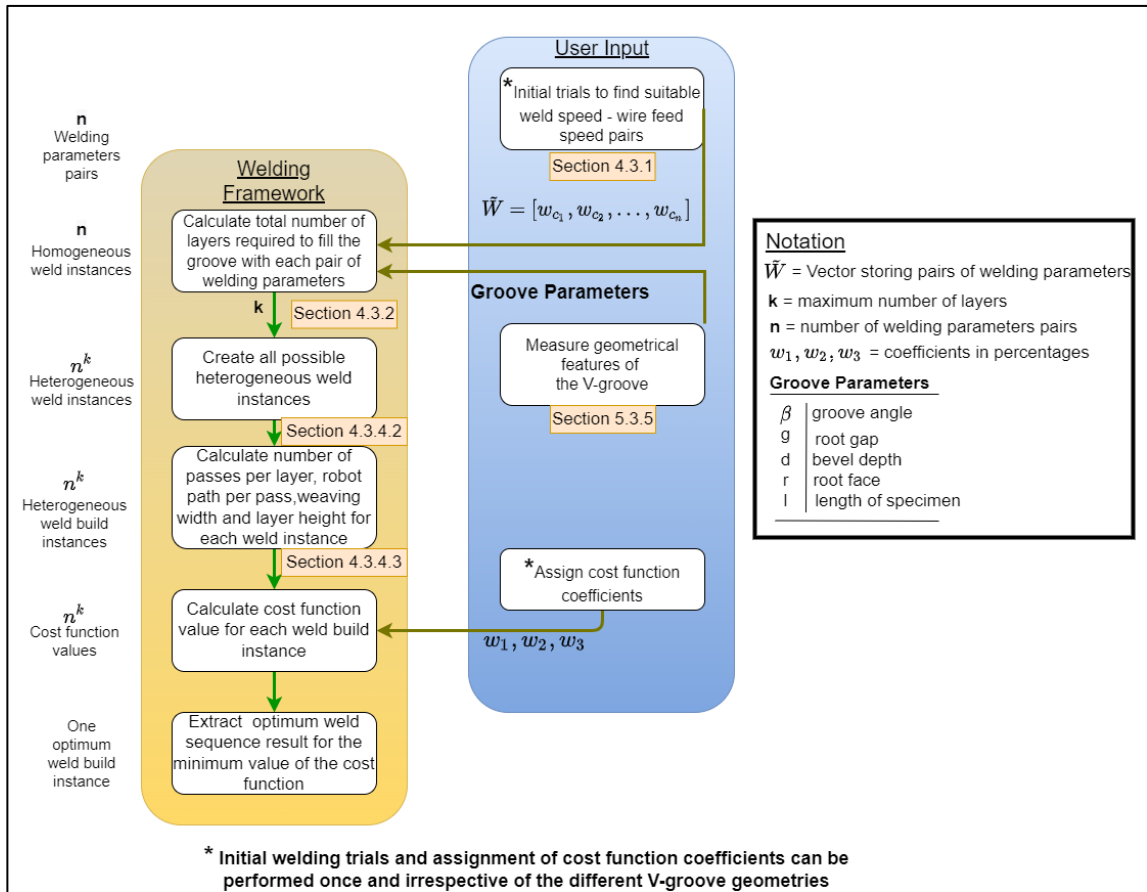
Figure 4.2. Flowchart presenting the welding system process and the required user input

4.3.1. Cross Section Area and Efficiency Coefficient

An integral part of the multi-pass sequence strategy is the prediction and approximation of the cross-section area of the deposited weld bead based on the welding parameters. The cross-section area defined with variable S (mm^2) is represented by a trapezium or

parallelogram shape depending on where it is deposited within the groove [145] and is

given by Equation (4.1):

$$S = \frac{\pi \cdot u \cdot D^2}{2 \cdot v}$$

(4.1)

where u = wire feed speed (mm/s), D = diameter of the wire (mm) and v = robot welding

speed (mm/s). Every pair of robot and wire feed speed is provided as a welding

configuration vector, $w_c = [v, u]$. To reflect the material loss during welding, due to the

efficiency of the filler wire, spatter and heat transfer, the coefficient a_H was introduced,

to give Equation (4.2) based on [28,143]. The coefficient a_H was determined through

experiments and subsequent welding trials as it is described in Section 4.4.1.

$$S = \frac{a_H \cdot \pi \cdot u \cdot D^2}{4 \cdot v}$$

(4.2)

4.3.2.   Assess the Number of Layers and Passes

The automatic generation of the number of layers and passes required was obtained by

building on [145] where the user was prompted to provide the total number of layers and

passes. The root and hot pass were not part of this routine, as they each constitute one

welding pass. The number of welding passes for every additional layer is now

automatically generated based on the parameters shown in Table 4.2 and driven by

restrictions on the maximum weaving width and the range of allowed height of every weld

bead on the layer. This is core of the developed algorithm, highlighted in the provided

flowchart of Figure 4.3 with the green dotted lines.

Table 4.2. Inputs of the algorithm that produce the number of passes per layer

Parameter	Description
w_c	Vector of welding parameters (see Section 4.3.1)
S	Array of values of cross-section areas of already deposited weld beads
m_i	Number of already deposited passes per layer
i	Current layer number
a_H	Deposition coefficient (see Section. 4.4.1)
δ	Weaving factor used to restrict weaving width (see Section 4.4.1)
β	Groove angle of V-groove
g	Root gap length
D	Diameter of filler wire

Maximum weaving width and accepted range of height for a weld pass are not defined explicitly in welding standards but is guided mainly from the requirements of the application and is recorded as part of the WPS (Welding Procedure Specification) document. However, the narrower and taller the bead is, the more challenging is to perform subsequent welding passes and to achieve proper fusion with the sides of the weld bead. On the other hand, weld beads with a small height lead to more passes to fill the remaining groove, and consequently more heat input which is not efficient in terms of manufacturing time. Preliminary experimental trials deployed with the robotic setup presented in Section 4.4 indicated that the acceptable range for height of each layer could be between 2 mm and 5 mm. Moreover, the maximum weaving width was limited to three

times the diameter of the welding wire ($3 \cdot D$) used. Excessive weave width increases heat

input towards inline cracking and the chance for lack of fusion with the sidewalls rise.
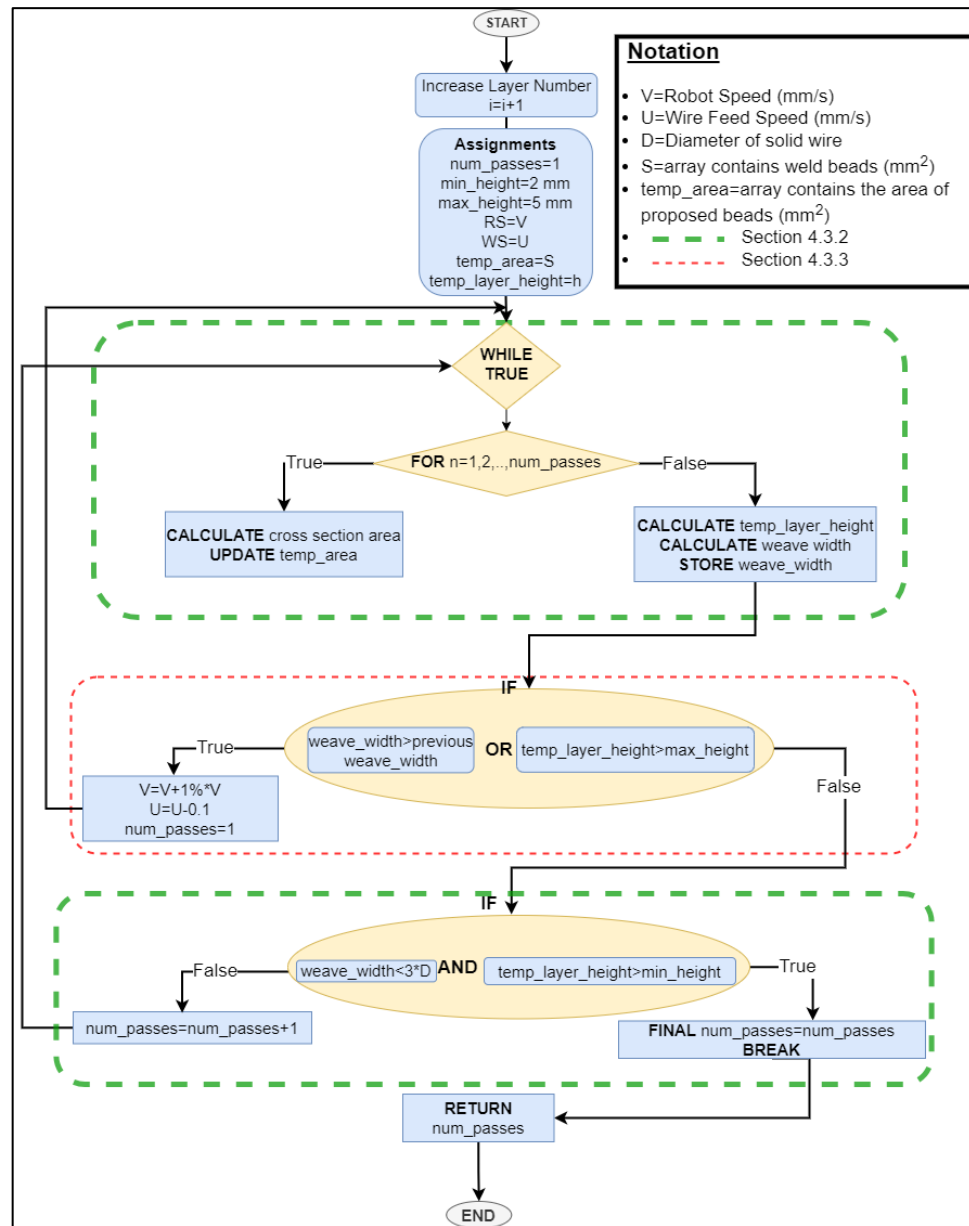
Figure 4.3. Process flowchart of the developed algorithm. The algorithm also adjusts the welding parameters based on the imposed restrictions of bead height and weave width.

4.3.3. Adapting Welding Parameters to Varying V-Groove Geometries

The process marked with red dotted lines in Figure 4.3, assists in generating and adapting the number of passes per layer for varying V-groove geometries, irrespective of the characteristics of the butt joint (bevel angle, height, root gap). Since the operator's input is not required for each layer, to guarantee that the restrictions on height and weave width are satisfied, a logic is encapsulated to adapt the existing welding parameters.

Investigating the variation on the geometric characteristics on the V-groove joint, there is a possibility that the cross-section areas of the produced welding beads based on the existing welding parameters will never satisfy the restrictions on height and weave width for the welding beads. Violating the restrictions stems from the rise of the width of the groove from bottom to top and at which height previous deposited layers resulted within the groove. More particularly equations from [145] were used to calculate the height of the layer and the required weaving width of passes. Both depend on the previous layers' height and covered area from already deposited weld beads. For every new layer, the algorithm initially picks a welding parameters pair and assigns one pass which has a weaving width that covers the whole width of the groove and the smallest height required to occupy the whole layer. In the next iteration a new pass will be added, so the weaving width will decrease and because more passes stack together the height of the layer will increase. However, in some circumstances adding more passes in that layer may never

satisfy the restrictions as the initial cross section area of the welding pass was too big and the height of the layer will keep increasing.

To counteract this action and always satisfy the imposed size limits, the cross-section area formed from the existing welding parameters must decrease. Hence, once there is a violation, the provided welding configurations are adjusted in every iteration by 1% of the robot speed and 0.1 m/min of the wire feed speed. These incremental proportional changes (1%, 0.1 m/min) were selected, as are the minimum allowed increments in the robotic and welder equipment setup used for the experimental proof of concept (Section 4.4). If larger increments were selected, the restrictions would be satisfied in fewer iterations. Still, the cross-section area of the welding passes would be much different from the welding parameters that the user initialized at the start of the system and at the end may not be accepted if the deviation is outside of the accepted window of the WPS document. It must be stressed also that large cross-section area beads produced from increased wire feed speed, may fill faster the volume of the groove, but will require more iterations to adjust the welding parameters if the restrictions are violated. These variations which were validated from experimental procedures consist of a groove angle further of 95°, root gap length more than 2 mm and total bevel height of 15 mm.

4.3.4. Cost Function Concept and Sequence of Welding Parameters

In manual welding, the sequence of welding parameters per layer is not always known beforehand and depends on the welder's experience to select and adjust these parameters

before each welding pass. Therefore, when considering automated welding, the total number of layers, welding passes, arc time and the amount of filler wire material that will be required are often unknown variables in the multi-pass weld planning procedure. As these parameters drive the direct costs of welding, they can be used to form a cost function. Such a cost function can be assigned by the operator and could be minimized, leading to the most optimum welding procedure based on the business requirements and operational plan.

For a given V-groove geometry and a produced sequence of welding parameters, the proposed cost function is the weighting summation of the number of passes, the amount of filler material and total arc time required. It takes the form of Equation (4.3):

$$C(w_1, w_2, w_3) = w_1 \cdot passes + w_2 \cdot material + w_3 \cdot time \qquad (4.3)$$

where w_1, w_2, w_3 are the weighting coefficients which must add up to 100% in total. In this proposed methodology the weighting coefficients are set by the operator, based on which parameter they would like to minimise the most.

The value of number of passes per layer are given from the algorithm described in Section 4.3.2. The arc time and amount of filler material per layer are given by Equation (4.4) and Equation (4.5) respectively:

$$Arc\ time/layer = \sum arc\ time/pass$$

$$(4.4)$$

$$Arc\ time/pass = Length\ specimen/v$$

$$Filler\ material\ /\ layer\ =\ \sum material/pass$$

$$material/pass\ =\ (wire\ weight\ /mm)\ *\ length\_wire \qquad (4.5)$$

$$length\ of\ wire\ =\ (arc\ time\ /pass)\ *\ u$$

To automate this process, the user initially defines the welding parameters that will be used in the welding system providing in pairs of w_c vectors, as mentioned in Section 4.3.1, and are feasible with respect to the welding equipment regarding heat input and welding speed. It must be noted that utilizing beads with increased cross-section area by increasing the wire feed speed u and keeping constant the robot speed v, will result in fewer passes to fill the V-groove volume. However, the welding parameters must be pre-approved from the relevant WPS document regarding the properties of the joint material. Increased wire feed speed, and as a result increased current, can result in excessive heat input, damaging the internal structure of the material and generating defects.

These welding configurations are stored as a vector $\widetilde{W} = \left[w_{c_1}, w_{c_2}, \dots, w_{c_n}\right]$ where $n \in Z^+$ is the length of the vector and shows the number of different welding parameters. The vector $\widetilde{W}$ remains constant for all the varying V-groove geometries that welding is scheduled.

4.3.4.1.   Homogeneous Weld Instances

Firstly, the total number of layers that can fit in a provided V-groove geometry has to be estimated based on the assigned vector $\widetilde{W}$. Following the root and hot pass which are not generated from the developed welding system, the number of welding layers for the remaining volume of the groove can be found by iterating through $\widetilde{W}$, and creating instances of the same groove geometry where each layer is assigned the same welding configuration.

This can be seen in Figure 4.4 where the generated samples of the V-groove geometry can be seen. The number of passes per layer is found, utilizing the algorithm described in Sections 4.3.2 and 4.3.3.
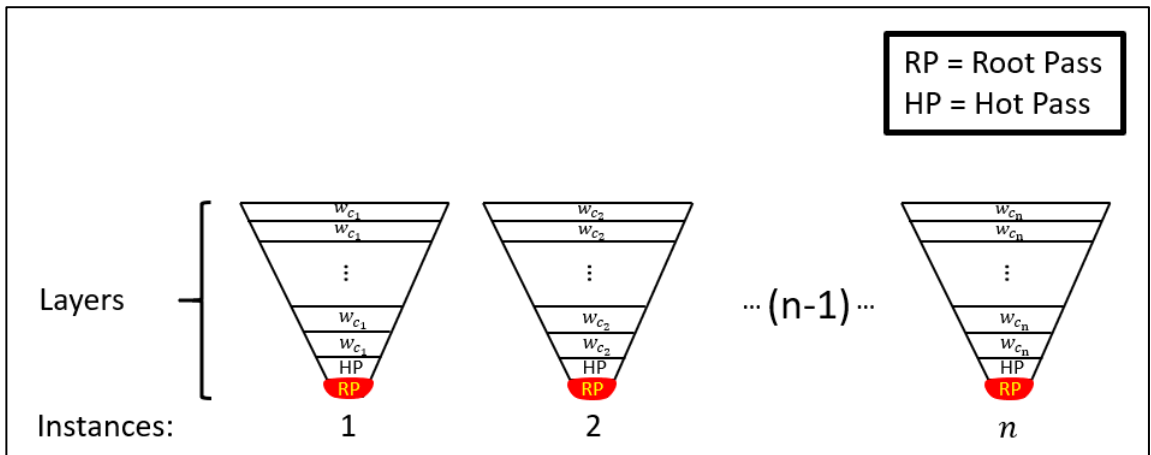
Figure 4.4. Highlighted are the initial generated instances which investigate the maximum number of layers that fitted among all the $\boldsymbol{n}$ different welding configurations in $\widetilde{\boldsymbol{W}}$ vector.

The w_c welding configuration per layer is adjusted if the restrictions of height and weaving criteria are violated. Therefore, n different instances are created for the same

geometry and the maximum number of layers that are found from this iterative process is recorded and defined as $k \in Z^+$.

4.3.4.2. Heterogenous Weld Instances

Permutations within iterations are utilized to determine all the different ways that the welding parameters can be assigned for the maximum number of layers found, while addressing the need for varying welding parameters as the layers are generated. The number of permutations can be found using Equation (4.6), and these are populated schematically in array P, as depicted in Figure 4.5.

$$P = \begin{bmatrix} W_{C_1} & W_{C_1} & \cdots & W_{C_1} & W_{C_1} \\ W_{C_1} & W_{C_1} & \cdots & W_{C_1} & W_{C_2} \\ W_{C_1} & W_{C_1} & \cdots & W_{C_1} & W_{C_3} \\ \vdots & \vdots & \vdots & \vdots & \vdots \\ & & n^{k-3} & & \\ \vdots & \vdots & \vdots & \vdots & \vdots \\ W_{C_n} & W_{C_n} & \cdots & W_{C_{n-1}} & W_{C_{n-1}} \\ W_{C_n} & W_{C_n} & \cdots & W_{C_{n-1}} & W_{C_n} \\ W_{C_n} & W_{C_n} & \cdots & W_{C_n} & W_{C_n} \end{bmatrix}$$

Layers →

Instances of V-groove geometry ↓
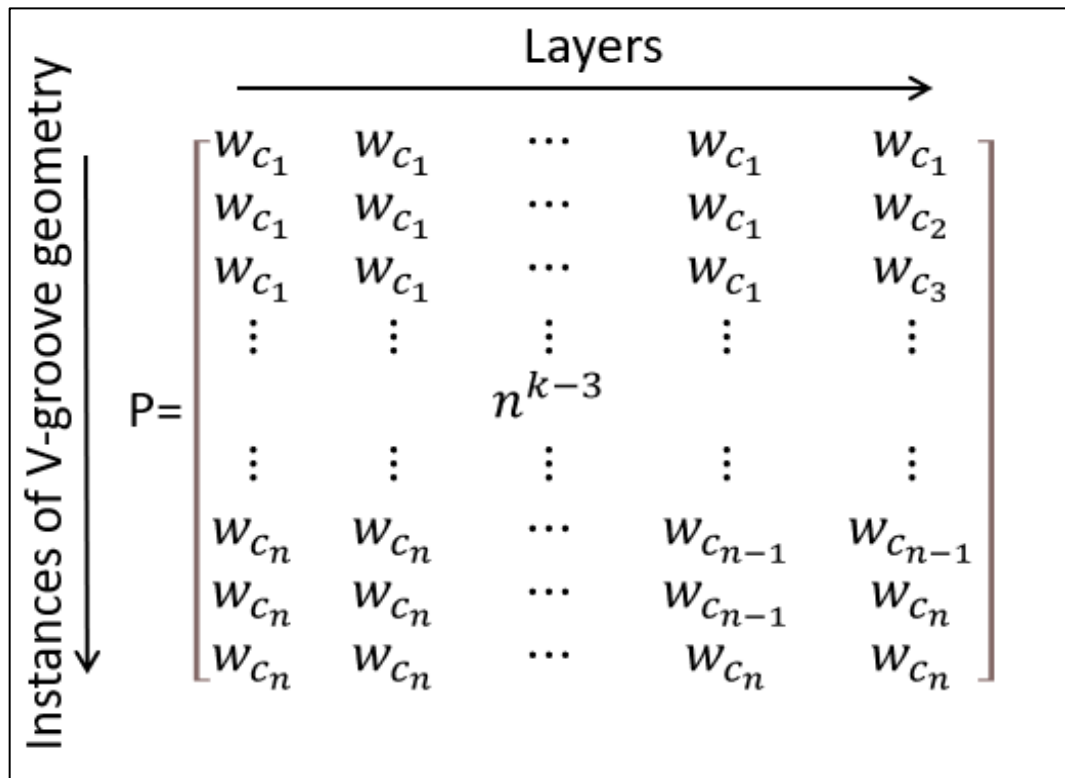
Figure 4.5. Array P is generated from populating the welding parameters per layer for n different welding configurations w_c using permutations within iterations.

Iteration is used since every new layer can have the ability to get assigned the same welding configuration w_c as the previous layer.

$$P_n^k = n^k \text{ where } k, n \in Z^+ \tag{4.6}$$

For example, if $n = 4$ different w_c welding configurations are assigned to the system through vector $\widetilde{W}$ and if $k = 6$, which is found from the process described in Section 4.3.4.1, then $4^6 = 4096$ different sequences of welding parameters (for the same groove geometry) can be generated, utilizing only four different welding configurations w_c (Section 4.3.4).

However, not all the generated welding sequences are unique, since the value k that was found is a rough estimation of how many layers can fit in the V-groove when all the layers have the same welding parameters. The restrictions on height and weaving width that are imposed when a new pass is added to the layer affect the height where every layer will reach within the V-groove. The algorithm reported in [145] that calculates the weaving width of a pass is guided from the summation of the cross-section areas of previous beads and the height where the last layer reached. Contrasting this calculation against the V-groove shape, where by definition the width of the groove increases from bottom to top and more passes can fit per layer, the number of total layers at the end may not be equal to the estimated value k (see Section 4.3.4.1). Besides, layers with welding parameters that follow a swapped sequence order from the permutations (i.e. $[w_{c_1} - w_{c_2} - w_{c_1}], [w_{c_1} - w_{c_1} - w_{c_2}], [w_{c_2} - w_{c_1} - w_{c_1}]$) and have different cross section area, may not reach the same height as they can be deposited in a different height, offset from the

root face. As a result, the restrictions can generate a different number of passes in these instances. The existence of these cases requires one additional layer, and this depends on the sequence of welding parameters that were populated during the formation of these previous layers. For that reason, permutations within iterations are investigated for $k + 1$ possible welding layers with n pairs of w_c, that represent the welding configurations and compensate for these additional cases.

4.3.4.3. Weld Build Instances and Cost Function Calculation

Populating the array P with dimensions $n^k \times k$, as was shown above in Figure 4.5 which stores the permutations of different welding sequences for a given V-groove geometry, is essential to finding all the values of the cost function. A V-groove instance filled by layers is generated, where each layer following the root and hot pass, gets assigned the welding parameters per column of the array P. For every generated layer the algorithm analysed in Section 4.3.2, is used to generate the number of passes where the amount of filler wire, the arc welding time and the number of passes is recorded based on Equation (4.5) and Equation (4.6). New layers are added until the top surface of the V-groove is reached and the robotic path per pass is generated based on the work described in [145] and welding parameters assigned per layer. Regarding the arc welding time; an optional time of 10 seconds should be added after depositing each pass to avoid contamination with subsequent passes. Equation (4.3) is used to calculate the value of the assigned cost function. This process is repeated for all the rows of array P, until n^k weld build instances are populated and those that resulted in the same cost value are rejected.

For example, assuming the annotated geometry in Figure 4.6, the proposed solution for the sequence of the welding parameters derives from the minimum value of the cost function $C(60\%, 10\%, 30\%)$. Schematics in Figure 4.6 (a) and (c) represents the number of layers, along with the generated passes and pose of the weld torch. The values of the cost function for all 1071 generated unique instances highlight the extreme maximum and minimum values and all the different ways that the geometry can be welded utilizing four different welding configurations w_c. The aim was to minimize the number of passes; thus, the first weighting coefficient was selected to be 60%. Comparing the results from the maximum cost value relative to the minimum requires six more passes, the welding time is increased by 44.49% and filler wire is 34.24% higher. This result validates the benefits linked to the cost function concept, which decreases the actual costs of automated welding, through reduced welding time, material and passes deposited. It is noted that the extra filler material of a fixed volume groove can be assigned in the cap pass area, based on the previous layer height offset from the root face resulting in different cost results. Moreover, when the geometry under consideration increases in depth and groove angle, more instances can be built and investigated, exploiting the advantages of the cost function concept, and delivering crucial savings on large scale projects in terms of cost and time planning.
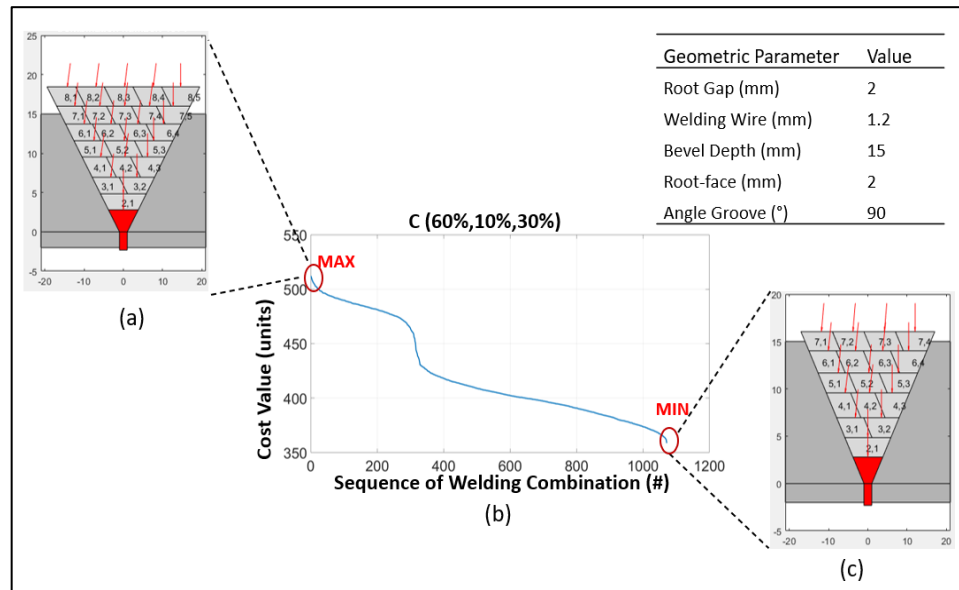
Figure 4.6. Highlighted cost function built from 1071 unique instances using 4 different welding configurations for 7 possible layers: (a) Solution from maximum cost value showing additional required six passes and increased welding time of 44.49%, (b) Cost function along the sequences of welding combinations, (c) Solution from minimum cost value showing a decrease of 34.24% in filler wire and six welding passes less than the maximum result

This process can be accelerated if instead of generating all the instances for every sequence of welding parameters, to reject every new incompatible instance when a new layer is added and results to higher cost value. However, the benefits of investigating the welding sequence from the minimum value of different cost functions, recommends the generation of all the possible instances for every row of array P. Therefore, the series of welding configurations that minimize at the most one of the three parameters (welding time, number of passes, filler material) can be found.

4.3.5.   Formalizing the Deposition of Additional Cap-Passes

The need to formalize the input of additional weld cap passes in the path layout model of [145] originates from initial welding trials, where the schematic of the proposed welding

solution did not match the expected result. The reasons behind this can be summarized as follows:

- According to the model of the welding torch pose and generated weld pass on [145], the shape of each bead (trapezium/parallelogram) is an approximation of the actual result and the space that will be allocated. However, as the molten weld pool solidifies, gravity and residual stress forces alter the approximated shapes in the cap layer to be more convex, circling the toes of the edges.

- Based on [145], all weld passes are deposited side to side, and the increased working angle of the torch on the first pass of the cap layer relative to the working angle of the root pass leads to overlap a part of the toes of the top surface. Additional passes with the same angle again overlap part of the previous cap passes, resulting in the formation of hollow spaces as can be seen in Figure 4.7 (a) and (b).

Therefore, the additional produced cost from the cap passes is incorporated to the cost function calculation in order the total minimum solution to be found.
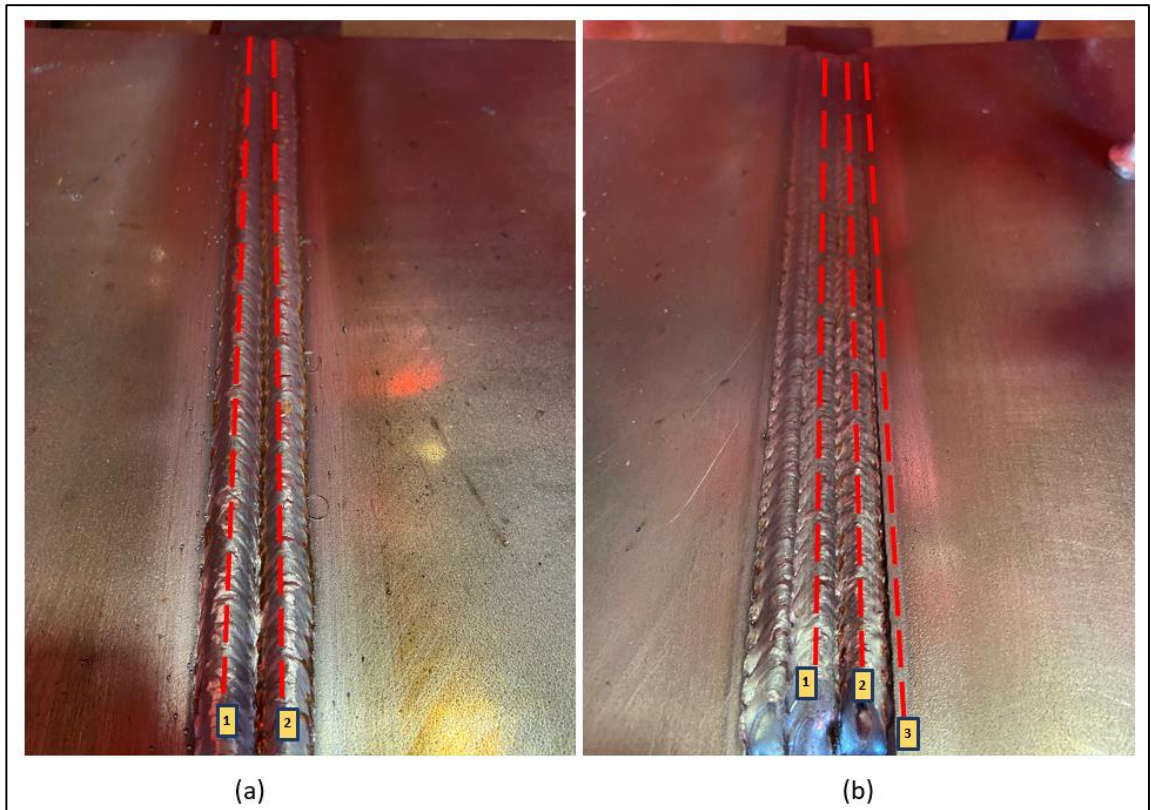
Figure 4.7. Highlighted formed concave spaces: (a) Between dotted lines 1 and 2 (b) Between dotted lines 1 and 2, 2 and 3

Formalizing these passes depends on the welding parameters of the previous passes in the cap layer. If the total number of weld beads deposited in the cap layer is denoted with letter m, p_m is the offset of the last pass from the middle of the seam and w_m is the weaving width then:

- When $m = 2$, only one additional cap pass is required. The pass is deposited in the middle of the V-groove (zero-offset from root gap) utilizing the same pose as the root pass with 10% less wire feed speed, based on experimental analysis, than what was used for the other passes at the same layer. The decreased wire feed speed results to less heat input in the last layer and consequently in lower stress

100

concentration. Moreover, the required weaving width was set to be 3 mm to achieve proper fusion with the side beads, based on experimental trials.

- For the case where $m > 2$ two additional cap passes are required. The first one is deposited between one pass before the last one and the last one with the position offset from the middle of the seam, is given by Equation (4.7).

$$p_{m+1} = \frac{(p_{m-2} + w_{m-2}) + (p_{m-1} - w_{m-1})}{2} \tag{4.7}$$

The second pass is deposited with an offset from the middle of the seam based on Equation (4.8).

$$p_{m+2} = p_{m-1} + w_{m-1} \tag{4.8}$$

As before the required wire feed speeds for both passes are 10% less than what is assigned in the other passes on the cap layer and the weaving width is 3 mm. Moreover, the angle of the welding torch for the second cap pass was set to be -5° relative to the root pass angle. Consequently, proper fusion is managed with the already deposited pass and the toes of the bevel.

The proposed additional cap passes in the welding system result can be seen schematically with the red dotted lines on the top layers in Figure 4.8. The selected welding parameters for both cases, were guided from the experimental trials and provided suitable fusion of the two toes of the bevel groove and a clean finish of the cap layer. Formalizing algorithmically the need for additional cap passes, allows the generalization of this process in varying V-groove geometries.
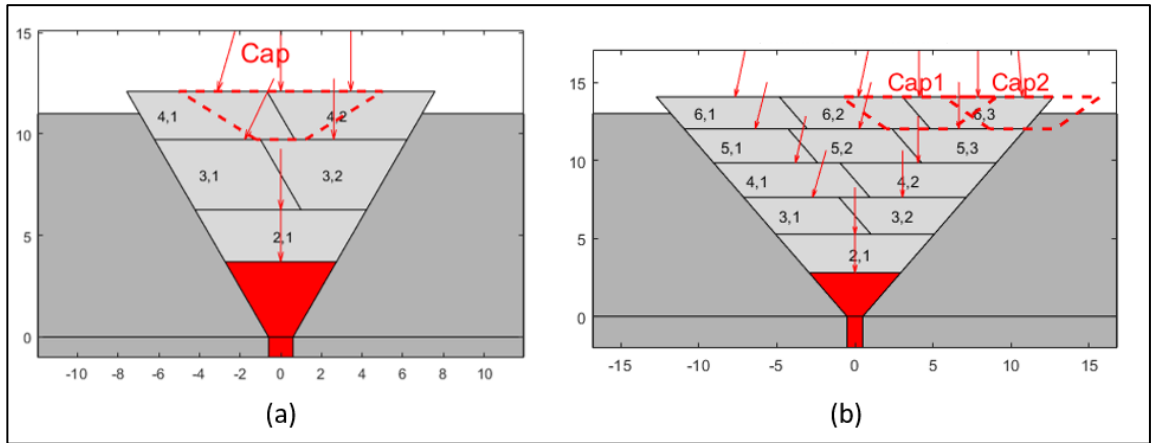
Figure 4.8. Additional cap passes added to the welding system solution to compensate between the model and actual welding result: (a) One more cap pass is required in the middle of the seam since the total deposited passes in the top layer were m=2, (b) Two additional cap passes are proposed when m>2 and the deposition position is formalized based on the previous existing passes in the same layer

4.4. Experimental Setup

A series of experiments were undertaken, utilizing the 6 DoF automated holistic robotic welding system introduced in Chapter 3 to prove the feasibility of the proposed welding system for multi-pass welding, aiming to automate the generation of the robotic motion path, welding parameters allocation and adaptation per layer based on the cost function concept.

4.4.1. Welding Parameters Configuration

To determine the deposition coefficient a_H, which is described in Section 4.3.1, welding passes with varying parameters were deposited and the cross-section area of each one was

measured using the laser scanner. A comparison of the cross-section area with the theoretically expected value from Equation (4.2) is shown in Figure 4.9.
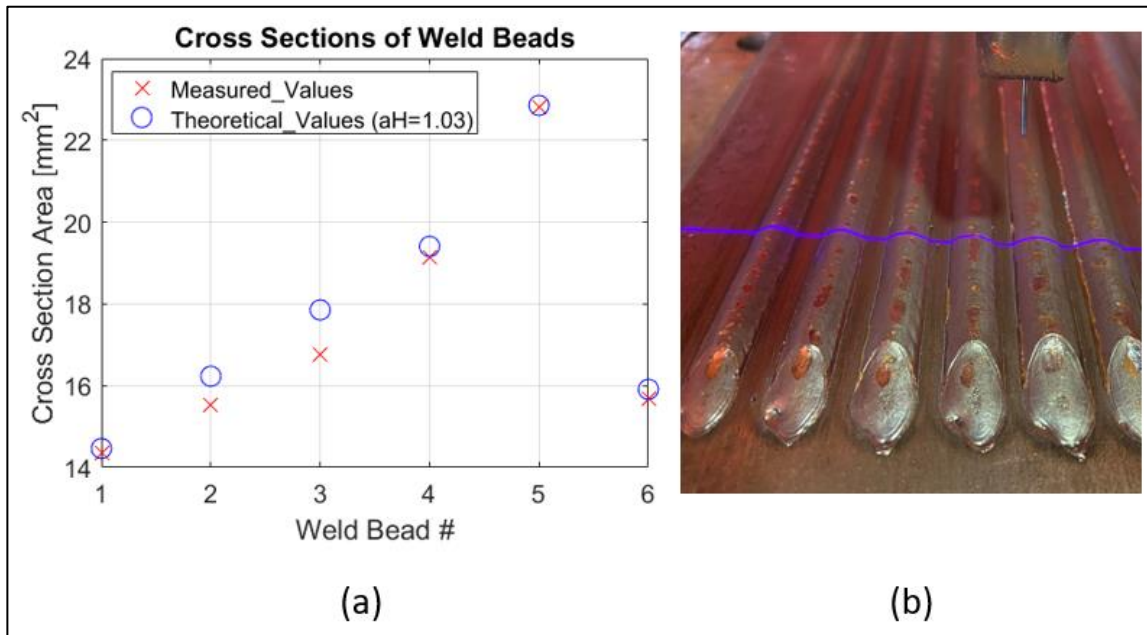
Figure 4.9. Highlighted cross section of welding beads with different welding parameters: (a) Measured values with laser scanner relative to theoretical values of Equation (4.2) (b) Deposited welding beads (front side-end of weld beads)

Obtaining the correct value of a_H is driven also from initial V-groove welding trials as can be seen in Section 4.4.3, where the proposed schematic solution of the welding joint did not match the volume of the actual welding result. Altering this parameter affects the schematic solution and the proposed number of passes as well. As a result, the constant a_H is found to be $a_H = 1.03$. Following this investigation, each of the welding configurations ($w_c = [v, u]$) selected for these experiments and used as input to the welding system, are stated in Table 4.3, and sorted in the descending order of their cross-section area. The selection of these welding configurations aligns with the industrial

partner's WPS for the welding joints provided in Table 4.4, as well with the purpose to have welding beads that form a window of varying cross-section area, where in that case covers 14.46 mm²-17.85 mm². As it is shown in Section 4.4.2, selecting pairs of welding configurations that form a fine window of cross-section areas can lead to a plethora of different sequences of welding parameters linked to the minimum solution of the cost function for varying V-groove geometries, as well for the same welding geometry and for different cost functions (Table 4.10).

*Table 4.3. Welding Parameters (**n**=4) along with theoretical, measured cross-section areas and recorded electrical parameters*

Welding Configuration	Robot Speed (mm/s)	Wire Feed Speed (mm/s)	Theoretical Cross Section (mm^2) *	Measured Cross Section (mm^2)	Current (A)	Voltage (Volts)
w_{c1}	5	76.63	17.85	16.77	144	21.9
w_{c2}	5	68.3	15.91	15.69	131	21.3
w_{c3}	5.5	76.63	16.23	15.52	144	21.9
w_{c4}	5.5	68.3	14.46	14.35	131	21.3

Investigating for example the number of welding pairs, if the number of current values increase by two then the wire feed speeds increase as well and selecting two additional robot speeds brings the total number of welding configurations to $n + 2 = 6$. Hence, Equation (4.6) storing the number of total permutations, produces the value $(n + 2)^k$ where the size of array P in Figure 4.5 increases to $(n + 2)^k \times k$ and as a result additional computational time is required to investigate and build all the different welding instances.

The weaving restriction enforced by parameter delta (δ), was found experimentally to be $\delta = 2$. This condition in weaving which reported in [145] is used in the algorithm

described in Section 4.3.2 which compensates the weaving width of the welding torch since the molten weld puddle can fuse with the edges of the groove without the tip of the wire to flush with them.

4.4.2.   Experimental Validation and Results

For the experimental verification trials, two different types of steel grade plates were machined to form three V-groove geometries, where the geometric characteristics recorded in Table 4.4 were extracted through the laser scanner. These configurations were selected based on commonly used marine and manufacturing configurations to highlight both the efficacy and flexibility of the proposed work. The welding reference path was set manually, providing the start and end points of the root pass.

Table 4.4. V-groove configurations and geometric characteristics of the joints

Characteristics	V-groove Geometry		
	S1	S2	S3
Structural Steel Grade	S-355	S-275	S-275
Root Gap (mm)	1.2	1	1
Welding Wire Diameter (mm)	1.2	1.2	1.2
Bevel Depth (mm)	12	13	13
Root-face (mm)	1	2	2
Groove Angle (°)	60	93	82
Root Height Offset (mm)	3.7	2.9	2.8
Length of Joint (mm)	300	300	300

Figure 4.10, 4.11 and 4.12 illustrate the selected cost function allocated for each one of the three samples along with the generated welding schedule of layers and passes. The red arrows represent the working angle of the welding torch for every weld pass, based on sequence path layout model developed in [145].
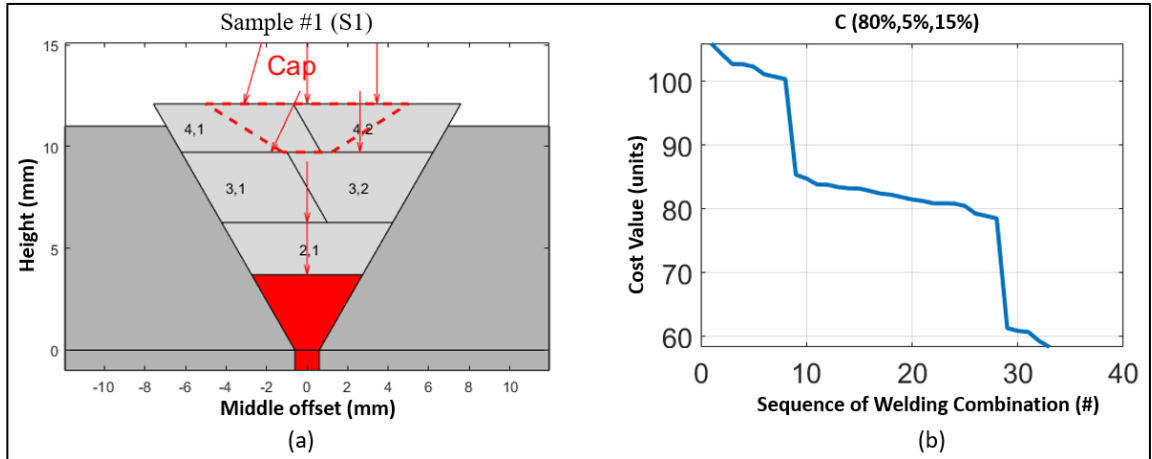
Figure 4.10. (a) Generated welding schedule for Sample #1 (S1) for the minimum cost value, (b) Values of allocated cost function across all the possible welding combinations for this V-groove geometry (Table 4.4-S1)
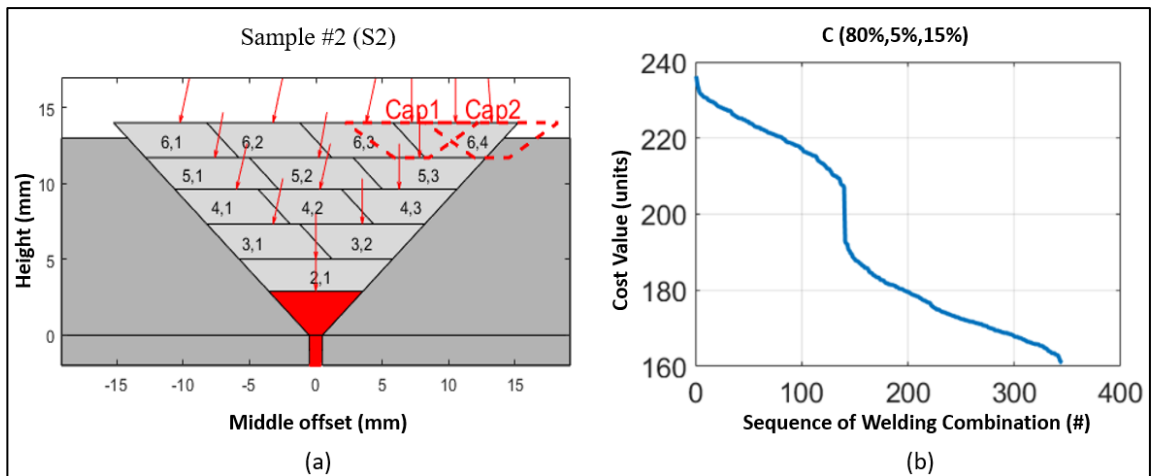
Figure 4.11. (a) Generated welding schedule for Sample #2 (S2) for the minimum cost value, (b) Values of allocated cost function across all the possible welding combinations for this V-groove geometry (Table 4.4-S2)

106
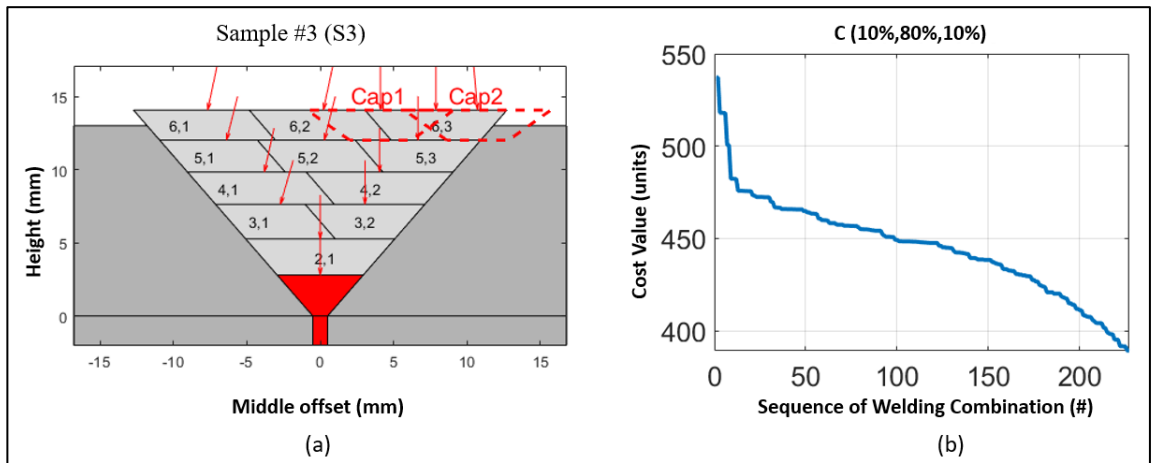
Figure 4.12. (a) Generated welding schedule for Sample #3 (S3) for the minimum cost value, (b) Values of allocated cost function across all the possible welding combinations for this V-groove geometry (Table 4.4-S3)

Figure 4.13, 4.14 and 4.15 illustrate a timelapse of the deposited welding passes for samples S1, S2 and S3 respectively, which validate the proposed welding solution in terms of adequately filling the whole groove with the generated welding passes resulting in a cap height above the top surface of average value 0.9 mm. The generated welding parameters produced from the welding system are stored in Table 4.5, 4.6 and 4.7.
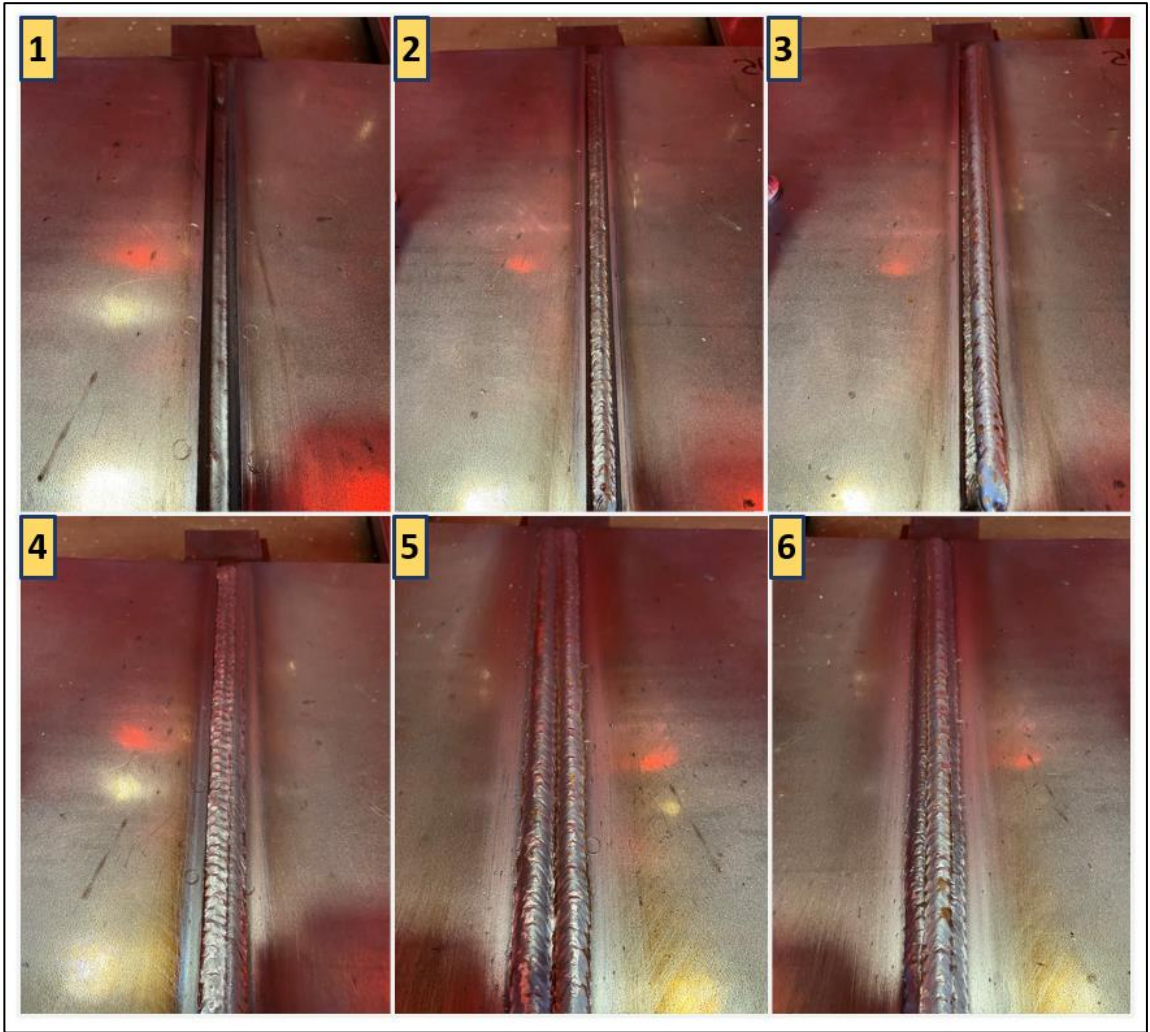
Figure 4.13. The generated welding sequence for the minimum value of cost function C(80%, 5%, 15%) resulted in 7 welding passes for sample S1
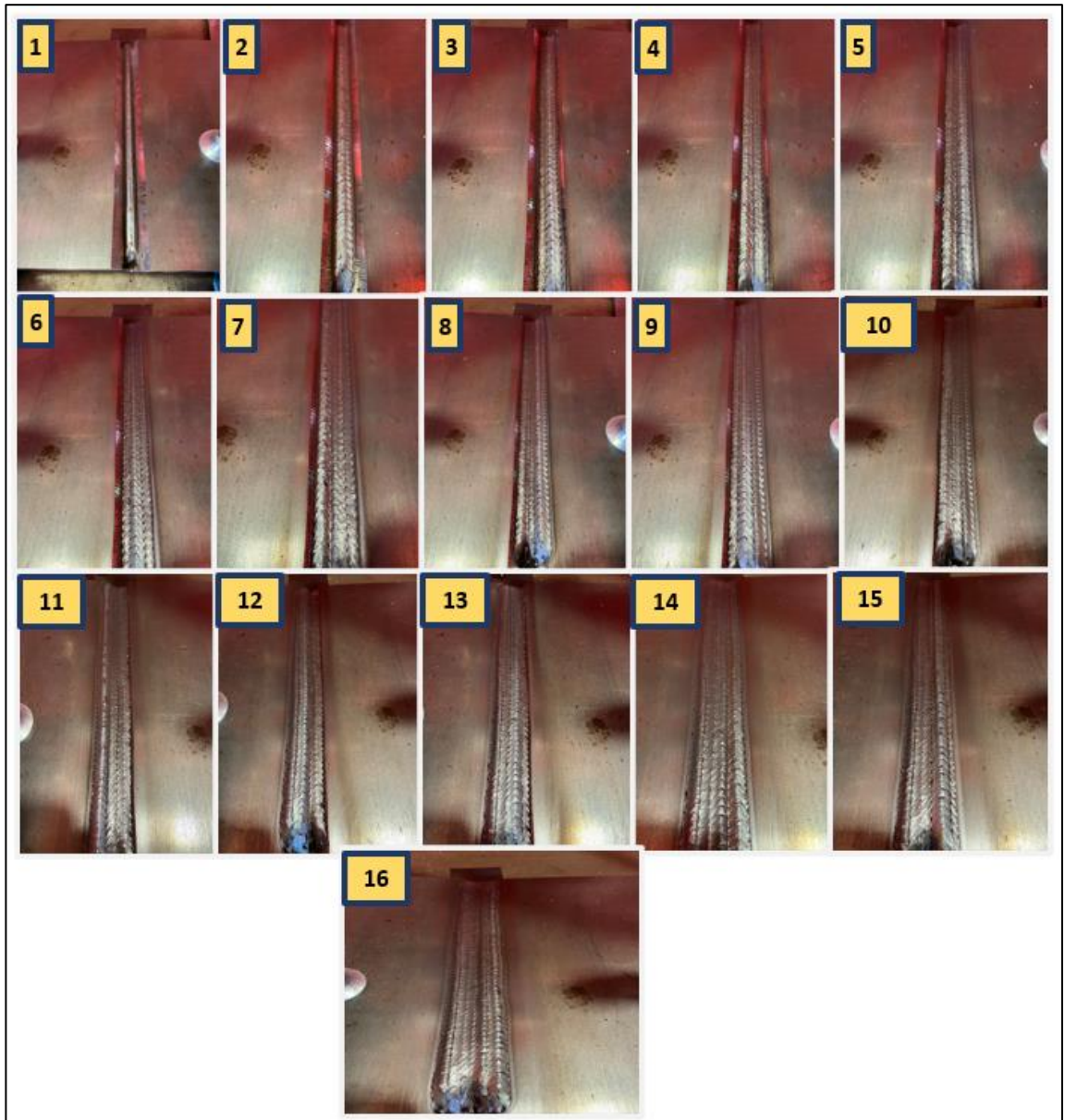
Figure 4.14. The generated welding sequence for the minimum value of cost function C(80%, 5%, 15%) resulted in 16 welding passes for sample S2
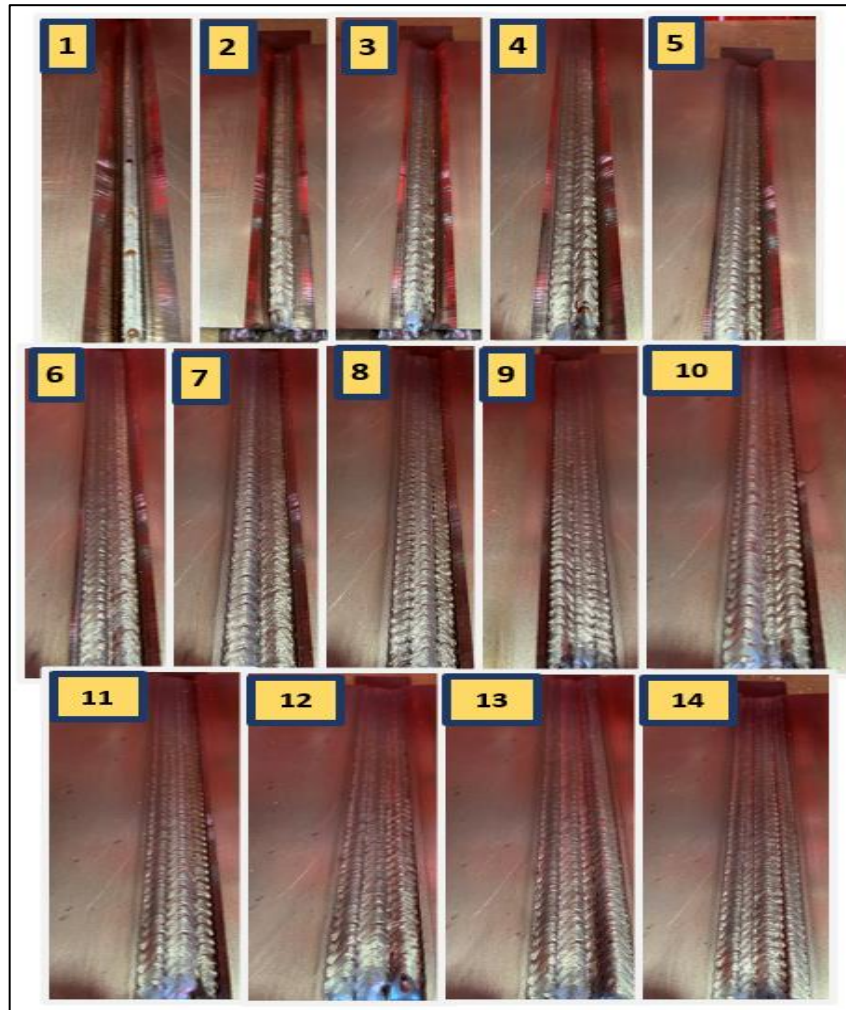
Figure 4.15. The generated welding sequence for the minimum value of cost function C(10%, 80%, 10%) resulted in 14 welding passes for sample S3

Table 4.5. S1 Generated welding parameters

Layer Number (#)	Pass Number (#)	Wire Feed Speed (mm/s)	Robot Speed (mm/s)	Offset-middle of the seam (mm)	Height from root-face (mm)	Angle of torch (°)	Weaving Width (mm)	Consumable Material (g)	Arc Welding Time (s)
1	1	60	4.50	0	3.70	0	0.73	32.93	66.66
2	1	83.30	5.50	0	6.26	0	2.21	37.40	54.54
3	1	76.63	5	-1.77	9.72	25.61	1.99	37.85	60
3	2	76.63	5	2.60	9.72	0	1.60	37.85	60
4	1	76.63	5.50	-3.10	12.09	16.02	2.30	34.41	54.54
4	2	76.63	5.50	3.44	12.09	0	2.13	34.41	54.54
4	3	68.96	5.50	0	12.09	0	3	30.97	54.54

Table 4.6. S2 generated welding parameters

Layer Number (#)	Pass Number (#)	Wire Feed Speed (mm/s)	Robot Speed (mm/s)	Offset-middle of the seam (mm)	Height from root-face (mm)	Angle of torch (°)	Weaving Width (mm)	Consumable Material (g)	Arc Welding Time (s)
1	1	55	5	0	2.90	0	1.55	27.17	60
2	1	93.30	5.50	0	5.01	0	3.78	41.90	54.54
3	1	76.60	5.50	-3.21	7.33	13.77	2.86	34.41	54.54
3	2	76.6	5.50	3.50	7.33	0	2.72	34.31	54.54
4	1	68.30	5.50	-5.98	9.63	14.77	2.50	30.67	54.54
4	2	68.30	5.50	0.30	9.63	14.77	2.50	30.67	54.54
4	3	68.30	5.50	6.29	9.63	0	2.357	30.67	54.54
5	1	76.63	5.50	-7.61	11.70	11.69	3.11	34.41	54.54
5	2	76.63	5.50	0.21	11.70	11.69	3.11	34.41	54.54
5	3	76.63	5.50	7.82	11.70	0	3.00	34.41	54.54
6	1	76.63	5.50	-10.25	14.01	13.72	2.86	34.41	54.54
6	2	76.63	5.50	-3.23	14.01	13.72	2.86	34.41	54.54
6	3	76.63	5.50	3.79	14.01	13.72	2.86	34.41	54.54
6	4	76.63	5.50	10.53	14.01	0	2.73	34.41	54.54
6	5	68.96	5.50	7.236	14.01	0	3	30.97	54.54
6	6	68.96	5.50	13.26	14.01	-5	3	30.97	54.54

Table 4.7. S3 generated welding parameters

Layer Number (#)	Pass Number (#)	Wire Feed Speed (mm/s)	Robot Speed (mm/s)	Offset-middle of the seam (mm)	Height from root-face (mm)	Angle of torch (°)	Weaving Width (mm)	Consumable Material (g)	Arc Welding Time (s)
1	1	55	5	0	2.8	0	0.93	27.17	60
2	1	93.30	5.50	0	4.26	0	3.07	41.9	54.54
3	1	68.30	5.50	-2.71	7.63	16.17	2.25	30.67	54.54
3	2	68.30	5.50	3.05	7.63	0	2.08	30.67	54.54
4	1	76.63	5	-3.80	9.84	12.42	3.12	37.85	60
4	2	76.63	5	4.04	9.84	0	3.00	37.85	60
5	1	68.30	5.50	-6.38	12.01	14.24	2.41	30.67	54.54
5	2	68.30	5.50	0.27	12.01	14.24	2.41	30.67	54.54
5	3	68.30	5.50	6.66	12.01	0	2.27	30.67	54.54
6	1	76.63	5.50	-7.67	14.06	11.99	2.94	34.41	54.54
6	2	76.63	5.50	0.21	14.06	11.99	2.94	34.41	54.54
6	3	76.63	5.50	7.88	14.06	0	2.83	34.41	54.54
6	4	68.96	5.50	4.10	14.06	0	3	30.97	54.54
6	5	68.96	5.50	10.72	14.06	-5	3	30.97	54.54

4.4.3.   Welding Failures

Initial investigation for determining the values of the deposition coefficient a_H and weaving restriction parameter (δ) through welding trials and different V-groove geometric configurations resulted in lack of fusion between beads and mismatch between proposed welding schedule and actual welding result.

Table 4.8 stores two of those welding configurations used to deploy initial trials, while Figure 4.16 and Figure 4.17 depict the welding failure results.

Table 4.8. V-groove configuration and geometric characteristics of the joints

	Failure 1	**Failure 2**
Structural Steel Grade	S-275	S-275
Root Gap (mm)	1.0	1.2
Welding Wire Diameter (mm)	1.2	1.2
Bevel Depth (mm)	13.9	10.11
Root-face (mm)	1.1	4.89
Groove Angle (°)	92	93
Root Height Offset (mm)	3.0	2.9
Length of Joint (mm)	300.0	300.0
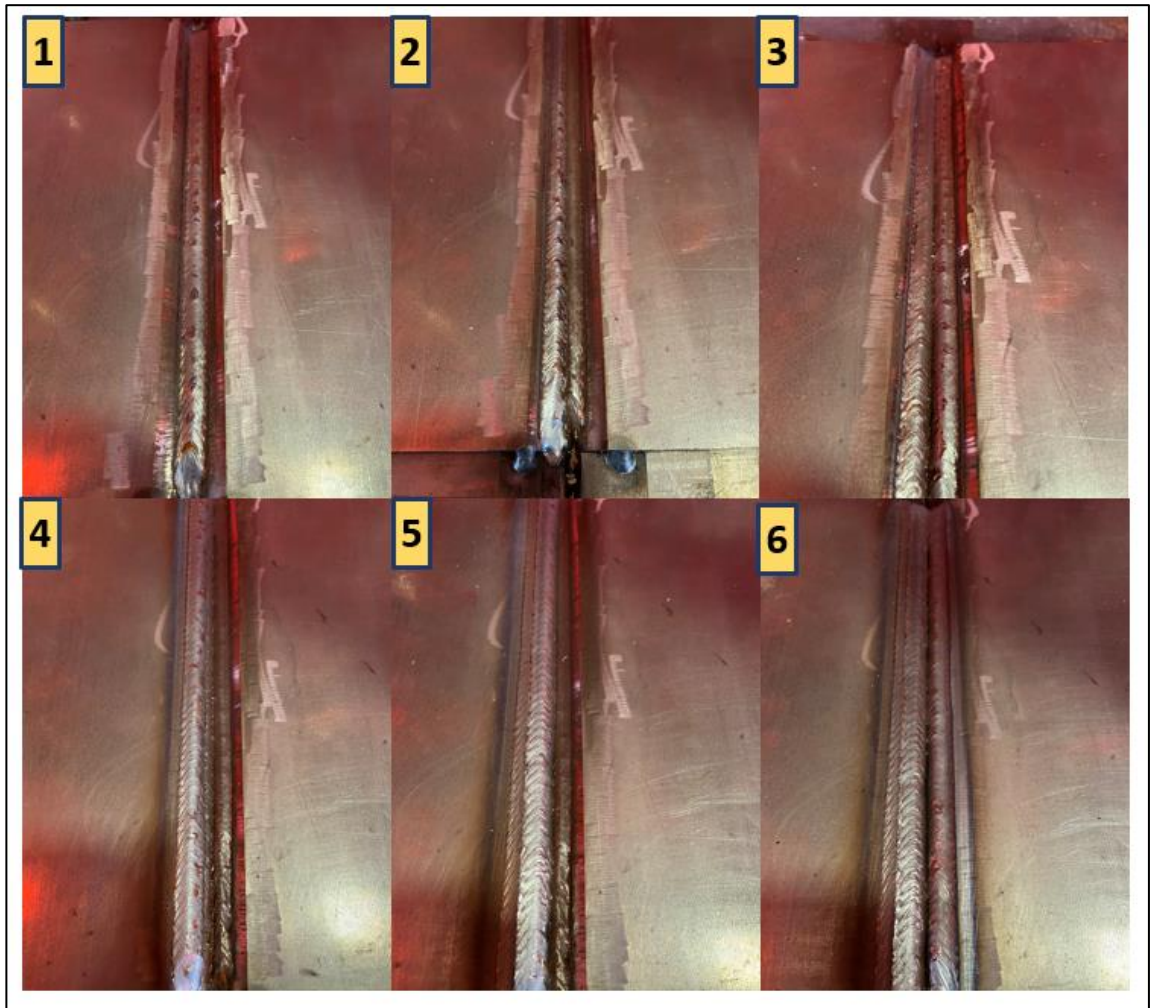
Figure 4.16. Failure 1 timelapse of deposited passes. Choosing $a_H = 0.98$ and weaving restriction parameter δ=2.8, resulted in excessive volumetric filling of the groove and lack of fusion due to increased value of δ.

More specifically for Failure 1, the deposition coefficient was selected to be $a_H = 0.98$ which resulted in a volumetric overload of the groove due to the increased theoretical cross section area of the beads. This can be seen from frame number six where the fourth welding layer out of the five is depicted and already the top surface of the groove is reached. In addition, the lack of fusion between the deposited beads was the result of the

increased value of the weaving restriction parameter δ=2.8 which resulted to decreased weaving width.
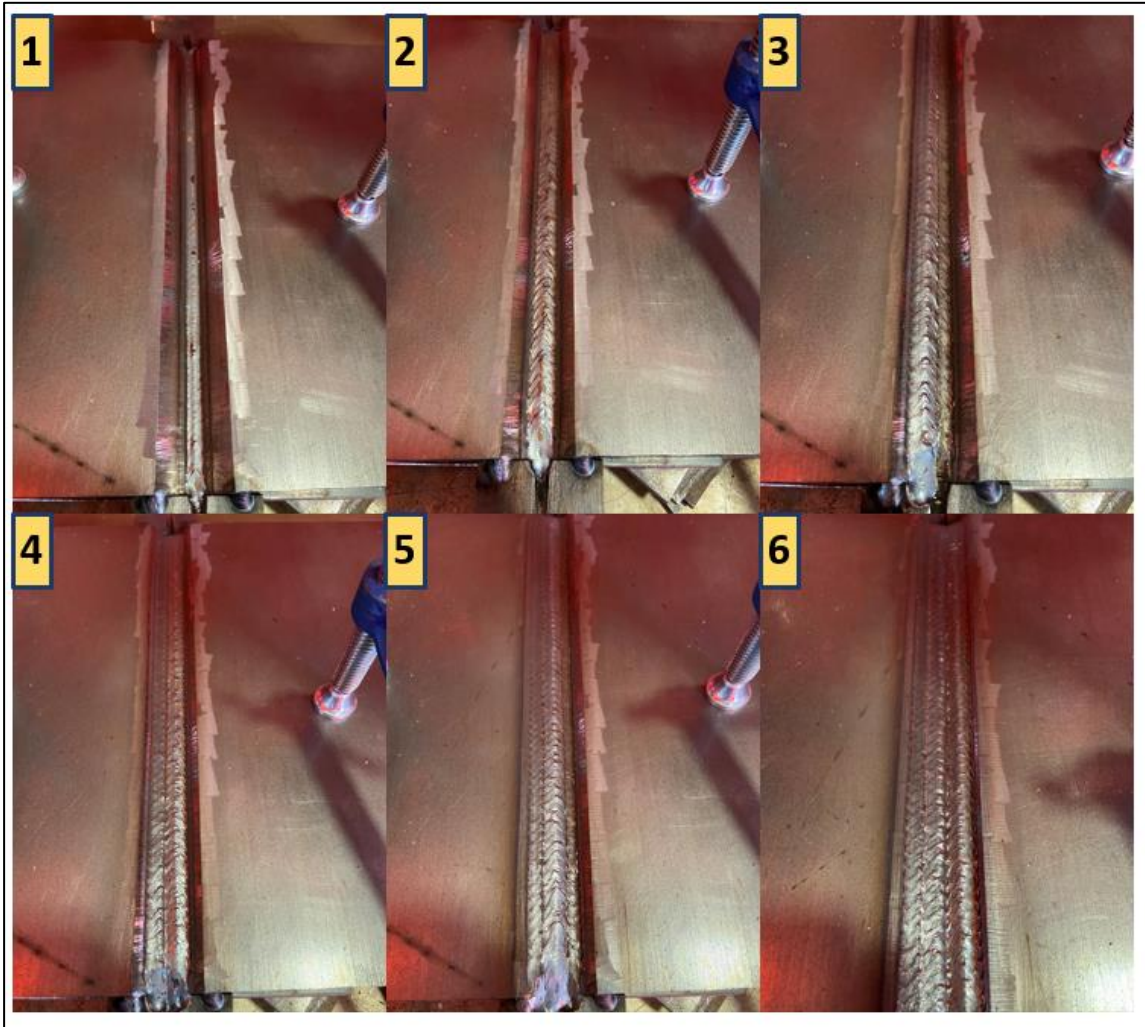
Figure 4.17. Failure 2 timelapse of deposited passes. Choosing $a_H = 1.08$ and weaving restriction parameter δ=2.5, resulted in lack of volumetric filling of the groove and lack of sidewall fusion due to the value of δ.

Regarding Failure 2, the deposition coefficient was set to be $a_H = 1.08$ resulting in underfilling the V-groove as can be seen from the timelapse in Figure 4.17. Moreover, weaving restriction parameter δ=2.5 has as a result lack of sidewall fusion.

4.4.4.   Ultrasound Inspection for Defects

For assessing the quality of the welded joints, Phased Array Ultrasonic Testing (PAUT), was employed to inspect the produced weldments [149]. The allocation of welding parameters through the cost-function concept establishes the generation of the welding sequence along the welding layers and does not optimize the quality of the weldments. However, it was mandatory the generated welding sequence to comply with the accompanying WPS to achieve an acceptable weldment. The developed welding system and the integrated technology that described in Chapter 3 was responsible to deliver repeatable high-integrity weldments.

An ultrasonic probe of 5 MHz with a linear array of 64 elements of 0.5 mm pitch was used to perform sectorial scans. A wedge of 37.6° was attached to the array and the focal laws were generated to form an S-scan covering a range of 35°-75°. Gain calibration was performed according to BS EN ISO 17640, and the reflections from defects were compared with the reference response signal. The calibration is depicted in Figure 4.18 where two side-drilled holes of ⌀ 2.0 mm diameter in a 15.0 mm thick welded section are inspected with the phased array probe. The gain was set to 50 dB, where the signal amplitude indicates 100% of the scale bar.

Following the gain calibration, each produced welded joint was inspected at room temperature along the length of the welding axis. In some positions, lack of root penetration was identified and is reported in Figure 4.19. No indication of lack of fusion on sidewalls or inter-pass lack of fusion was detected across all samples, which can frequently occur in welded joints during manufacturing [150].
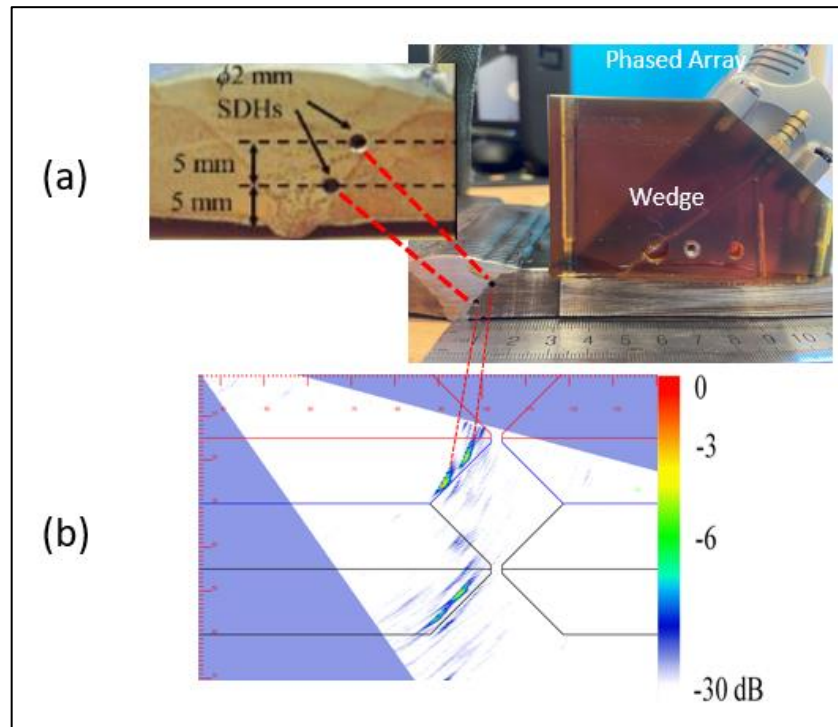
Figure 4.18. Gain calibration using two side-drilled holes of ⌀ 2 mm for PAUT inspection

Lack of root penetration may have been caused by misaligned fitting of the parent metal plates during joint setup and uneven height of root face caused by bevelling of the weld grooves. As mentioned previously, the welding parameters for root and hot pass were instructed from the operator and are not included in the automation of the proposed welding system, which is discussed in this chapter.
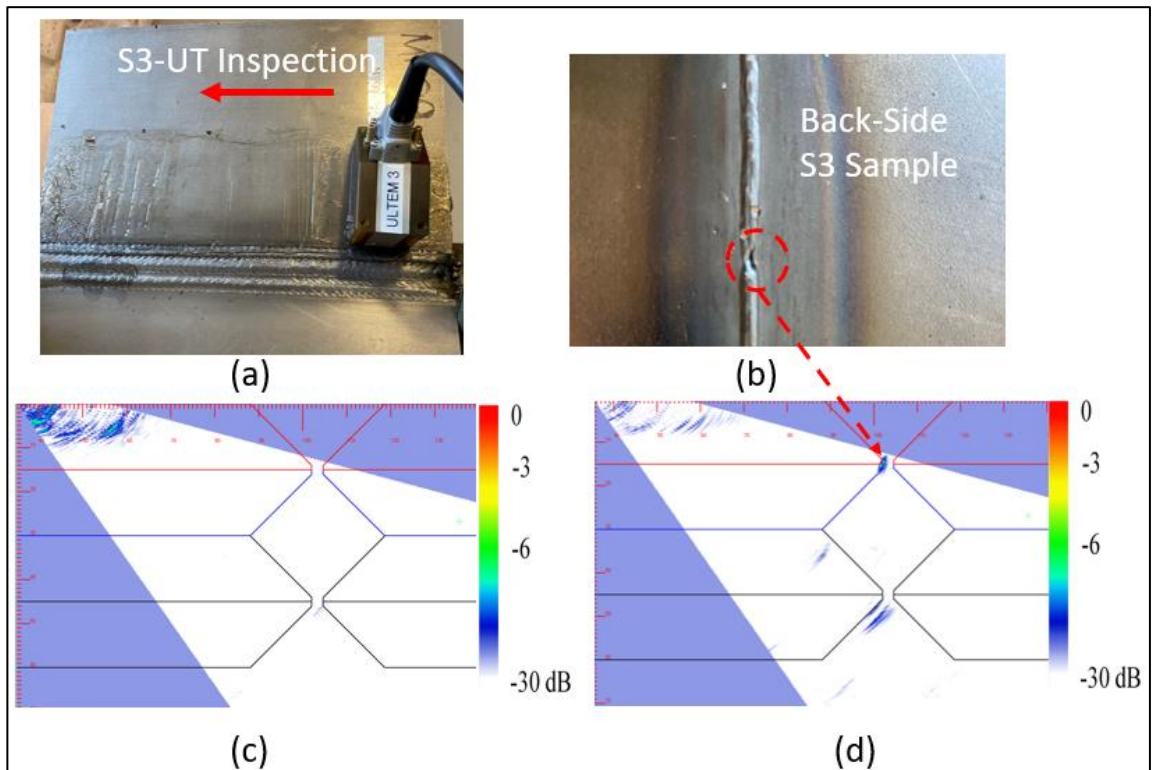
Figure 4.19. Phased array inspection and indication of lack of root penetration: (a)Sample S3 showing the direction of inspection, (b)Back-side of sample S3 where lack of root penetration exist, indicated by the red circle, (c) Sector scan 35°-75°: where no defects are found, (d) Sector scan 35°-75°: reflection caused from lack of root penetration

4.4.5. Distortion on the Weldments

Distortion was observed along the vertical direction of welding as shown in Figure 4.20. The inter-pass temperature was held at 70°C, and clamping was consistent across all samples. Distortion was more severe in samples S2 and S3, where their structural steel grade is lower than S1 and the thickness of the plates was 3 mm more. Also, on all samples, metal straps were tack welded on both sides to prevent excessive distortion.

Distortion is attributed in the order which the generated welding passes were deposited. The deposition of the welding beads took place side to side, always starting from the left

of the groove (seen from the front-side of Figure 4.20) generating increased heat on the left parent plate introducing distortion.
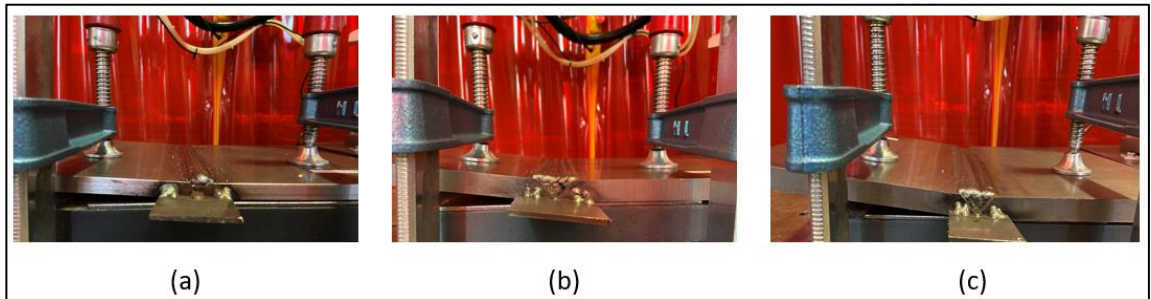
Figure 4.20. Distortion observed on welded samples: (a) Sample S1-Material S-375 with seven welding passes, (b) Sample S2-Material S-275 with 16 welding passes, (c) Sample S3-Material S-275 with 14 welding passes

Moreover, weaving is required on each welding pass, except the root pass, which increases the heat input as the welding torch spends more time inside the groove.

4.5. Discussion

The following sections discuss the results of the welding trials based on the allocated cost function and the generated welding schedule. Also, the state of the art is compared relative to the proposed methodology of multi-pass welding system proposed in this thesis.

4.5.1.   Generated Welding Results and Cost Functions
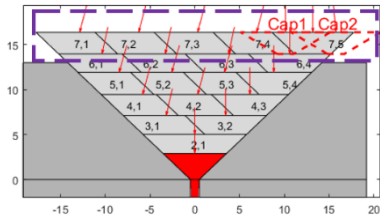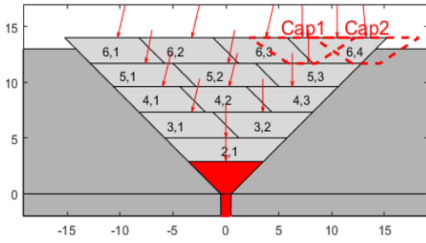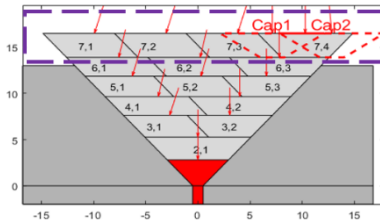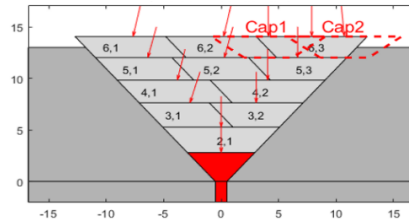
Three manufactured samples were produced by the proposed welding system with the cost function concept described in Section 4.3.4, and presented in this work with welding parameters recorded in Table 4.5, 4.6 and 4.7. The samples were welded using the generated welding parameters and visual inspection showed no undercuts or lack of fusion

between adjacent passes. This was also validated from the PAUT inspection presented in Section 4.4.4.

The welding parameters utilized to weld each sample were extracted from the optimum generated instance of the V-groove linked to the minimum value of the assigned cost function. Regarding sample S2, where cost function C(80%, 5%, 15%) was assigned, comparing maximum and minimum values, the welding time was decreased by 32.9% and the amount of filler wire by 26.18%. Similar savings were noticed regarding the cost function of sample S3, C(10%, 80%, 10%), where the reduction in welding time and in the amount of filler wire was 28.3% and 27.38% respectively. These reductions are reported in Table 4.9 for both samples again representing the difference between maximum and minimum values of each cost function. In addition, from the schematic comparison, the additional amount of filler wire for both samples (purple dotted box), linked to the maximum solution is assigned to the cap pass area, which is defined as the less efficient solution for the allocated cost function.

Table 4.9. Comparison between maximum and minimum values of cost function C(80%,5%,15%) and C(10%,80%,10%) respectively for samples S2 and S3 regarding the amount of filler wire and arc time

Sample S2	MAX	MIN	Decrease (%)
Amount of filler material (g)	628.18	463.68	26.18
Arc time (s)	1259.1	843.63	32.9
Schematic Solution			

Sample S3	MAX	MIN	Decrease (%)
Amount of filler material (g)	542.97	394.26	27.38
Arc time (s)	1011.8	725.45	28.30
Schematic Solution			

Samples S1 and S2 utilize the same form of the cost function to reflect the difference on the amount of possible unique generated sequences of welding parameters and the increase in the values that the function receives as the weld groove geometry changes in depth, groove angle and gap offset. As it was expected, sample S2 due to thicker material than S1, required two more welding layers and nine welding passes than sample S1. The

selection of weighting coefficients for the cost function depends solely on the operator's choice, and different cost functions can be compared only in the degree that the result is driven by the operator's choice of the parameter to minimize at most.

This can be understood better in sample S3 with cost function $C(10\%, 80\%, 10\%)$, which highlights the aim to reduce at most the filler consumable material relative to the other two parameters. Comparing the utilized cost function relative to $C(80\%, 5\%, 15\%)$ for the same sample, the amount of filler wire is reduced by 4.34 grams, but the additional arc welding time is increased by 9.91 seconds since the w_3 is reduced by 5%. The expected outcome (which is illustrated in Table 4.10), is validated from the reflection of the weighting coefficients in the generated sequence of welding parameters in layers 4 and 5 if the cost function $C(80\%, 5\%, 15\%)$ was allocated instead of $C(10\%, 80\%, 10\%)$.

*Table 4.10. Different generated welding parameters in layers 4 and 5 for sample S3 using cost function **C(80%,5%,15%)** instead of **C(10%,80%,10%)***

Layer Number (#)	Pass Number (#)	Wire Feed Speed (mm/s)	Robot Speed (mm/s)	Consumable Material (g)	Arc Welding Time (s)
4	1	76.63	**5/5.50**	**37.85/34.41**	**60/54.54**
4	2	76.63	**5/5.50**	**37.85/34.41**	**60/54.54**
5	1	**68.3/76.63**	5.50	**30.67/34.41**	54.54
5	2	**68.3/76.63**	5.50	**30.67/34.41**	54.54
5	3	**68.3/76.63**	5.50	**30.67/34.41**	54.54

Moreover, large variations in the results of different cost functions for the same geometry can be noticed when the selected welding parameters w_c (stored in vector $\widetilde{W}$) as these result in a large variation of weld cross-section area. However, selecting beads with excessive large cross-section area can decrease the total arc welding time, whereas the

total heat input is increased with higher probability to damage the internal structure of the welded material. So, the algorithm described in Section 4.3.2, which is utilized in every new layer, to determine the number of welding passes has the advantage to adjust the initial welding parameters and adapt in that way to varying V-groove geometries. The three presented manufactured samples did not require this utility, since geometries with groove angles above 95° tend to require this logic as more passes stack together to reduce the weaving width but conversely the height of the layer increases above the restriction of 5 mm.

To enhance the understanding of the adaptation ability of the developed system an example is provided. Considering the V-groove geometry with characteristics as recorded in Table 4.11, using the welding parameters reported in Table 4.3 and cost function $C(80\%,5\%,15\%)$ it was found that the initial number of layers that can fit according to Section 4.3.4.1 equals to six. Following the process in Section 4.3.4.2, an investigation for permutations within iterations is performed for seven layers and the total number of permutations based on Equation (4.6) equals 16,384. It was found that violations on the height and weaving width took place for layers 3,4,5 and 6 and the logic described in Section 4.3.3 to adapt the given welding parameters was utilized 22,464 times resulting in total additional time of 0.1135 sec. Moreover, the average time spent in this logic when a violation occurred was $5.0537 \cdot 10^{-6}$ sec and the welding configuration $w_c = [5,76.63]$ had to change to [5.1,73.29] and in other instances to [5.15,71.62], thus two or in other cases, three iterations of this logic for 22,464 times contributed to the additional

computation time. The reported execution times are extracted from a workstation with an Intel Core i7 @ 2.60 GHz, 16.0 Gb of RAM, Windows 10x64 bit architecture.

Table 4.11. V-groove geometry where violation on height and weaving width occurred in layers 3,4,5 and 6

Geometric Parameter	Value
Root Gap (mm)	3
Welding Wire (mm)	1.2
Bevel Depth (mm)	15
Root-face (mm)	1
Groove Angle (°)	120
Root Offset (mm)	2.5

4.5.2.   Performance Assessment against the State-Of-The-Art

Based on the available relevant works, reported in Table 4.1, an experimental simulation comparison, regarding the performance between the state-of-the art and the proposed system is performed.

In [145] and [146] the same groove geometry is used, where in the latter the wire feed speed used for every welding bead was not reported. This does not allow the calculation of the amount of filler material used. To compare with [145], the same restrictions on the size of the weld bead, weaving width and welding parameters were utilized relative to this method and the cost function C(10%,10%,80%) was assigned to reduce the arc welding time. To have a common base of comparison, the length of the joint was normalized to 300 mm and the same root pass was used. The results are depicted in Table 4.12.

123

Following the restrictions on the height and weaving width for every welding layer that exist in [145], one more additional layer and cap pass were added. As explained in Figure 4.2, this occurs from the investigation for the numbers of layers and passes per layer and the need to find the optimum sequence of welding configurations, by utilizing the same welding parameters as in [145]. As a result, by permutating the welding parameters, forming the required layers and investigating all the possible solutions delivers direct savings, compared to prompting the user to decide on the number of layers and the welding parameters per layer.

Table 4.12. Quantitative comparison of the proposed welding system relative to the work reported in [145]

	Layers	Number of Passes	Material (g)	Arc Time (s)
H. Zhang [145]	5	8	1400.49	1815.06
This body of work	6	9	1047.32	1551.33
Difference	+1	+1	-25.22 %	-14.53%

As in the work reported in [146] the wire feed speed for every pass is omitted and the same groove geometry is used as in [145], the results from the above table are used to compare with the arc time required to weld the whole geometry. It can be seen in Table 4.13, that the amount of welding passes deposited was 51, thus this method was not efficient to achieve a better arc time than [145] and the proposed work herein.

Table 4.13. Quantitative comparison of the proposed welding system relative to the work reported in [146]

	Layers	Number of Passes	Material (g)	Arc Time (s)
S.J. Yan et al [146]	10	51	N/A	3657.45
This body of work	6	9	1047.32	1551.33
Difference	-4	-42	N/A	-57.58%

The proposed system is also compared to [144] where a much smaller groove geometry with an angle of 25 ° is utilized than the previous works. The welding parameters for the root-pass from [144] were used. For the filling passes the welding parameters stated in Table 4.3 were assigned to the vector $\widetilde{W}$, since in [144] the same welding pass is used for all the passes in the different layers. The cost function C(10%,10%,80%) was utilized and the generated results of the welding system are compared in Table 4.14.

Table 4.14. Quantitative comparison of the proposed welding system relative to the work reported in [144]

	Layers	Number of Passes	Material (g)	Arc Time (s)
T.-Y.Huang et al. [144]	5	7	237.19	432.17
This body of work	6	9	229.69	274.19
Difference	+1	+2	-3.16%	-13.42%

Regarding [28] and [143], which use the same experimental verification, there are not available information regarding the material and arc time spent as well as welding

parameters allocated in order to validate the geometric characteristics of the utilized V-groove geometry.

4.6. Conclusion

In this Chapter, an algorithmic system for automated off-line multi-pass V-groove weld path planning and sequencing was developed and validated. It can generate robotic welding paths per pass and welding parameters for varying single-sided V-groove geometries per welding layer, based on the operator's choice to minimize a cost function defined as the weighting combination of number of welding passes, arc time and filler wire consumption.

The generation of welding passes per layer is driven from the algorithm presented in Sections 4.3.2 and 4.3.3, which populates the number of welding beads through the imposed restrictions on maximum weaving width and height of every welding pass. The developed work builds on the algorithmic work developed in [145] where the user is prompted to enter the total number of layers, number of passes and welding parameters. The adaptability of the welding parameters accomplishes the generation of welding passes planning irrespective of the geometric characteristics of the V-groove geometry. As a result, the robotic weld path planning process is accelerated without the need to re-program and teach the path points in space for the welding torch to follow.

The integrated cost function concept introduces the flexibility for the automation of different welding parameters per layer as it happens in manual welding. All the alternative ways that a V-groove geometry can be welded, based on the stored welding configurations

on vector $\widetilde{W}$ are investigated, resulting in comparisons and savings between different approaches, which can be prescribed by specifying a preferred operation performance metric. In this way, planning of resources can be perceived, estimating the overall welding procedure, and instantly deploying robotic welding between different V-groove joints. In practice, the developed system can potentially reduce direct robotic welding costs by minimizing the combination of the number of passes, arc time and filler consumable material through the assigned cost function. As an example, in the welding trial of sample S2, the arc time and amount of filler wire were found to be 32.9% and 26.18% lower respectively than the worst-case available welding parameter combination. In this proposed approach, since an operator does not decide the welding parameters, the cost function always satisfies the optimum result. As a result, a decrease of direct costs from the worst feasible automated way to weld the joint is achieved. Furthermore, indirect costs associated with freeing up welders for other tasks and reduced overwork from induced defects can further decrease manufacturing costs.

Experimental results validate the welding system utilizing different V-groove geometries for two types of steel grade. The proposed generated solution for each joint is examined under the actual welding result. Based on the proposed sequence of welding parameters which minimized the allocated cost function along with the respective robotic welding path, fusion of the beads with parent metal is achieved, proving the feasibility of each solution. The need for additional cap passes is reported and formalized to conclude the automated multi-pass robotic welding system. Moreover, the feasibility of the proposed work is enhanced when the structural integrity of the weldments is assessed using PAUT

inspection. Lack of root penetration was reported, which may have been caused by uneven root face of the metal plates from the bevelling of the groove sides and misalignment during fitting. Other defects were not identified, demonstrating an excellent overall fusion of the parent metals under the deposited weld passes.

In summary, this Chapter introduces and presents a new automated weld parameter and pass deposition sequencing strategy, which builds on the current state of the art, that enables automatic offline planning of multi-pass welding for single-sided V-groove geometries, through minimization of a user defined novel cost-function, resulting in clear commercial and technical benefits.

Chapter 5

Towards Flexible and Automated Robotic Multi-Pass Arc Welding

5.1. Introduction

Staying competitive in the global HVM sectors, including, but not limited to marine and nuclear remains a significant challenge. As product complexity and volumes rise, automated welding offers a potential solution to meet some of these demands [20,151,152]. However, the full automation of multi-pass arc welding still faces challenges due to difficulties related to current tedious and semi-automatic robotic path generation methods and the ease of adaption of the welding process to new (V-groove) geometries.

In this Chapter, the developed sensory-driven approach for automated robotic multi-pass arc welding is presented, which provides a means to interact with the environment, increase efficiency and adapt to changes without requiring manual re-programming of the robot path planning motion when the welding configuration or the environment changes. Moreover, the integration of the developed multi-pass welding system for single-sided V-groove geometries, presented in Chapter 4 completes the generation of an automated

robotic multi-pass welding system, able to locate the welding specimen in the scene and deploy multi-pass arc welding without human intervention.

More specifically, a series of novel algorithmic processes are developed, building on the state of the art, enabling automated multi-pass robotic arc welding for an unstructured environment. These include:

1. Adaption of the pose of the welding torch to the pre-welded joint
2. User-initiated, autonomous workpiece localization of the pre-welded joint

Benefits arising from an automated strategy to adapt the pose of the torch for a pre-welded joint, utilizing a sensor-guided approach, include i) maximum accessibility, ii) heat concentration and coverage for all three degrees of orientation in (cartesian space) as well as iii) the accurate extraction of geometry characteristics and key points of the weldment for on-the-fly welding path generation. The localization of the specimen in the scene is achieved through the combination of a common fiducial Quick Response (QR) code tag and hand-eye calibration, avoiding the need for feature matching with a CAD design, intensive computational complexity in terms of image analysis and the existence of a database with possible discrete poses. Hence, these contributions along with the deployment of kinematics through the described external real-time position control strategy (Chapter 3), raise the level of flexibility to weld different V-grooves in an unstructured environment, maximizing the production cycle by minimizing human input and the need to reprogram the robotic motion.

5.2. Vision Sensing Approaches in Workpiece Localization

The ratio of set-up time of weldments over production time can account for more than 95% [153]. This adds to the delay for reprogramming and outweighs the automated production efficiency, decreasing the potential for automation in low volume production. The current prevalent method for workpiece localization used in welding applications is feature matching [154,155], accomplished by the use of monocular or 3D sensors, mounted on a robot end-effector or in a static fixture within the welding cell to extract point cloud data of the workpiece [156]. Assuming an approximate pose of the workpiece, the extracted features are aligned with the reference CAD model, usually with a local minimization algorithm, such as Iterative Closest Point (ICP) [153,157,158] to compensate for small deviations or correct offline programmed path. This approach requires the existence of a CAD model, which is not efficient in terms of high product variance components. Moreover, the knowledge of an initial guess of the workpiece's pose and the need to fix the position of the 3D sensor within the cell constrains the potential of such approaches in structured environment conditions, i.e. those that exist on a production floor.

As a result, in welding applications, a global localization approach is absent compared to other automated production systems, such pick and place [156], where widely applied techniques are adopted such as clustering pose candidates [159,160] and voting schemes [161,162]. However, the accuracy of these methods depends on the existence of associated databases containing discrete reference poses of the workpieces, which is not feasible for an unstructured welding environment.

Table 5.1 depicts the current state-of-the-art regarding automated workpiece localization linked to automated path planning approaches along with their limitations.

Table 5.1. Relevant works in automated robotic workpiece localization

Relevant Works	No need for CAD design	No need for an Initial pose guess	No need for a database of discrete poses	Not a Computative Intensive Image Analysis *
Mitchell Dinham et al. [78]	✓	✓	✓	✗
MARWIN [117]	✗	✓	✓	✗
HEPHAESTOS I & II [118]	✓	✓	✓	✗
K.T. Gunnarsson [154]	✗	✓	✓	✓
Xiong et al [155]	✗	✓	✓	✓
M. Rajaraman et al. [153]	✗	✗	✓	✓
Cheng-Hei Wu et al. [52]	✗	✓	✗	✓
L. Yang et al. [64]	✗	✓	✓	✗
This body of work	✓	✓	✓	✓

* Intensive image analysis refers to image segmentation, applying window ROI, edge detection, 3D reconstruction

5.3. Methodology

5.3.1. Fiducial Marker and Estimation of eHw

A robust workpiece localization approach can be developed using a QR code (Figure 5.1), since its use as a fiducial marker to provide the detection and the pose of an object has been proved a resilient and flexible solution in a variety of robotic applications. Object manipulation tasks and autonomous driving of mobile robots [163,164] utilize QR codes

to increase the accuracy and robustness of localization, as can be a source of recognizable distinctive features with embedded fault detection [165]. Within the work of this thesis, the use of the QR code is utilized as a user-initiated method to identify the pose of a welding joint in the scene among the existing, to be welded, sequencing in that way welding jobs to the robotic welding system. Distinctive image features are extracted from the QR code which overcomes the dependence on the characteristics of the actual weld joint geometry, which are usually uniquely affected by the background environment or existing fixtures and clamping.

The estimation of eHw as discussed in Section 2.2.2.2 can be treated as a perspective-n-point problem which can be solved using the Perspective-three-Point (P3P) algorithm through OpenCV [166]. Inputs are the image points from the four corners of the marker which are captured through LabVIEW Vision Acquisition Software Library. Results are averaged over five consecutive frames, the corresponding word points of these corners, (which are provided as constants since the marker is of known size) and the camera parameters. The internal matrix and the distortion coefficients found from the camera calibration are then used to undistort each captured frame.

Figure 5.1. QR code which is used as a fiducial marker

To relate the QR code with the pose of the specimen, the following convention described in Figure 5.2 is followed, where one side of the square fiducial marker is placed by a human in parallel with the main axis of welding.
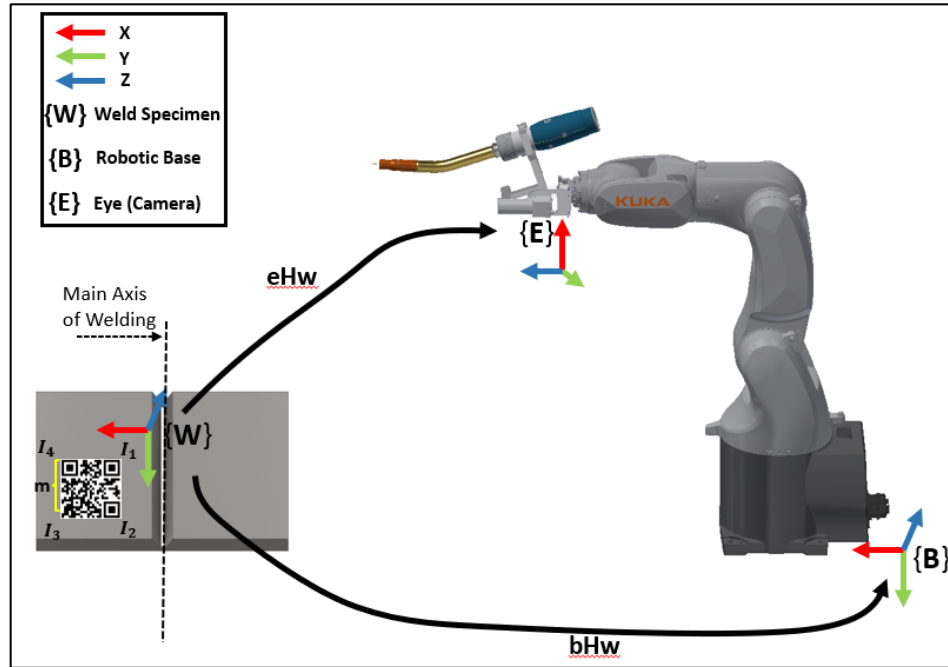
Figure 5.2. A fiducial QR code marker was placed in the weld joint to relate the pose of the welding specimen relative to the robot base

For a QR code with edge size equal to m and identified corners in image plane {I} of sequence I_1-I_2-I_3-I_4, the corresponding world points W_1-W_2-W_3-W_4 which all lie in the specimen plane can be set according to Equation (5.1) to define the direction of the axes frame {W} of the QR code, such as Y is the main axis of welding for the specimen. The coincidence of the direction of frame {W} and robot motion frame {B} as depicted in Figure 5.2, provides an easy way to interpret the difference that will exist in the pose between the welding specimen and robot base. P3P is deployed to estimate the rotational array R_{3x3} which refer to the orientation of specimen frame {W} relative to the camera

134

frame {E} and translation t_{3x1} of the camera principal point (centre) from the point W_1 which represents the origin of the QR code to the camera frame{E} and both constitute the pose eHw (Equation (5.2)).

$$\begin{cases} I_1 = (u_1, v_1) \\ I_2 = (u_2, v_2) \\ I_3 = (u_3, v_3) \\ I_4 = (u_4, v_4) \end{cases} \text{ and } \begin{cases} W_1 = (0,0,0) \\ W_2 = (0, m, 0) \\ W_3 = (m, m, 0) \\ W_4 = (m, 0, 0) \end{cases} \tag{5.1}$$

$$eHw = \begin{bmatrix} r_{11} & r_{12} & r_{13} & t_x \\ r_{21} & r_{22} & r_{23} & t_y \\ r_{31} & r_{32} & r_{33} & t_z \\ 0 & 0 & 0 & 1 \end{bmatrix} \tag{5.2}$$

Utilizing Equation (2.1) the pose of the QR code relative to the robot base can be estimated. The accuracy of the estimation depends on the error from the TCP calibration, reprojection error from the camera calibration and Hand-Eye calibration. Nevertheless, the user's input to place the QR code in parallel with the main axis of welding affects the degree that which the pose of the fiducial marker represents the actual pose of the specimen.

5.3.2.   Adapting the Pose of the Welding Torch

Control of the weld pool, sufficient penetration and fusion with the base material are linked with parameters such as the orientation of the electrode relative to the joint and the direction and location of the arc. Generally, the positioning of a welding torch is described by work and travel angles (as shown in Figure 5.3), where incorrectly defined parameters can cause adverse effects such as porosity, weld undercut and slag entrapment [25]. Hence, the adaption of the pose of the welding torch relative to the pose of the specimen can

improve the quality of welding and avoid the generation of possible collisions with existing fixtures or clamps.
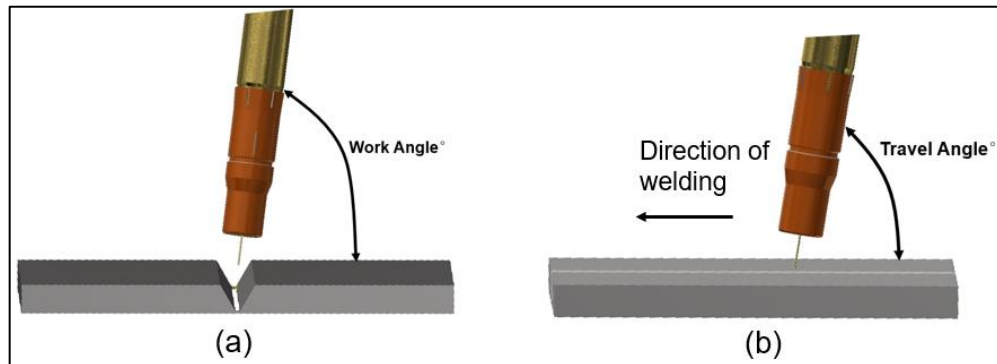
Figure 5.3. Orientation of the torch during welding: (a) Indicates the working angle of the torch formed by a line perpendicular to the major surface of the workpiece and a plane determined by the electrode axis and weld axis (b) The travel angle of the torch dictates the welding technique which can be forehand or backhand, based on the direction of the electrode relative to the welding direction [25].

5.3.3. Calibration of the TCP Orientation

Adjusting the work and travel angle of the welding torch requires the accurate extraction of the pose of the specimen and the motion of the TCP of the robotic arm relative to that identified frame. Since the extraction of the pose of the specimen, which is described in Section 5.3.1, can identify the desired motion frame, the calibration of the TCP beforehand aids the alignment of the torch relative to the specimen. As shown in Figure 5.4, the TCP is calibrated such that the X-axis is pointing in the direction of the electrode wire and the orientation of the Z-axis forms 90° with the electrode wire passing through the middle plane of the torch.
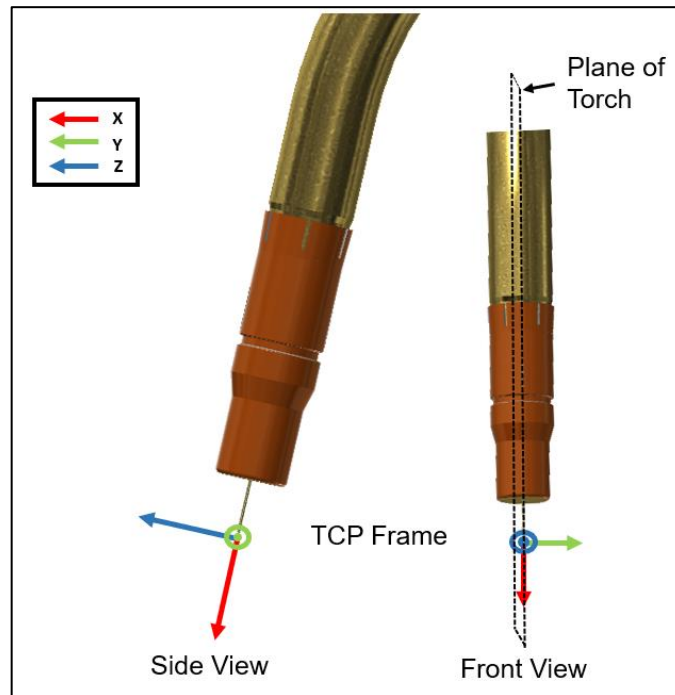
Figure 5.4. Adjusting the orientation of TCP calibration

5.3.4. Initial Adjustment of Welding Torch's Pose

Following the extraction of the pose of the specimen relative to the base of the robot using the QR marker, then the pose of the welding torch will adapt (initially) relative to this extracted pose.

Supposing that the TCP of the robotic arm is in a random position relative to the specimen frame {W} and assuming that this is the starting position to perform corrections on the robot path (see Figure 5.5a where the laser scanner is removed for better visualization), the adjustment of the pose of the torch {G} for a specimen with pose {W} relative to robot base frame {B}, is described by the Euler angles A, B, C respectively. The first target of the robotic arm, moving the TCP relative to frame {W}, is assigned Euler angles following the ZYX convention of KUKA, of A=90°, B=80°, C=0°. This can be seen in Figure 5.5b,

137

where irrespective of the orientation of the specimen frame {W} relative to the robot base {B}, a 90° work angle is achieved, and a start travel angle of 10°. This is a standard configuration in forehand welding with solid wire. The angle C is selected to be 0° for the laser scanner which is mounted in the welding torch to align the projected laser stripe 90° relative to the main axis of welding Y, as seen in Figure 5.5c and Figure 5.6c, exploiting the full range of the scanner in order to extract geometric features of the V-groove. Table 5.2 stores the poses of frame {G} relative to {W} as illustrated in Figure 5.5. The selection of these angles aligns with the laser scanner optimum incidence and steepness angles found in Section 3.3.3 to extract reliable measurements during inspection of the specimen.
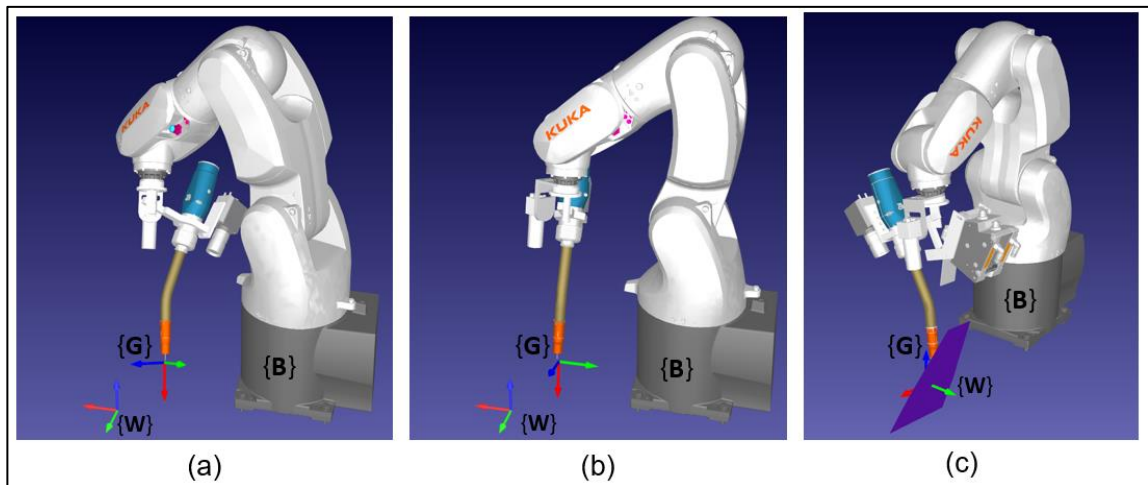
Figure 5.5. Adjusting pose of torch {G} relative to identified pose of specimen {W}: (a) Random initial pose of welding torch {G} relative to identified frame {W}, (b) Adjusted pose of torch relative to {W} resulting in 90° work angle and 10° initial travel angle, (c) Welding torch 20 mm and 50 mm relative to the origin of frame {W} to show the adjustment of the pose.
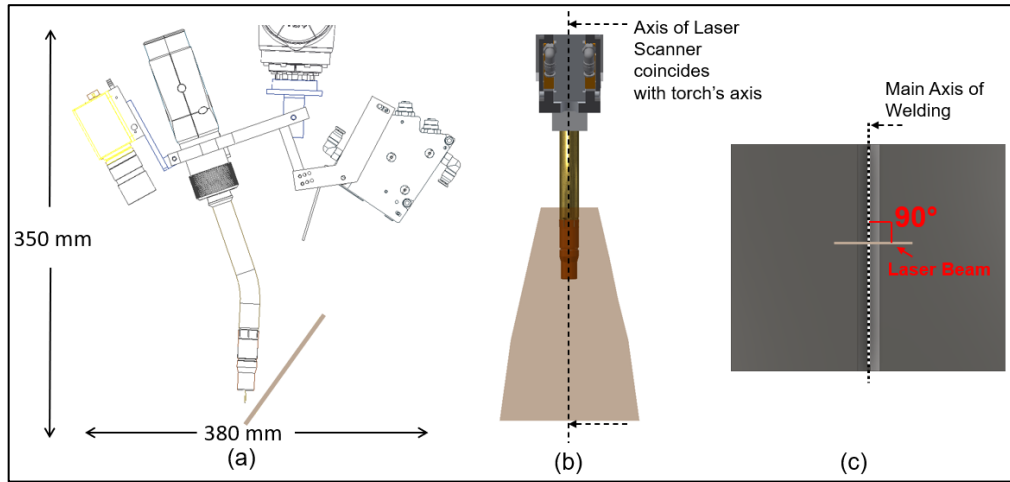
Figure 5.6. Laser stripe forms 90° relative to main axis of welding for angle C=0°: (a) Side View, (b) Front view, (c) Top View with projected laser stripe in a single-sided V-groove.

Table 5.2. Poses of the welding torch adapted to estimated specimen frame {W}

#Pose of {G} relative to {W}	X	Y	Z	A	B	C
Figure 5.5a	-59.27	-25.78	122.22	96.60	62.79	48.86
Figure 5.5b	-59.27	-25.78	122.22	90	80	0
Figure 5.5c	0	20	50	90	80	0

5.3.5. Compensating for Vision and Human Error through Laser Scanning

Since a human place the fiducial QR code marker in parallel with the main axis of welding, an error can be introduced in the pose of the QR code which represents the specimen's

139

pose. Moreover, an error is accumulated from the TCP calibration, camera calibration and hand-eye calibration setup, referred to here from now on as vision error. Hence, the initial assignment of the Euler angles described in Section 5.3.4 will not result in the desired A, B and C angles with the specimen due to an error in the identified pose of the QR code. Consecutively, the laser scanner which follows the induced motion of the welding torch will not move in a constant height relative to the specimen due to the error in the assigned motion frame of the QR code, generating false measurements in the set ROI regarding bevel height, root-face, and root gap measurement.

Following the specimen's pose extraction process and the associated adjustment, the TCP is assigned a second target relative to the frame of motion {W} in order to approach the origin of the QR code which has X=0, Y=0, Z=0 and the same pose as in Figure 5.5b (A=90°, B=80°, C=0°). A touch sensing routine is utilized through the welding equipment's digital connection output to drive the welding torch within the V-groove. The welding torch descends in small increments of 3 mm to avoid a crash with the specimen, while at the same time checking if the digital signal of touch sensing is received to the NI-9425 module of the cRIO (Section 3.2.3). Once the digital signal is received, the touching height is recorded, and the torch is driven inside the V-groove in increments of 5 mm until the height difference becomes smaller than 2 mm. At that point it is ensured that the welding torch lies inside the V-groove and is aligned with the middle of the seam through the laser scanner internal function to identify the V-groove start-end points. Algorithm 1 describes the touch sensing routine that is used to drive the welding torch within the V-groove.

Algorithm 1: Touch Sensing Routine

Data: X_position, Angle_B, Times_Touched, Z_Touched_Position, Touched_Position, Z_threshold, Touching, Z_Position, Wire_Touched, Target_Z

1   *Times_Touched* ← 0; *X_position* ← 0; *Touching* ← TRUE; *Z_Position* ← 0;

2   *WHILE* (Touching)

3   *Z_Position* ← Z_position-3;

4   *IF* Wire_Touched

5   *Touched_Position* ← Robot_Position; *Times_Touched* ← Times_Touched+1; *Target_Z* ← Z_Position+10

6   *IF* Timed_Touched > 1

7   *IF* abs(Angle B) > 5 { *Z_Threshold* ← 4; *ELSE Z_Threshold* ← 2; }

8   *END*

9   *IF* abs(Z_touched_Position(**Times_Touched**)-Z_Touched_Position(**Times_Touched-1**)) > Z_Threshold

10   *Touching* ← FALSE;

11   *ELSE*

12   *X_position* ← Times_Touched·(-5);

13   *END*

14   *ELSE*

15   *X_position* ← Times_Touched·(-5);

16   *END*

17   *END*

Algorithm 1 Touch sensing routine to drive laser scanner within the groove.

The placement of the QR code as depicted in Figure 5.7a introduces an error in angle A

which describes the rotation of the specimen around axis Z of QR code frame {W}. Due

to that error, the laser scanning process which extracts the root pass welding reference

path and the geometric features is affected. To compensate for the introduced error in

angle A between the QR frame {W} and the actual orientation of the specimen, the TCP

of the welding torch continues to move back at the start and end of the specimen relative

141

to the identified frame {W} while the laser scanner identifies the middle of the seam to record P_{start} and P_{end} points along with their X and Y coordinates. In this manner, the corrected slope of the seam path in the X-Y plane of {W} is calculated and the arctan of that slope is added as angle difference relative to the extracted angle A. The process recorded in Algorithm 2 compensates for the introduced error in angle A between the QR frame {W} and the actual orientation of the specimen.
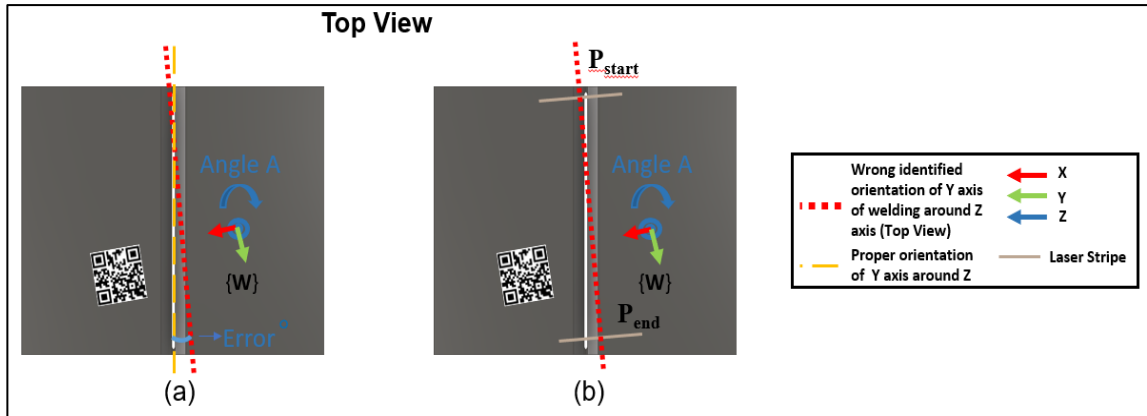
Figure 5.7. Misplacement of QR code affects the angel A of torch relative to Z-axis of {W}: (a) The wrong axis of welding forms angle A+|error°| around the desired axis of welding Y, (b) P_{start} and P_{end} are recorded while the laser scanner moves the TCP to the middle of the seam and X, Y coordinates of TCP are recorded on these points

---

Algorithm 2: Compensate for error in angle A around Z axis

    Data: *A angle, x_start, x_end, y_start, y_end, actual_A_angle , slope, theta*

1   *slope←(x_end-x_start)/(y_end-y_start)*

2   *theta←rad2deg(atan(abs(slope)))*

3   *IF (slope <0)*

4   *actual_A_angle← A angle+theta*

5   *ELSE*

6   *actual_A_angle← A angle-theta*

7   *END*

Algorithm 2 Compensates for the error in angle A around Z axis using the start and end points from laser scanner inspection in X-Y space of frame {W}.

Similarly, to the placement of the marker and vision error that may exist, an additional potential error associated with angle C, which describes the orientation of the specimen around axis X of frame {W} and is related to the travel angle, has been assessed and alleviated. As can be seen in Figure 5.8, for the wrong identified angle C from hand-eye calibration, the laser scanner will not move at a constant height relative to the specimen, cause the welding torch's TCP was moving relative to a wrong frame of motion, generating false reflections for the ROI assigned to measure bevel height, root-face, and root gap measurement. To estimate and compensate for that error, the TCP visits three key points while moving relative to the motion frame {W} as can be seen in Figure 5.9. These points are the identified start, end of the specimen and the point related to the origin of the QR code following touch sensing. At each of the three points, the distance of the laser scanner from the specimen must be equal to the predefined distance of the laser scanner from the top of the specimen, as recorded in the first key point. The predefined distance is selected to be 245 mm from the laser scanner to the specimen according to the performance assessment of the laser scanner in Section 3.3.3. As the robotic arm progresses to key points two and three, the feedback from the scanner offsets the TCP of the welding torch to match the predefined distance from the surface, recording the coordinates of Ystart, Zstart and Yend, Zend of the TCP in Y-Z space. These coordinates are used to calculate the slope of the seam path in the Y-Z plane of {W}, and the arctan of this slope is added as the angle difference in the original measured angle C. The process for compensating and the estimation of the actual angle C is described in Algorithm 3.
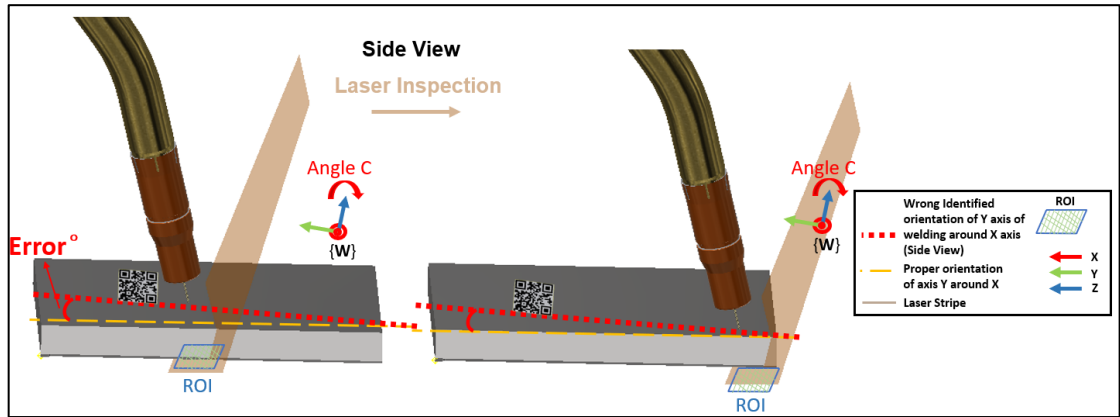
Figure 5.8. Error in angle C causes the laser scanner to inspect in different heights over the specimen length, causing the ROI for gap measurement to offset from the desired area of inspection
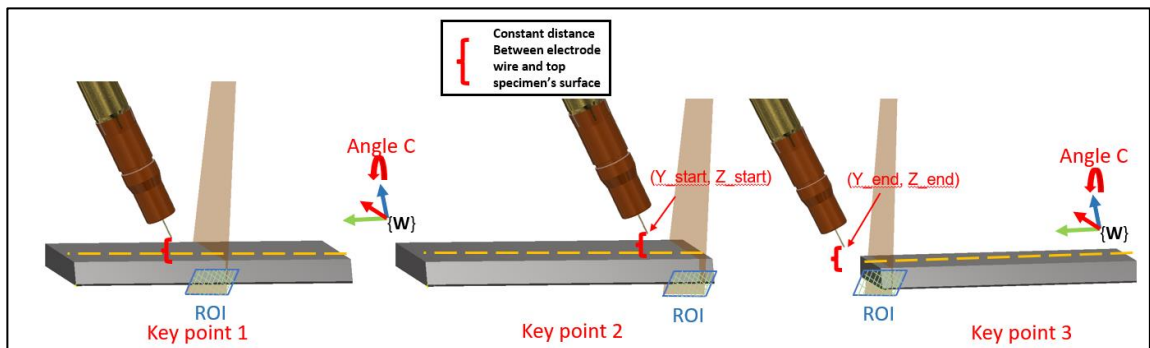
Figure 5.9. To compensate for the error in angle C, the laser scanner height measurement offsets the TCP of the torch relative to the top surface of the specimen keeping it constant along with the whole specimen

Algorithm 3: Compensate for error in angle C around X axis

      Data: C angle, z_start, z_end, y_start, y_end, actual_C_angle , slope, theta

1   *slope* ← (z_end-z_start)/(y_end-y_start)

2   *theta* ← rad2deg(atan(abs(slope)))

3   *IF (slope < 0)*

4   *actual_C_angle* ← psi angle-theta

5   *ELSE*

6   *actual_C_angle* ← psi angle+theta

7   *END*

Algorithm 3. Compensates for the error in angle C around X using the start, end points from laser scanner inspection in Y-Z space of frame {W}, while keeping constant height between laser scanner emission point and specimen

Finally, and for completeness the error in angle B which represents the orientation of the specimen around the Y-axis (the main axis of welding), is identified from the internal measurement of the laser scanner using the inherent principle of triangulation.

With the vision and human-introduced errors identified, the welding system initiates a second inspection of the specimen. Now the TCP of the welding torch moves relative to the new corrected frame {W} as is shown in the flowchart depicted of Figure 5.10. The described process identifies the required points to generate the root-pass path used as a reference welding path for all the subsequent passes. Moreover, the key features of the V-groove geometry are extracted and are used as an input to the multi-pass welding system in order to populate the welding schedule (Chapter 4).
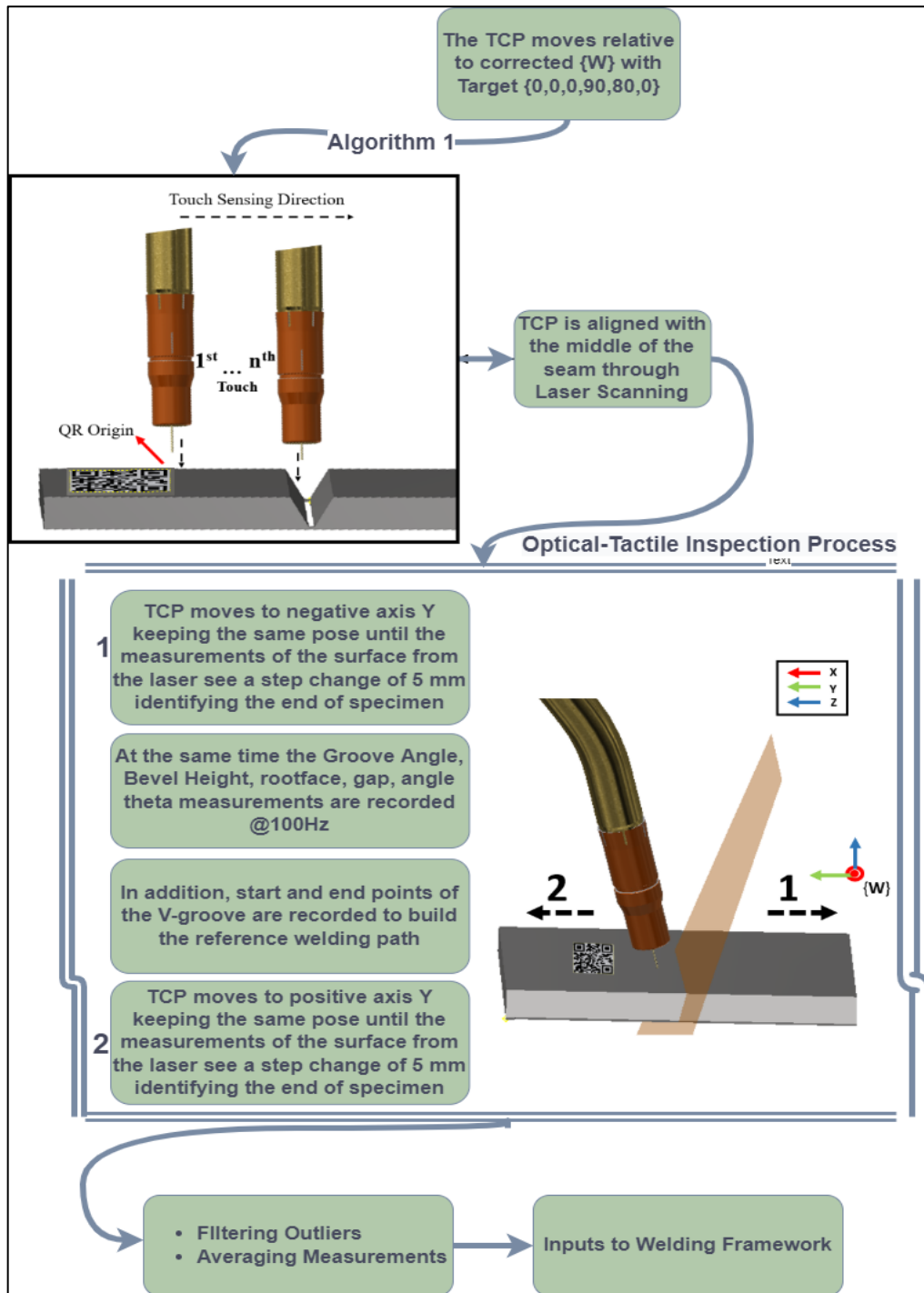
Figure 5.10. The V-groove dynamic inspection process for generating the root-pass path is used as a reference welding path and measurement of geometric characteristics which are used as inputs for the multi-pass welding system

146

5.4. Proof-of-Concept Experimental Verification

A series of Proof of Concept (POC) experiments were undertaken to prove, validate and characterize the flexibility and the autonomous capability of the developed holistic robotic welding system while identifying a V-groove joint in the scene, adapting the pose of the welding torch relative to the V-groove, extracting the welding reference path, and finally deploying automated multi-pass arc welding.

5.4.1. Automated Extraction of Features and Reference Welding Path

The first set of experiments was undertaken to characterize the automated robotic welding systems' autonomous ability to identify single-sided V-grooves in the scene, adapting its welding torch pose relative to the groove, in such a way that the features of the groove and the welding reference path can be extracted with high accuracy and can perform welding with a forehand technique [25]. For that purpose, a V-groove joint was placed in four different positions-orientations within $\pm10°$ of the base of the robot, as can be seen in Figure 5.11, acknowledging that these bounds are usually met within realistic high integrity welding configurations. The geometric characteristics of the V-groove joint are recorded in Table 5.3.

In each configuration, a human operator manually placed a square QR code of fixed edge size 60.1 mm in parallel with the main axis of welding. Choosing a 60.1 mm QR code was found to be within the depth of field of the camera (which was calculated at 350 mm) and the selected scene where the robotic arm operates. The robot retracts, extracts a pose of

the scene, and based on Section 5.3.1 and Equation (2.1) both translation and pose of the QR code are calculated relative to the robot motion frame. Figure 5.12 depicts the process of identifying autonomously the specimen's pose, utilizing the vision result of the hand-eye calibration, adapting the torch's pose based on Section 5.3.4, and extracting the groove features and reference welding path for the root pass.
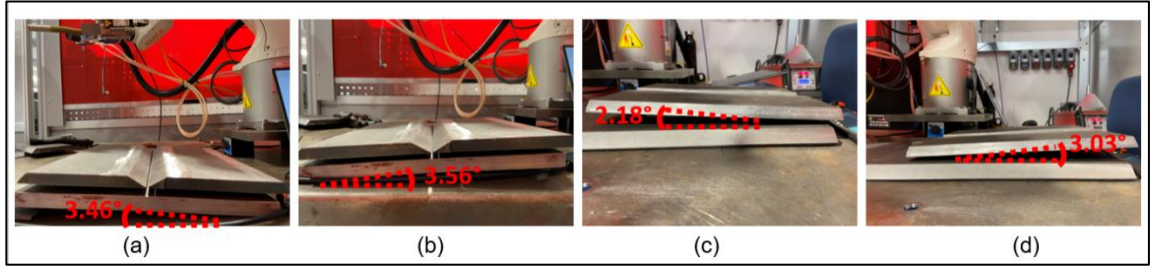
Figure 5.11. Four random poses of V-groove joint relative to the robot base. For better illustration, the formed angles of the specimens relative to the robot base are sketched based on the plane that the picture was taken with red dotted lines. For (a) and (b) the angles are relative to the Y-axis which is the main axis of welding and for (c) and (d) the angles are relative to X-axis. These angles are calculated by extracting the pose of the QR code through Hand-Eye calibration and following the compensation for vision and human error through the laser scanning algorithmic processes described in Section 5.3.5

Table 5.3. Reference geometric characteristics of the V-groove joint used for the first set of experiments in four different poses

V-Groove Geometry Features	
Groove Angle (°)	120
Root Gap (mm)	2
Root-face (mm)	1.1
Length of joint (mm)	300
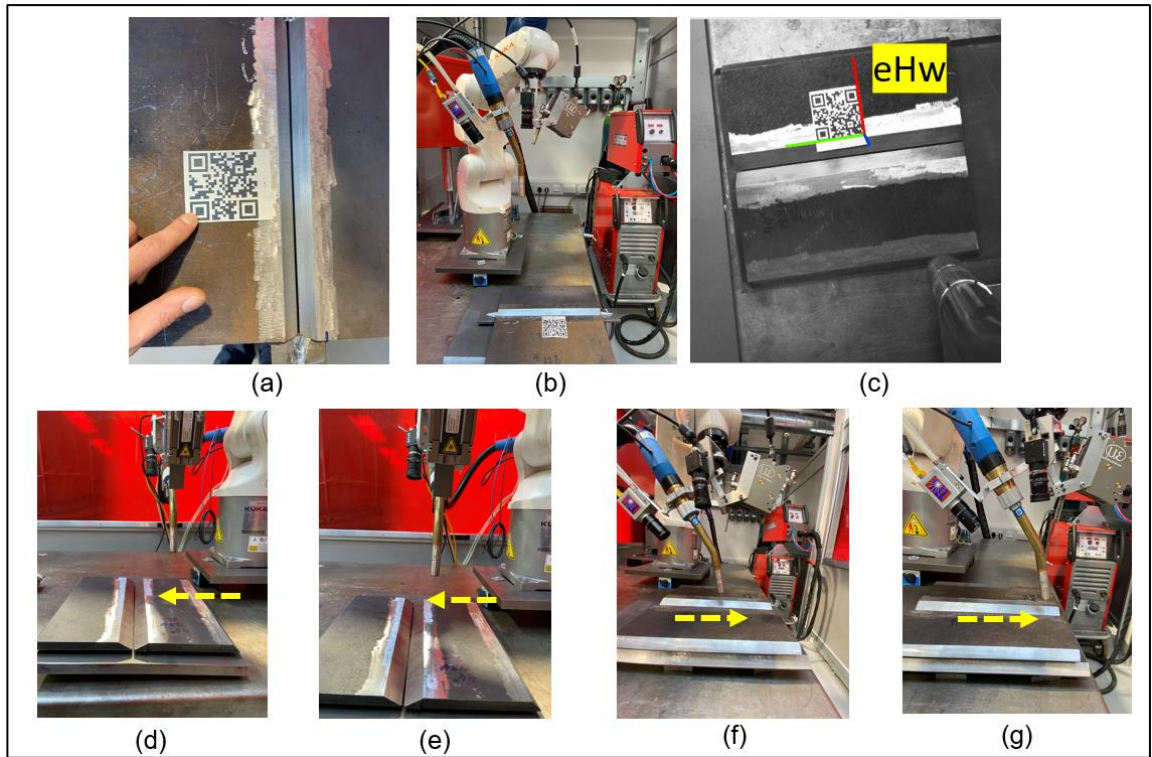
Figure 5.12. (a) A human placed the QR code in the specimen with one edge in parallel with the seam (axis of welding), (b) The robotic arm retracts to grab an image of the scene, (c) the Algorithmic process described in Section 5.3.1 estimates the pose eHw of the QR code relative to the camera optical centre (overlayed in the image), (d) The welding system utilizes Equation (2.1) to estimate the pose of the specimen relative to the robot base in the initial position of the torch, (e) The welding torch adapts its pose relative to the specimen (Section 5.3.4), (f)-(g) Groove characteristics and reference welding path are extracted trough tactile and optical sensing along with the specimen

Subsequently, the geometrical features of the single-sided V-groove and the welding reference path were extracted according to the algorithmic process described in Figure 5.10. Lastly, the same process was repeated but this time the algorithms described in Section 5.3.5 were utilized where the laser scanner compensates for the vision and human-introduced error from the manual placement of the QR code.

The accuracy of the extracted features of the groove was compared in both cases with the actual ones from Table 5.3, resulting in Table 5.4, where the maximum error and the percentage reduction of the error for the four different orientations with and without compensating for the vision and human error is recorded.

Table 5.5 depicts the error per pose of the welding joint on the extracted features of the groove following compensation for the vision and the human error.

Lastly, Table 5.6 stores the maximum error on the extraction of the reference welding path between the four different orientations when the algorithmic process described in Section 5.3.5 is not utilized.

Table 5.4. The maximum error between the four different orientations (Figure 5.11) on extracting the geometrical characteristics of the V-groove with and without compensating for the Vision and Human Error

Groove Features	Error -Without Compensation	Error following Compensation (Section 5.3.5)	% Percentage error reduction after compensating
Groove Angle (°)	5.78	0.76	**-86.8%**
Root Gap (mm)	1.03	0.22	**-78.6%**
Root-face (mm)	1.69	0.11	**-93.49%**
Length of joint (mm)	3	0.4	**-86.66%**

Table 5.5. Error on the extracted groove features for each pose of the V-groove joint (Figure 5.11) following compensation for the vision and human introduced error

Groove Features	Pose (a)	Pose (b)	Pose (c)	Pose (d)	Average Error
Groove Angle (°)	0.00	0.56	0.28	0.76	0.40
Root Gap (mm)	0.04	0.07	0.22	0.10	0.18
Root-face (mm)	0.03	0.11	0.09	0.04	0.06
Length of Joint (mm)	0.01	0.09	0.00	0.40	0.12

Table 5.6. The maximum error in translation and rotation on the extraction of the reference welding path for both Start and End weld points between the four different orientations of the V-groove joint when the compensation for vision and human error does not take place.

Max Path Error	X (mm)	Y (mm)	Z (mm)	A (°)	B (°)	C (°)
Start Point	1.78	3.94	1.41	1.01	1.15	0.8
End Point	2.08	0.08	1.11	1.01	1.15	0.8
In total	**2.08**	**3.94**	**1.41**	**1.01**	**1.15**	**0.8**

Also, Figure 5.13 depicts the error in the extracted pose of the welding specimen from Figure 5.11(d) through the difference in the pose of the two depicted coordinate frames. The error on the angles was found to be A=0.38°, B=1.15°, and C=0.26° after compensating with the algorithmic laser scanning process.
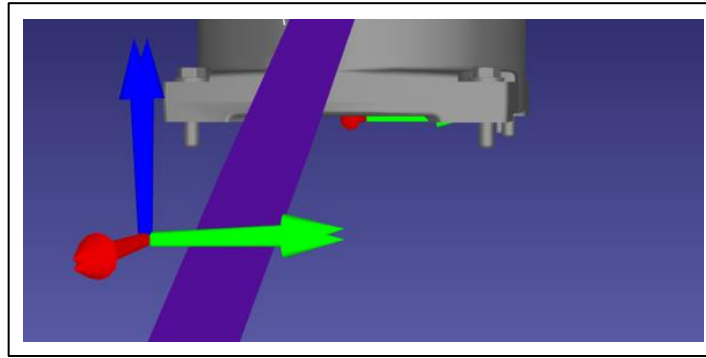
Figure 5.13. Correcting the welding torch's pose relative to the pose of the specimen, through laser scanner compensation algorithmic process in Section 5.3.5

5.4.2.   Automated Multi-Pass Arc Welding Trials

The second set of experiments was related to fully automated welding trials for three single-sided V-groove joints of structural steel grade S-275. These joints were manually placed within the robotic working volume at various $\pm 10°$ angles relative to the robot base. The autonomous identification of the pose of the specimen, compensation for vision and human error and finally the utilization of the tactile and optical sensing process led to the extraction of the groove characteristics and the reference welding path as described in Section 5.4.1. Subsequently, the groove characteristics were used as an input to the multi-pass welding system described in Chapter 4, along with the measured root offset from the root-face through the laser scanner, to populate the welding schedule for all welding passes per layer, except the root and hot pass welding parameters which are provided from the user. The consistent quality of the weldments was validated afterwards with PAUT.

The V-groove joints (S-275) used for experimental validation are commonly found in marine and manufacturing configurations where the characteristics of these were captured from tactile and optical inspection process and are recorded in Table 5.7.

Table 5.7. Extracted features through the optical and tactile inspection process (Figure 5.10) of the three single-sided V-grooves following vision and human error compensation process

Geometric Features	Joint 1	Joint 2	Joint 3
Thickness (mm)	15.40	15.10	9.87
Groove Angle (°)	87.02	86.81	91.60
Root Gap (mm)	2.15	2.10	2.22
Root-face (mm)	1.81	1.57	2.06
Length of joint (mm)	299.98	300.02	299.98
Root-offset (mm-after root-pass)	3.78	3.35	3.34

The pose of each specimen relative to the robot base following the compensation for vision and human error can be seen graphically in Figure 5.14 and is recorded in Table 5.8.
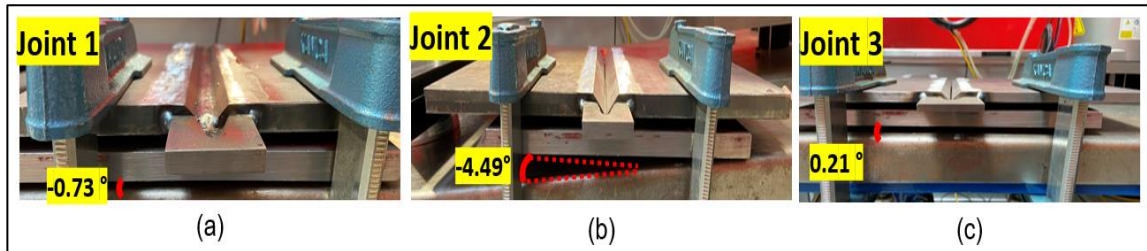
Figure 5.14. Extracted poses of the joints following compensation of vision and human error. (a), (b) and (c): Front plane angle relative to robot base, which is the angle of the specimen relative to Y axis of the WORLD frame of the robot, found physically in the root of the robot

153

Table 5.8. Identified origin of QR code relative to WORLD base of the robot and corrected pose of the specimen following the algorithmic process from Section 5.3.5

Joint 1						
	Identified Origin of QR code (relative to robot WORLD Base)			Orientation of QR code – Specimen (relative to robot WORLD Base)		
	X (mm)	Y(mm)	Z(mm)	A (°)	B (°)	C (°)
Initial Pose	375.05	201.8	-22.72	-1.24	2.39	-1.78
Corrected Pose	-	-	-	-1.01	-0.73	-0.95
Joint 2						
	Identified Origin of QR code (relative to robot WORLD Base)			Orientation of QR code – Specimen (relative to robot WORLD Base)		
	X (mm)	Y(mm)	Z(mm)	A (°)	B (°)	C (°)
Initial Pose	383.62	214.32	-15.59	-1.49	-0.66	-0.45
Corrected Pose	-	-	-	-0.62	-4.49	-0.33
Joint 3						
	Identified Origin of QR code (relative to robot WORLD Base)			Orientation of QR code – Specimen (relative to robot WORLD Base)		
	X (mm)	Y(mm)	Z(mm)	A (°)	B (°)	C (°)
Initial Pose	374.47	198.32	-29.46	3.01	2.75	-0.91
Corrected Pose	-	-	-	2.51	0.21	0.05

The multi-pass welding system described in Chapter 4, was initialized with a deposition coefficient $a_H = 1.03$, weaving factor $\delta = 2\ mm$, total height above specimen of 1 mm and four different welding parameter combinations which are recorded in Table 4.3. Figure 5.15 and Figure 5.16 depict the generated welding schedule for joints 1 and 3 along with the values of the allocated cost function C(80%,5%,15%) that was selected for all joints to result in the minimum number of passes.
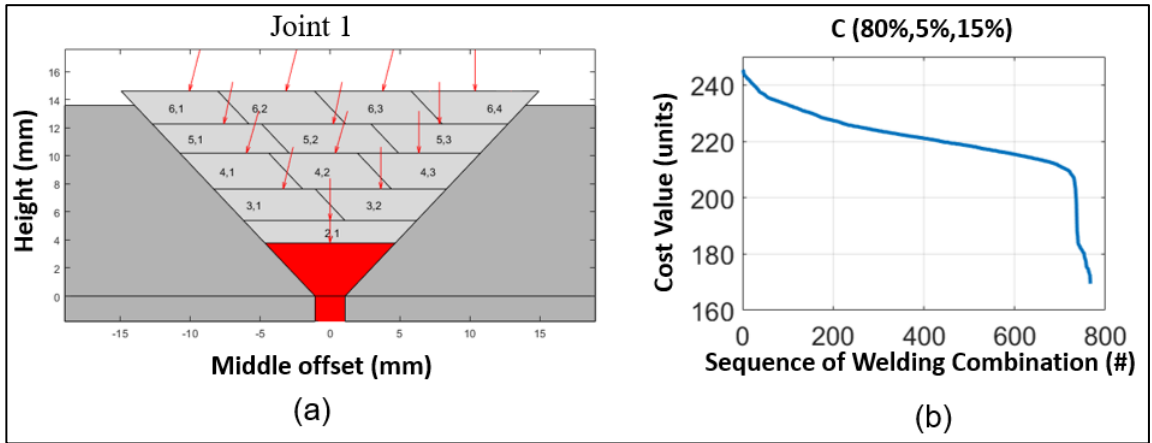
*Figure 5.15 (a) Generated welding schedule for joint 1 for the minimum cost value, (b)
Value of allocated cost function across all the possible welding combinations for this V-
groove geometry*
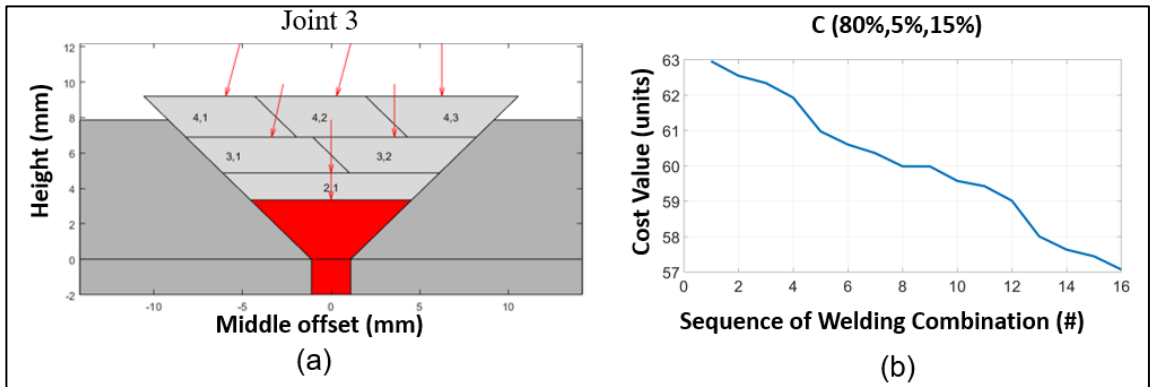
*Figure 5.16 (a) Generated welding schedule for joint 3 for the minimum cost value, (b)
Value of allocated cost function across all the possible welding combinations for this V-
groove geometry*

Table 5.9 to Table 5.11 provide the produced welding parameters per layer for each joint

respectively.

155

Table 5.9. Populated welding schedule and welding parameters per layer for joint 1

Layer Number (#)	Pass Number (#)	Wire Feed Speed (mm/s)	Robot Speed (mm/s)	Offset-middle of the seam (mm)	Height from root-face (mm)	Work Angle of torch (°)	Weaving Width (mm)	Consumable Material (g)	Arc Welding Time (s)
1	1	41.66	2	0	3.78	0	2.66	51.44	150
2	1	75	5	0	5.38	0	4.19	37.04	59.99
3	1	76.63	5.5	-3.36	7.62	13.41	2.82	34.41	54.54
3	2	76.63	5.5	3.62	7.62	0	2.68	34.41	54.54
4	1	76.63	5.5	-5.98	10.18	16.22	2.57	34.41	54.54
4	2	76.63	5.5	0.37	10.18	16.22	2.57	34.41	54.54
4	3	76.63	5.5	6.35	10.18	0	2.38	34.41	54.54
5	1	76.63	5.5	-7.59	12.25	11.97	3.00	34.41	54.54
5	2	76.63	5.5	0.22	12.25	11.97	3.00	34.41	54.54
5	3	76.63	5.5	7.81	12.25	0	2.89	34.41	54.54
6	1	76.63	5.5	-10.06	14.60	14.40	2.71	34.41	54.54
6	2	76.63	5.5	-3.15	14.60	14.40	2.71	34.41	54.54
6	3	76.63	5.5	3.75	14.60	14.40	2.71	34.41	54.54
6	4	76.63	5.5	10.37	14.60	0	2.57	34.41	54.54

Table 5.10. Populated welding schedule and welding parameters per layer for joint 2

Layer Number (#)	Pass Number (#)	Wire Feed Speed (mm/s)	Robot Speed (mm/s)	Offset-middle of the seam (mm)	Height from root-face (mm)	Work Angle of torch (°)	Weaving Width (mm)	Consumable Material (g)	Arc Welding Time (s)
1	1	41.66	2	0	3.35	0	2.23	51.45	150.01
2	1	75	5	0	5.08	0	3.86	37.05	60.00
3	1	76.63	5.5	-3.18	7.41	14.24	2.73	35.04	55.54
3	2	76.63	5.5	3.48	7.41	0	2.58	35.04	55.54
4	1	76.63	5	-5.82	10.26	17.59	2.70	37.85	60.00
4	2	76.63	5	0.45	10.26	17.59	2.70	37.85	60.00
4	3	76.63	5	6.27	10.26	0	2.48	37.85	60.00
5	1	76.63	5	-7.63	12.52	12.71	3.14	37.85	60.00
5	2	76.63	5	0.25	12.52	12.71	3.14	37.85	60.00
5	3	76.63	5	7.88	12.52	0	3.01	37.85	60.00
6	1	76.63	5.5	-10.20	14.84	14.15	2.74	35.04	55.54
6	2	76.63	5.5	-3.20	14.84	14.15	2.74	35.04	55.54
6	3	76.63	5.5	3.79	14.84	14.15	2.74	35.04	55.54
6	4	76.63	5.5	10.49	14.84	0	2.59	35.04	55.54

Table 5.11. Populated welding schedule and welding parameters per layer for joint 3

Layer Number (#)	Pass Number (#)	Wire Feed Speed (mm/s)	Robot Speed (mm/s)	Offset-middle of the seam (mm)	Height from root-face (mm)	Work Angle of torch (°)	Weaving Width (mm)	Consumable Material (g)	Arc Welding Time (s)
1	1	41.66	2	0	3.34	0	2.55	51.96	151.5
2	1	70	5	0	4.86	0	4.13	34.92	60.59
3	1	68.3	5.5	-3.36	6.88	12.29	2.73	30.97	55.08
3	2	68.3	5.5	3.58	6.88	0	2.62	30.97	55.08
4	1	68.3	5.5	-5.96	9.18	14.94	2.47	30.97	55.08
4	2	68.3	5.5	0.30	9.18	14.94	2.47	30.97	55.08
4	3	68.3	5.5	6.26	9.18	0	2.32	30.97	55.08

Figure 5.17 up to Figure 5.19 illustrate a time-lapse of the 14 welding passes for joints 1 and 2 and 7 passes for joint 3, validating the generated welding solution in terms of adequately filling the whole groove, resulting in a cap height above the top surface of average 0.9 mm. Moreover, the flexibility of the proposed automated welding system to identify and adapt to varying V-groove geometries within the welding volume is justified by the welding outcome. The wire of the torch is cut manually between passes in order to avoid contamination with subsequent welding passes and a five-minute break is utilized to limit heat input and remain within the temperature window (150°C-250°C) based on the WPS (Welding Procedure Specification) document produced from the weld procedure qualification record. Between formed layers, touch sensing through the welder digital output is used to identify the height of the last deposited layer relative to the root-face.
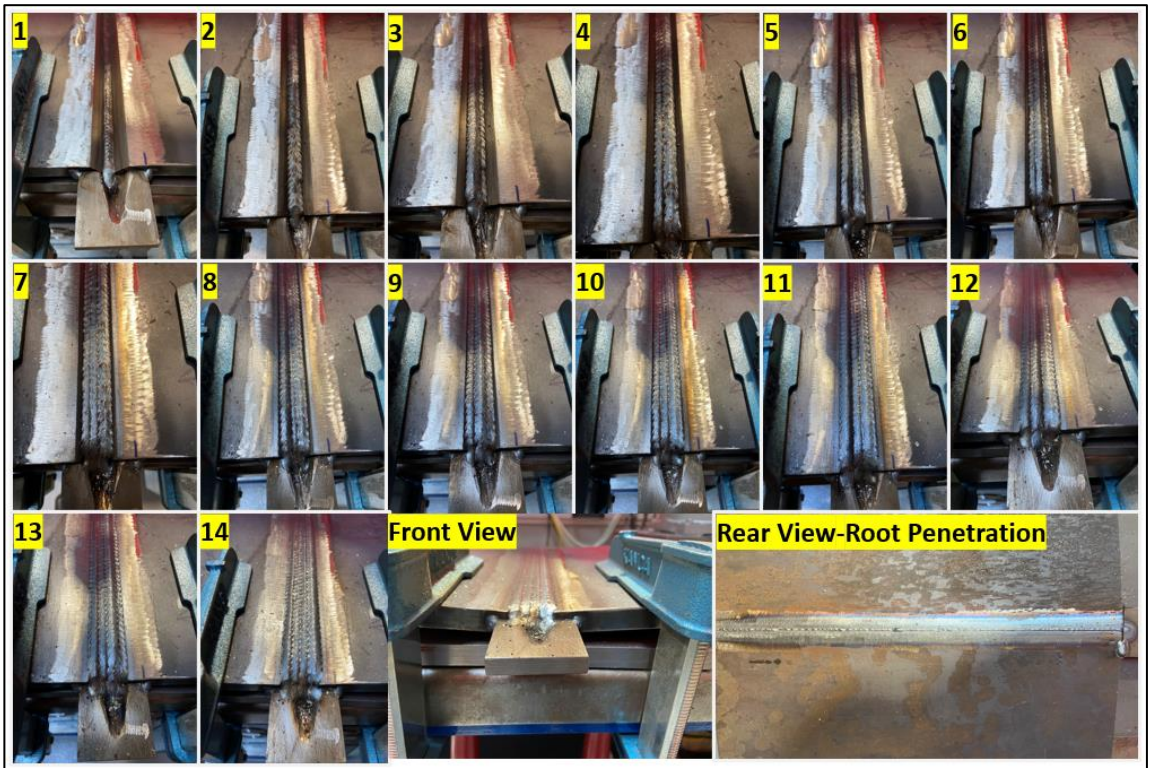
Figure 5.17. Multi-Pass welding system generated 14 welding passes based on cost function C(80%,5%,15%) for weld joint 1
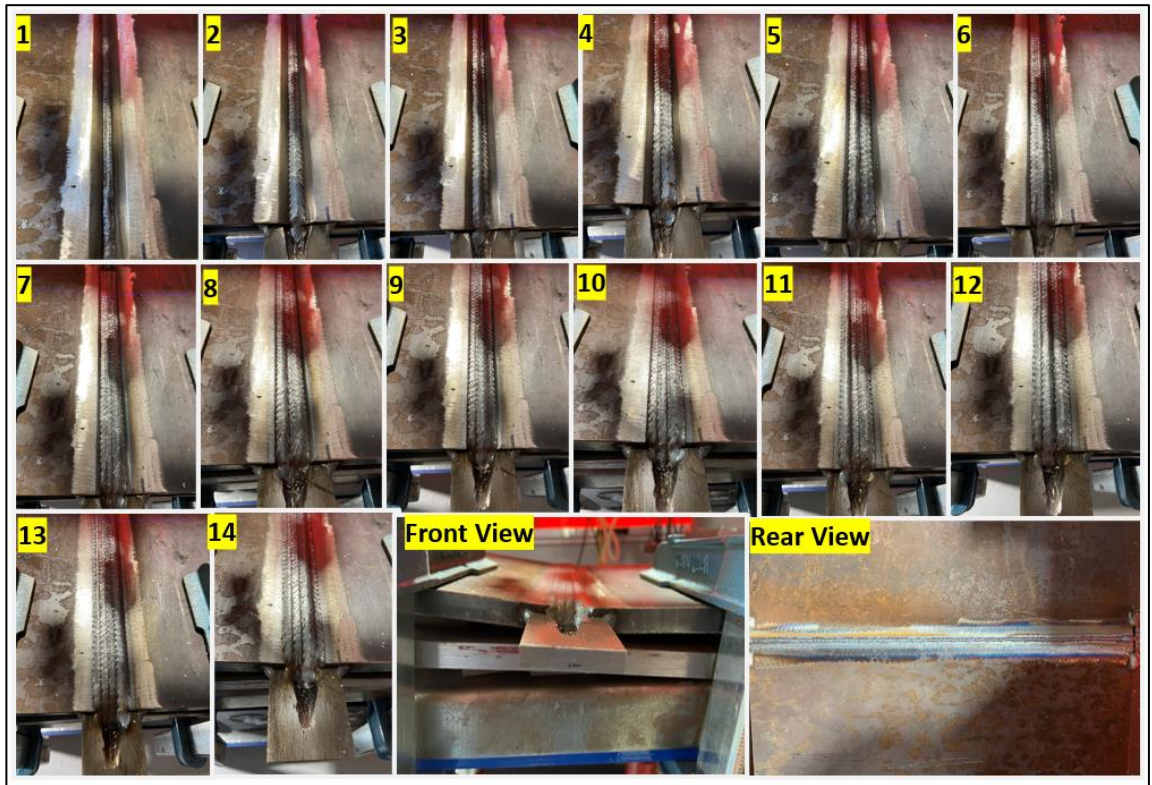
Figure 5.18. Multi-Pass welding system generated 14 welding passes based on cost function C(80%,5%,15%) for weld joint 2
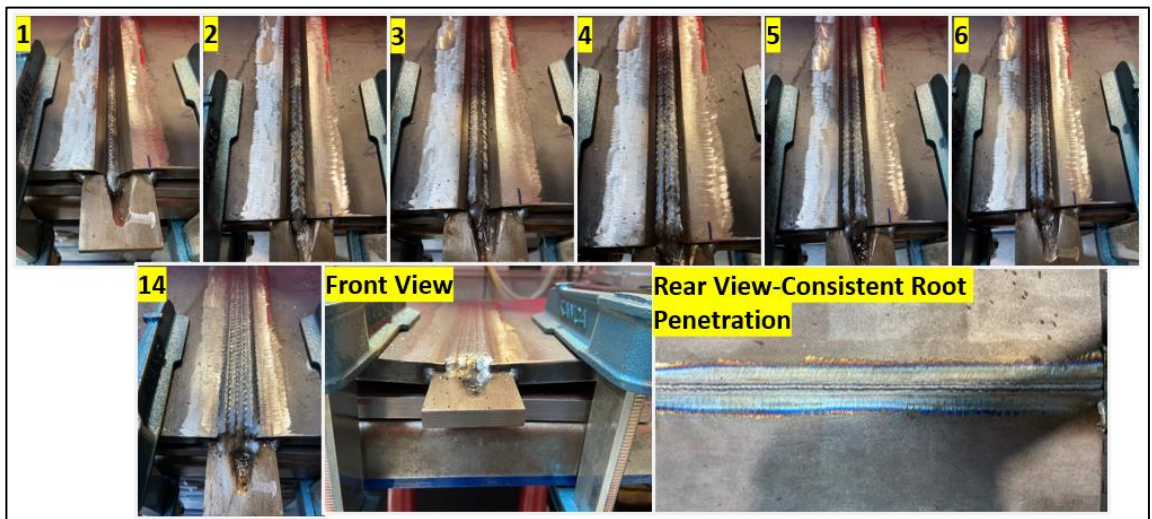
Figure 5.19. Multi-Pass welding system generated 7 welding passes based on cost function C(80%,5%,15%) for weld joint 3

5.4.3. UT Inspection for Defects

To assess the welding result of automated multi-pass arc welding trials, PAUT is utilized to inspect for defects in the welded samples [149]. The configuration for the inspection system can be seen in Table 5.12.

Table 5.12. Configuration of the PAUT inspection system

PAUT Configuration	Value / Description
Probe (MHz)	5
Voltage (V)	100
Elements of the array (#)	64
Pitch (mm)	0.5
Wedge Material	Ultem
Wedge Angle (°)	37.6
PRF (Hz)	2000
Pulse Width (ns)	100
Sector (°)	40-75
Controller	LTPA 64T/64R (Peak NDT, UK)

Gain calibration was performed according to BS EN ISO 17640 and any reflections from potential defects were compared with the reference signal. Figure 5.20 illustrates the calibration process where a phased array system inspects a welded sample of 15 mm thickness with two side-drilled holes of ø 2 mm. The gain was fixed at 55 dB and the signal from the side-drilled holes was received at an angle of 55° and was set at 80% of the screen height.

Adhering to the experimental calibration process each joint was inspected manually at room temperature along the main axis of welding. It was decided that indications above 40% on-screen height of the A-scans will indicate a possible candidate for a defect. For Joint 1, at 98.9 mm from the start of the sample, lack of root penetration was identified and is reported in Figure 5.21. This defect may have occurred due to misalignment of fitting of the parent metal plates during joint setup and uneven height of root face caused by manual machining of the weld grooves. Additionally, this was expected from the log file of the welding passes as depicted in Figure 5.22 which presents the welding current, voltage, and wire feed speed across the welding axis. The PAUT inspection of joints 2 and 3 did not give any indication of any potential defect above the set threshold. Lastly, there was no other indication of lack of fusion on sidewalls or inter-pass lack of fusion which is often encountered on welded joints during manufacturing [150].
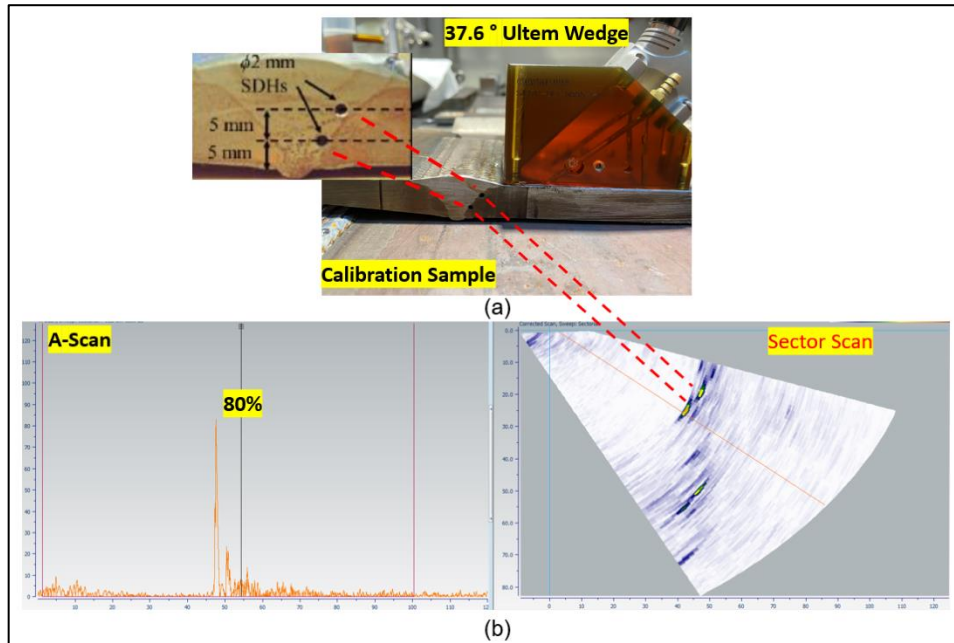
Figure 5.20. Gain calibration at 55 dB using a welded sample with two side-drilled holes of ø 2 mm for PAUT-NDT inspection: (a) Two side-drilled holes of 2 mm used as reflectors, (b) A-scan indicates the received signal from the reflector fixed at 80% of the screen height, and sector scan on the right showing the volumetric result of the inspection
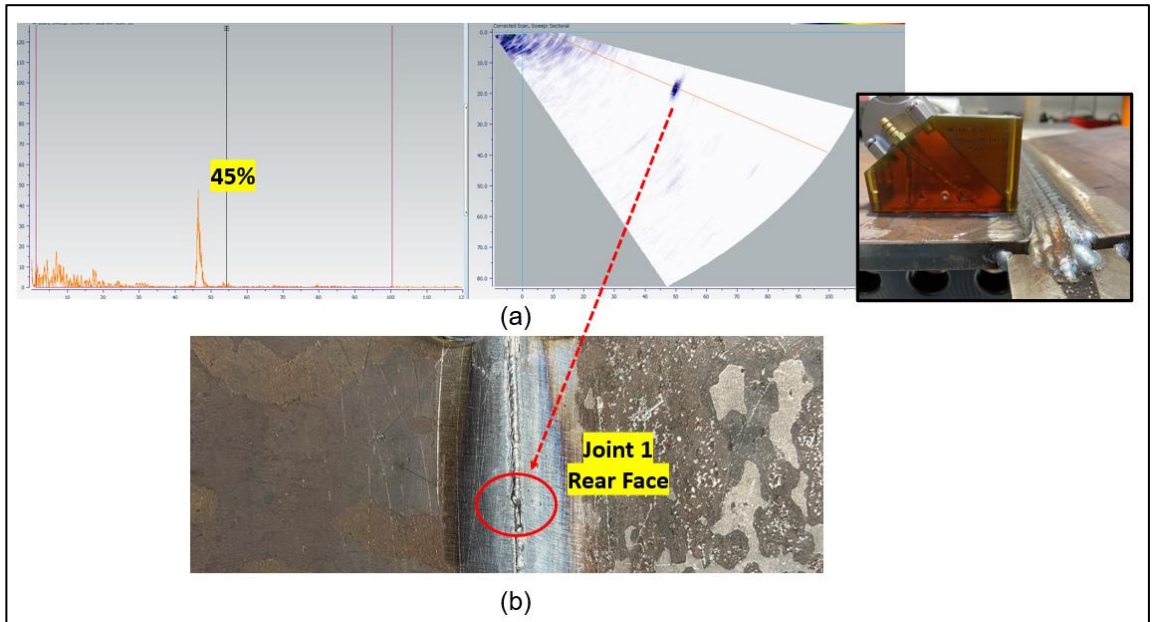
Figure 5.21. PAUT inspection and an indication of lack of root penetration for joint 1. (a) A-scan maximum value was 45% of the screen height, (b) Examination of the rear face indicated the lack of root penetration
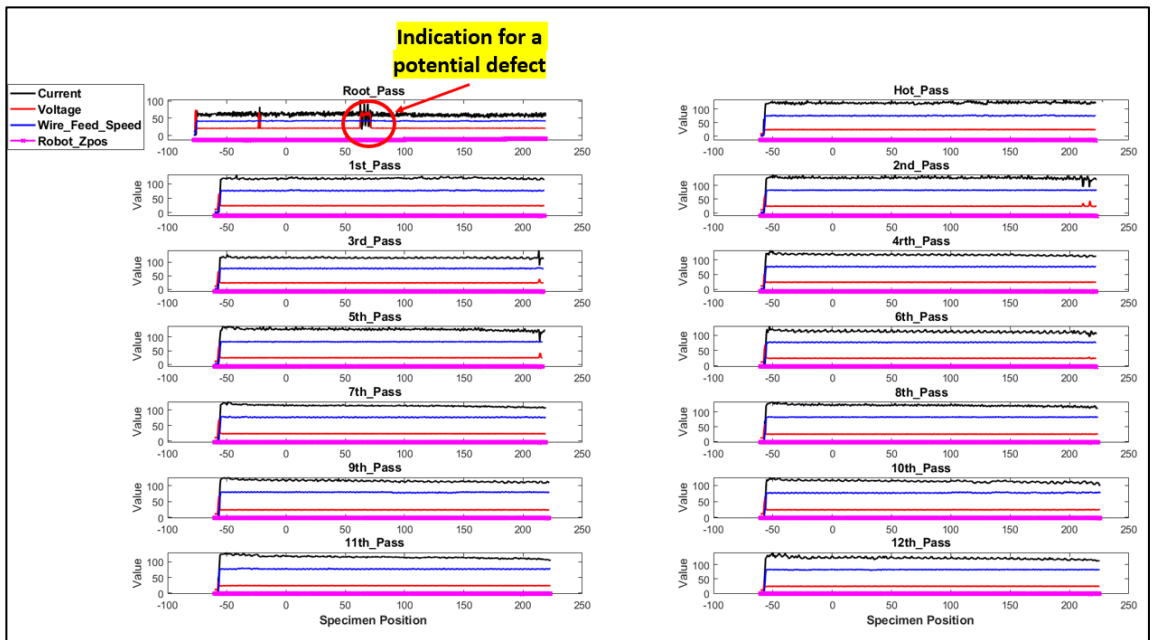
Figure 5.22. Log file of welded joint 1 which consists of a subplot of each welding pass displaying the instantaneous value of current, voltage wire feed speed and Z offset of the welding torch along the axis of welding

163

5.5. Discussion

Two sets of experiments were performed, following the developed methodology for workpiece localization and adaption to the welding configuration. The novelty of the proposed holistic automated robotic arc welding system was examined for its autonomous ability to: a) identify the scene and adapt the welding torch's pose relative to positionally unknown and unconstrained angled-placed welding specimens, b) extract the features of the V-groove and generate the welding reference path and c) finally deploy all the populated welding passes under a purely sensor-driven motion system. PAUT inspection validated the successful outcome of the fully automated welding result.

From the first set of experiments, the developed system was able to accurately extract the features of the single-sided V-groove for all four different poses and generate the reference welding path, which was used for all subsequent welding passes. Compensating for the vision and human error, that was introduced from the placement of the QR code in the specimen, the algorithmically sensor-driven approach achieved a maximum error of 0.4 mm and 0.76°; with an average 0.12 mm, 0.4° on the extraction of the features of the groove. This is a significant 86.38% average reduction in the error as compared to the process which relies only on the vision outcome, where the errors reached 3 mm and 5.78°.

In addition, it was essential to accurately adapt the pose of the welding torch relative to the welding joint for the tactile and optical process, in order to extract the welding reference path with high accuracy (< 1 mm). Without adaption of the pose to the specimen,

a maximum error of 3.94 mm and 1.15° was observed on the extraction of the reference path, which is not acceptable for robotic welding. It is worth mentioning that the developed process generates the accurate welding reference path for the root pass and subsequent passes, not only because it can be validated optically, but also due to the induced motion of the laser scanner relative to the specimen, which happens in a constant offset along the whole length of the specimen. This result reflects the correct estimation of the angle C of the specimen relative to the robot base {B}. Moreover, the end-effector's TCP motion follows the middle of the seam, which reflects the correct estimation of the angle A of the specimen relative to frame {B}. Also, through the laser scanner, the angle B relative to the Y-axis of welding has a zero offset.

The successful automated deployment of multi-pass robotic arc welding from start to end of three single-sided V-groove joints, which vary in geometric features and placement poses relative to the robotic arm, enhances the proof-of-concept of the developed automated welding system. A maximum error of 3.12°, 3.83° and 2.54° on the identified pose of Joints 1 up to 3 respectively, was corrected by the integrated algorithmic system and the system was able to complete the full multi-pass generated welding schedule without human intervention during welding.

Lastly, the integration of the developed external real-time motion module provided the foundation for a purely sensor-driven whole process approach, from identification, and inspection of the sample up to the subsequent deployment of each welding pass.

5.6. Conclusion

In this Chapter, an autonomous sensory-driven approach was developed, deployed, and experimentally validated in order to showcase automated multi-pass robotic welding for single-sided V-grooves. Dynamic localization of the pre-welded specimen in the scene, the adaption of the welding torch's pose for maximum accessibility, extraction of groove characteristics and generation of the reference welding path under a holistic external real-time control motion module builds a technology package for increased productivity and flexible robotic welding.

The introduction of a fiducial marker (QR code) in the scene provides a reliable and consistent user-initiated coarse localization method of the workpiece that requires welding. Also, the accurate extraction of geometric features of V-grooves, at different positions and orientations within $\pm 10°$ relative to the base of the robot was demonstrated ad validated. These limits are realistic within high integrity welding configurations. Compensating vision and human error as a consequence of placement of the QR code, resulted in a maximum error of 0.4 mm and 0.76°. The developed algorithmic process, which adapts the pose of the welding torch in such a way that a forehand welding technique can be applied at the same time as extracting an accurate ($<$ 1 mm) welding reference path, was compared relative to the inspection process of the sample which rely only on the vision result of the hand-eye calibration, resulting in an error of 3.94 mm and 1.15°.

Combining the presented developments with the external real-time motion module led to the full deployment of the holistic robotic welding system, used to inspect and perform automated multi-pass welding for three joints placed at an angle to the robot base. The feasibility of the proposed work was validated by examining the structural integrity of the weldments utilizing PAUT inspection. Lack of root penetration in Joint 1 was reported which may have arisen due to uneven fitting of the base plates. The lack of other defects such as undercuts or lack of sidewall fusion validates the overall success of the automated welding result.

Benefits arising for the manufacturing and nuclear sector from the developed sensor-driven approach highlight the flexible and robust character of the system to adapt the welding process for new V-grooves, which may vary in geometric features without the requirement of a custom fixed welding cell through adoption of this approach. In addition, minimum time for setup is required, since there is no need to teach manually robotic paths or adapt to existing CAD designs which increases the downtime of the production cycle. Overall, the developed technology does not require a robotic programmer or experience which may have a big impact on developing a business case, by driving the associated cost.

The presented work for automated multi-pass robotic welding was built on the current state of the art and can be realized as a technology package that can be applied directly to larger-scale robotics platforms with multiple DoFs based on the application's requirements.

Chapter 6

Conclusion and Future Work

6.1. Conclusion

Automated welding systems are deployed in factory production lines to aid in the fulfilment of increased and repeatable delivery of high-quality weldments. The production efficiency is affected by the decrease of skilled manual labour, due to harsh environmental conditions such as increased temperatures linked to infra-red radiation, and the concentration of gases, dust, and fumes. Nonetheless, welder retirement due to age profile further limits the available working pool of workers. Therefore, realizing the need for high integrity components drives the requirement for automated welding, an imperative need for the viable future of manufacturing.

Manual robot programming of welding paths, allocation of welding parameters, and adjusting the welding procedure manually for different workpieces are some of the challenges that the automated welding industry today is facing and therefore it struggles to exploit its benefits. These challenges can be tackled by proposing and adopting an

automated robotic welding system for repetitive welding tasks which will allow skilled welders to be utilized in more complex and creative welding tasks.

This thesis has investigated and researched the conceptualization, design, development, and deployment of an automated robotic arc welding system with immediate application in nuclear, offshore and oil and gas sectors.

A holistic and adaptive modular robotic welding system was developed to support the demonstration of the fully automated deployment of multi-pass arc welding for single-sided V-groove joints. The holistic welding system allows automated welding in confined spaces and features a flexible way to mount different metallic surfaces close to the pre-welded joint. The development and integration of the real-time low-latency sensor-driven motion module, based on the RSI interface, can generate and deploy the robot kinematics; influencing the robot end-effector's position and adapting the motion relative to the characteristics of the environment. Over and above the demonstrated project described herein, the developed motion module has been deployed in other projects and applications, allowing the realization and deployment of varying welding and NDT applications [136].

The development of a welding sequence planning system allowed the offline generation of welding parameters for each welding pass, the number of layers and welding passes based on a cost-function concept, which affects the direct welding costs for automated robotic welding technology. The proposed solution proved that it can adapt the generation of welding parameters to the geometric characteristics of the V-groove geometry, decreasing the time-consuming and cumbersome preparation of different welding configurations. POC experiments validated the adaption of the multi-pass welding system

to different V-groove geometries with enhanced welding quality, as proved through the final PAUT inspections. This approach benefits SMEs which are still showing reluctant to adopt automated robotic welding solutions due to the high variation and small volume of products that they handle.

Additionally, the developed advancements related to the dynamic user-initiated localization of the welding specimen and adaption of the welding torch enhance the flexibility of the demonstrated welding system by eliminating programming overhead between jobs. Finally, the automated generation of the welding reference path and the extraction of the groove features for the multi-pass welding system shaped a technology package with capabilities for fully automated multi-pass robotic welding. As a result, a key technology demonstrator was delivered for autonomous and high-quality multi-pass welding, as was proved from the POC trials and PAUT inspection.

The research described within this thesis lays the foundation for automated robotic welding intended for application small and constrained spaces, like those inside the hull of frigates; fulfilling the industrial requirements for minimum programming, adaption to the environment and delivery of high-quality weldments. Moreover, the demonstrated technology can be applied via different robotic arms, independent of robot manufacturer and size, linked with the application requirements and commercial benefits. Adopting more robotic welding systems on the production floor will further benefit welders, by replacing current tedious tasks. The future of the manufacturing sector will be shaped by the introduction of flexible welding solutions such as holistic and adaptive robotic welding systems enabling fast growth of robotic automation in production and repair processes.

6.2. Suggestions for Future Work

Investigating the established research goals of this thesis, led to the development of a state-of-the-art holistic and adaptive robotic welding system. The following sections describe future advancements of the established work, related to the system's flexibility, increased degree of adaption and enhanced quality of welding.

6.2.1. Holistic Sensor-Enabled Robotic Welding System

The flexible character of the developed holistic robotic welding system to mount on different metallic surfaces through magnets can be extended further by including also metallic rails. In that way, the reachability of the system will be increased and can potentially accommodate pipe welding and long seam welds, which are usually found on the open deck of ships. As a result, preparation time can be decreased further as for example the operator will not be required to re-mount the welding robot between jobs. Moreover, the prototype welding bracket associated with this thesis accommodates three vision sensors, a welding torch could be designed to support a tool changer such as a TIG welding torch in order to extend the welding process capabilities of the automated welding system.

Moreover, from a hardware perspective, the utilized cRIO controller is limited in terms of process memory and storage, and cannot be used in real-time machine vision applications, such as weld pool monitoring. Extending the capabilities of the technology developed in this thesis to accommodate real-time vision analysis during welding can optimize the welding quality and consistency of the welding result by adjusting the welding parameters

on the fly. To overcome this barrier, the integration of a high-performance PXI controller from National Instrument can provide extended computational resources, supporting at the same time the interconnection of the welding equipment, robotic motion and I/O between the welder and external control system.

The real-time external motion control module can generate, control, and deploy the robot kinematics, originating from the sensors' path planning approach. The motion can be optimized further by incorporating the dynamics of the robot, as such the generated currents from the servo motors and the weight of the attached tool, resulting in a smooth motion during sudden changes in speed and acceleration.

6.2.2. A Cost-Function Driven Adaptive Welding System for Multi-Pass Robotic Welding

Investigating a suitable methodology for root and hot pass welding parameters allocation can overcome the required input from the operator, complementing the welding sequence generation for the full V-groove geometry. This allocation of parameters could be generated from a learning model such us of a neural network for quality estimation of the welding procedure, based on laser scanning data of the root face, gap measurements and weld penetration depth for a variety of welding parameters. The proposed model should also consider irregularities that occur during bevelling and fitting of the parent plates prior to welding.

The procedure to identify the minimum value of the cost function for all the different weld instances can be optimized in terms of computation resource allocation, by incorporating

other methods, such as random and fuzzy logic instead of grid search, Bayesian and related Monte-Carlo. Nonetheless, other methods such as hill climbing and goal trees to identify the optimum solution, satisfying all the constraints based on the weighting of the cost function could be investigated [167,168].This requires the modelling of the probability distribution of the parameters that affect the optimum result and concentrating around this area of search. As a result, this advancement will benefit welding geometries that require numerous welding layers to fill the groove area, such as thick samples above 18 mm.

Additionally, the order in which the welding beads are deposited, which dictates distortion, should be investigated, and incorporated to avoid adverse effects on the structural integrity of the weldments. As such multiple welding trials and characterizations for varying groove geometries could be a key objective of future work.

Furthermore, the proposed approach will be extended further of single-sided V-grooves, to include different types of joints such as tee, lap corner and edge where multi-pass welding should be investigated. Therefore, this work of this thesis can be considered as the foundation of projecting the multi-pass welding procedure as a real problem in manufacturing through the automation of welding with the benefits it can offer.

6.2.3.   Towards Flexible and Automated Robotic Multi-Pass Arc Welding

The investigation and integration of a strategy to adapt the welding process per layer during welding will be a key to maximising the intelligence and flexibility of the automated welding system. Currently, the developed algorithms of the developed welding

system can adapt relative to the specimen in the scene and at the same time adapt its welding schedule relative to the geometric features of the groove. Bringing forward techniques such as weld pool monitoring for quality assessment of the integrity of the weld bead in real-time will further enhance the intelligence of the system and will minimize the risk for the formation of possible defects [140,169].

The developed technology can be extended to different types of weld joint configurations, following the investigation of offline sequence welding parameters generation conducted here. The laser scanning process should be extended to extract the groove characteristics of different geometries such as tee, lap, and edge configurations. In that way, the capability of the system to identify and adapt the welding process for different joints will benefit SMEs due to the high variation in specifications and low volume of products they handle.

Lastly, incorporating techniques that ensure avoidance of possible singularities that may arise due to the placement of the robot, the specimen or possible collision with fixtures will aid in the intelligence of the welding system to cooperate independently with minimal human supervision.

References

[1] UK Manufacturing Statistics, The Manufacturer. (n.d.). https://www.themanufacturer.com/uk-manufacturing-statistics/ (accessed April 5, 2022).

[2] PricewaterhouseCoopers, Annual Manufacturing Report 2020, PwC. (n.d.). https://www.pwc.co.uk/industries/manufacturing/insights/annual-manufacturing-report.html (accessed April 5, 2022).

[3] Welding Market Size, Share | Global Industry Growth, 2021-2028, (n.d.). https://www.fortunebusinessinsights.com/industry-reports/welding-market-101657 (accessed March 3, 2022).

[4] K. Weman, 23 - Welding costs, in: K. Weman (Ed.), Welding Processes Handbook (Second Edition), Woodhead Publishing, 2012: pp. 259–266. https://doi.org/10.1533/9780857095183.259.

[5] S. Pye, F.G.N. Li, J. Price, B. Fais, Achieving net-zero emissions through the reframing of UK national targets in the post-Paris Agreement era, Nat Energy. 2 (2017) 17024. https://doi.org/10.1038/nenergy.2017.24.

[6] A. Farkas, Impact of Industry 4.0 on robotic welding, IOP Conf. Ser.: Mater. Sci. Eng. 448 (2018) 012034. https://doi.org/10.1088/1757-899X/448/1/012034.

[7] What Industry 4.0 means to the welding department, (n.d.). https://www.thefabricator.com/thefabricator/article/arcwelding/what-industry-40-means-to-the-welding-department (accessed April 13, 2022).

[8]   M. Javaid, A. Haleem, R.P. Singh, S. Rab, R. Suman, Significance of sensors for industry 4.0: Roles, capabilities, and applications, Sensors International. 2 (2021) 100110. https://doi.org/10.1016/j.sintl.2021.100110.

[9]   Welding Products Market Size, Global Industry Report, 2020-2027, (n.d.). https://www.grandviewresearch.com/industry-analysis/global-welding-products-market (accessed April 13, 2022).

[10]   T.-J. Tarn, S.-B. Chen, C. Zhou, eds., Robotic welding, intelligence and automation, Springer, Berlin, 2007.

[11]   B. Kehoe, S. Patil, P. Abbeel, K. Goldberg, A Survey of Research on Cloud Robotics and Automation, IEEE Transactions on Automation Science and Engineering. 12 (2015) 398–409. https://doi.org/10.1109/TASE.2014.2376492.

[12]   R. Bogue, Cloud robotics: a review of technologies, developments and applications, Industrial Robot: An International Journal. 44 (2017) 1–5. https://doi.org/10.1108/IR-10-2016-0265.

[13]   S.B. Chen, T. Qiu, T. Lin, L. Wu, J.S. Tian, W.X. Lv, Y. Zhang, Intelligent Technologies for Robotic Welding, in: T.-J. Tarn, C. Zhou, S.-B. Chen (Eds.), Robotic Welding, Intelligence and Automation, Springer Berlin Heidelberg, 2004: pp. 123–143.

[14]   T. Lei, Y. Rong, H. Wang, Y. Huang, M. Li, A review of vision-aided robotic welding, Computers in Industry. 123 (2020) 103326. https://doi.org/10.1016/j.compind.2020.103326.

[15]   Welding Automation, (n.d.). https://www.twi-global.com/what-we-do/services-and-support/technical-support/welding-engineering/welding-automation/home.aspx (accessed April 13, 2022).

[16]   Z. Pan, J. Polden, N. Larkin, S.V. Duin, J. Norrish, Recent Progress on Programming Methods for Industrial Robots, in: ISR 2010 (41st International Symposium on Robotics) and ROBOTIK 2010 (6th German Conference on Robotics), 2010: pp. 1–8.

[17]   R. Halmshaw, Introduction to the non-destructive testing of welded joints, Woodhead Publishing, 1996.

[18]   A.S. Baskoro, D.A. Purwanto, A. Widyianto, Controlling the Width of Weld Bead from the Weld Pool Using Machine Vision and Artificial Neural Network, MATEC Web Conf. 269 (2019) 04003. https://doi.org/10.1051/matecconf/201926904003.

[19]   Y. Liu, Y. Zhang, Fusing machine algorithm with welder intelligence for adaptive welding robots, Journal of Manufacturing Processes. 27 (2017) 18–25. https://doi.org/10.1016/j.jmapro.2017.03.015.

[20]   R.M. Stern, A. Berlin, A. Fletcher, K. Hemminki, J. Jarvisalo, J. Peto, International conference on health hazards and biological effects of welding fumes and gases, Int. Arch Occup Environ Heath. 57 (1986) 237–246. https://doi.org/10.1007/BF00405791.

[21]   Babcock   International,   Babcock   International.   (n.d.). https://www.babcockinternational.com/what-we-do/marine/defence/facilities-and-infrastructure/our-facilities/ (accessed August 10, 2019).

[22]   HMS Iron Duke (F234) | Royal Navy, (n.d.). https://www.royalnavy.mod.uk/our-organisation/the-fighting-arms/surface-fleet/frigates/type-23/hms-iron-duke   (accessed May 2, 2022).

[23]   What is Welding? - Definition, Processes and Types of Welds, (n.d.). https://www.twi-global.com/technical-knowledge/faqs/what-is-welding.aspx   (accessed March 3, 2022).

[24]   R.W. Messler Jr, Principles of welding: processes, physics, chemistry, and metallurgy, John Wiley & Sons, 2008.

[25]   R. O'Brien, Welding handbook, vol. 2, American Welding Society. (1991).

[26]   What is Gas Metal Arc Welding? (MIG Welding / MAG Welding), (n.d.). https://www.twi-global.com/technical-knowledge/faqs/faq-what-is-mig-mag-welding.aspx (accessed November 10, 2020).

[27]   W. Savage, others, Joining of advanced materials, Elsevier, 2013.

[28]   C.D. Yang, H.Y. Huang, H.J. Zhang, Y.X. Chen, S.B. Chen, Multi-Pass Route Planning for Thick Plate of Low Alloy High Strength Steel by Double-Sided Double Arc Welding,   AMR.   590   (2012)   28–34. https://doi.org/10.4028/www.scientific.net/AMR.590.28.

[29]   M.G. Murch, Chapter 2 - Mechanised arc welding process options for pipework fabrications, in: W. Lucas (Ed.), Process Pipe and Tube Welding, Woodhead Publishing, 1991: pp. 21–34. https://doi.org/10.1533/9781845698881.21.

[30]   D. Lee, Robots in the shipbuilding industry, Robotics and Computer-Integrated Manufacturing. 30 (2014) 442–450. https://doi.org/10.1016/j.rcim.2014.02.002.

[31]   CEDEFOP, Skill shortages and gaps in European enterprises: Striking a balance between vocational education and training and the labour market, Publications Office Luxembourg, 2015.

[32]   W. Fricke, Fatigue analysis of welded joints: state of development, Marine Structures. 16 (2003) 185–200.

[33]   CaB System 300S/300M, (n.d.). https://www.esab.co.uk/gb/en/ (accessed November 24, 2020).

[34]   T.S. Hong, M. Ghobakhloo, W. Khaksar, 6.04 - Robotic Welding Technology, in: S. Hashmi, G.F. Batalha, C.J. Van Tyne, B. Yilbas (Eds.), Comprehensive Materials Processing, Elsevier, Oxford, 2014: pp. 77–99. https://doi.org/10.1016/B978-0-08-096532-1.00604-X.

[35]   Making the Cut with KUKA Robotics Corporation at FABTECH 2015 Chicago, (2015). https://www.businesswire.com/news/home/20151106005066/en/Making-the-Cut-with-KUKA-Robotics-Corporation-at-FABTECH-2015-Chicago (accessed November 24, 2020).

[36]   G. Giralt, R. Chatila, R. Alami, Remote intervention, robot autonomy, and teleprogramming: generic concepts and real-world application cases, in: Proceedings of 1993 IEEE/RSJ International Conference on Intelligent Robots and Systems (IROS '93), 1993: pp. 314–320 vol.1. https://doi.org/10.1109/IROS.1993.583117.

[37]   K. Xue, Z. Wang, J. Shen, S. Hu, Y. Zhen, J. Liu, D. Wu, H. Yang, Robotic seam tracking system based on vision sensing and human-machine interaction for multi-pass MAG welding, Journal of Manufacturing Processes. (2020). https://doi.org/10.1016/j.jmapro.2020.02.026.

[38]   J.J. Craig, Introduction to robotics: mechanics and control, 3/E, Pearson Education India, 2009.

[39]   O. Heimann, J. Guhl, Industrial Robot Programming Methods: A Scoping Review, in: 2020 25th IEEE International Conference on Emerging Technologies and Factory Automation   (ETFA),   2020:   pp.   696–703. https://doi.org/10.1109/ETFA46521.2020.9211997.

[40]   K. Fischer, F. Kirstein, L.C. Jensen, N. Krüger, K. Kukliński, M.V. aus der Wieschen, T.R. Savarimuthu, A comparison of types of robot control for programming by Demonstration, in: 2016 11th ACM/IEEE International Conference on Human-Robot Interaction (HRI), 2016: pp. 213–220. https://doi.org/10.1109/HRI.2016.7451754.

[41]   R.S. Andersen, S. Bøgh, T.B. Moeslund, O. Madsen, Intuitive task programming of stud welding robots for ship construction, in: 2015 IEEE International Conference on Industrial   Technology   (ICIT),   2015:   pp.   3302–3307. https://doi.org/10.1109/ICIT.2015.7125587.

[42]   G. Reinhart, U. Munzert, W. Vogl, A programming system for robot-based remote-laser-welding with conventional optics, CIRP Annals. 57 (2008) 37–40. https://doi.org/10.1016/j.cirp.2008.03.120.

[43]   M.F. Zaeh, W. Vogl, Interactive laser-projection for programming industrial robots, in: 2006 IEEE/ACM International Symposium on Mixed and Augmented Reality, 2006: pp. 125–128. https://doi.org/10.1109/ISMAR.2006.297803.

[44]   S. Mitsi, K.-D. Bouzakis, G. Mansour, D. Sagris, G. Maliaris, Off-line programming of an industrial robot for manufacturing, The International Journal of Advanced Manufacturing Technology. 26 (2005) 262–267.

[45]   S.I. Sagatun, K.E. Kjelstad, Robot Technology in the Shipyard Production Environment, Journal of Ship Production. 12 (1996) 39–48. https://doi.org/10.5957/jsp.1996.12.1.39.

[46]   N.J. Jacobsen, C.H. Jacobsen, GENERATING A JOB DESCRIPTION FOR MOTION PLANNING, IFAC Proceedings Volumes. 40 (2007) 24–29. https://doi.org/10.3182/20070523-3-ES-4908.00005.

[47]   Automatic robot welding | KRANENDONK, (n.d.). https://www.kranendonk.com/software/rinasweld (accessed January 23, 2021).

[48]   CAR-W |, (n.d.). https://www.wolfrobotics.com/equipment-technology/robot-software-solutions/auto-path-programming/ (accessed January 23, 2021).

[49]   DTPS III Desktop Programming & Simulation | Panasonic System Solutions Company of North America – Process Automation, (n.d.). https://www.panasonicfa.com/content/dtps-iii-desktop-programming-simulation (accessed January 23, 2021).

[50]   Model Predictive Visual Servoing of Fully-Actuated Underwater Vehicles With a Sliding Mode Disturbance Observer | IEEE Journals & Magazine | IEEE Xplore, (n.d.). https://ieeexplore.ieee.org/document/8649637 (accessed August 2, 2021).

[51]   F. Chaumette, S. Hutchinson, Visual servo control, Part I: Basic approaches, (2006) 10.

[52]   J. Li, Z. Chen, G. Rao, J. Xu, Structured Light-Based Visual Servoing for Robotic Pipe Welding Pose Optimization, IEEE Access. 7 (2019) 138327–138340. https://doi.org/10.1109/ACCESS.2019.2943248.

[53]   G. Chesi, K. Hashimoto, eds., Visual Servoing via Advanced Numerical Methods, Springer London, London, 2010. https://doi.org/10.1007/978-1-84996-089-2.

[54]   B. Espiau, Effect of camera calibration errors on visual servoing in robotics, in: T. Yoshikawa, F. Miyazaki (Eds.), Experimental Robotics III, Springer, Berlin, Heidelberg, 1994: pp. 182–192. https://doi.org/10.1007/BFb0027594.

[55]   V. Kyrki, D. Kragic, H.I. Christensen, Measurement errors in visual servoing, in: IEEE International Conference on Robotics and Automation, 2004. Proceedings. ICRA '04. 2004, 2004: pp. 1861-1867 Vol.2. https://doi.org/10.1109/ROBOT.2004.1308095.

[56]   B. Wang, S.J. Hu, L. Sun, T. Freiheit, Intelligent welding system technologies: State-of-the-art review and perspectives, Journal of Manufacturing Systems. 56 (2020) 373–391. https://doi.org/10.1016/j.jmsy.2020.06.020.

[57]   H. Zhang, H. Chen, N. Xi, G. Zhang, J. He, On-Line Path Generation for Robotic Deburring of Cast Aluminum Wheels, in: 2006 IEEE/RSJ International Conference on Intelligent Robots and Systems, 2006: pp. 2400–2405. https://doi.org/10.1109/IROS.2006.281679.

[58]   Z. Pan, H. Zhang, Robotic Machining from Programming to Process Control, (2008).

[59]   B. Solvang, G. Sziebig, P. Korondi, Robot Programming in Machining Operations, IntechOpen, 2008. https://doi.org/10.5772/6221.

[60]   A. Nicholson, Rapid adaptive programming using image data, University of Wollongong Thesis Collection 1954-2016. (2005). https://ro.uow.edu.au/theses/422.

[61]   E.J. Gonzalez-Galvan, A. Loredo-Flores, E.D. Laborico-Aviles, F. Pazos-Flores, J.J. Cervantes-Sanchez, An algorithm for optimal closed-path generation over arbitrary surfaces using uncalibrated vision, in: Proceedings 2007 IEEE International Conference on Robotics and Automation, 2007: pp. 2465–2470. https://doi.org/10.1109/ROBOT.2007.363689.

[62]   Z. Hu, C. Marshall, R. Bicker, P. Taylor, Automatic surface roughing with 3 D machine vision and cooperative robot control, Robotics and Autonomous Systems. 55 (2007) 552–560. https://doi.org/10.1016/j.robot.2007.01.005.

[63]   B. Takarics, P.T. Szemes, G. Nemeth, P. Korondi, Welding trajectory reconstruction based on the Intelligent Space concept, in: 2008 Conference on Human System Interactions, 2008: pp. 791–796. https://doi.org/10.1109/HSI.2008.4581542.

[64]   L. Yang, E. Li, T. Long, J. Fan, Z. Liang, A Novel 3-D Path Extraction Method for Arc Welding Robot Based on Stereo Structured Light Sensor, IEEE Sensors Journal. 19 (2019) 763–773. https://doi.org/10.1109/JSEN.2018.2877976.

[65]   P. Maiolino, R. Woolley, D. Branson, P. Benardos, A. Popov, S. Ratchev, Flexible robot sealant dispensing cell using RGB-D sensor and off-line programming, Robotics and Computer-Integrated Manufacturing. 48 (2017) 188–195. https://doi.org/10.1016/j.rcim.2017.04.004.

[66]   A. Rout, B.B.V.L. Deepak, B.B. Biswal, Advances in weld seam tracking techniques for robotic welding: A review, Robotics and Computer-Integrated Manufacturing. 56 (2019) 12–37. https://doi.org/10.1016/j.rcim.2018.08.003.

[67]   P. Kah, M. Shrestha, E. Hiltunen, J. Martikainen, Robotic arc welding sensors and programming in industrial applications, Int J Mech Mater Eng. 10 (2015) 13. https://doi.org/10.1186/s40712-015-0042-y.

[68]   W.P. Gu, Z.Y. Xiong, W. Wan, Autonomous seam acquisition and tracking system for multi-pass welding based on vision sensor, Int J Adv Manuf Technol. 69 (2013) 451–460. https://doi.org/10.1007/s00170-013-5034-6.

[69]   J. Sun, G. Cao, S. Huang, K. Chen, J. Yang, Welding seam detection and feature point extraction for robotic arc welding using laser-vision, in: 2016 13th International Conference on Ubiquitous Robots and Ambient Intelligence (URAI), 2016: pp. 644–647. https://doi.org/10.1109/URAI.2016.7625795.

[70]   J. Muhammad, H. Altun, E. Abo-Serie, Welding seam profiling techniques based on active vision sensing for intelligent robotic welding, The International Journal of Advanced Manufacturing Technology. 88 (2017) 127–145. https://doi.org/10.1007/s00170-016-8707-0.

[71]   A. Zych, Programming of Welding Robots in Shipbuilding, Procedia CIRP. 99 (2021) 478–483. https://doi.org/10.1016/j.procir.2021.03.107.

[72]   N.R. Nayak, A. Ray, Intelligent seam tracking for robotic welding, Springer Science & Business Media, 2013.

[73]   J. Le, H. Zhang, X. Chen, Right-angle fillet weld tracking by robots based on rotating arc sensors in GMAW, Int J Adv Manuf Technol. 93 (2017) 605–616. https://doi.org/10.1007/s00170-017-0536-2.

[74]   V. Shelyagin, I. Zaitsev, A. Bernatskyi, V. Sydorets, A. Dubko, O. Bondarenko, Contactless monitoring of welding processes with computer processing of acoustic emission signals, in: 2018 14th International Conference on Advanced Trends in Radioelecrtronics, Telecommunications and Computer Engineering (TCSET), 2018: pp. 706–710. https://doi.org/10.1109/TCSET.2018.8336298.

[75]   Y. Shi, G. Zhang, C. Li, Y. Gu, D. Fan, Weld pool oscillation frequency in pulsed gas tungsten arc welding with varying weld penetration, in: 2015 IEEE International Conference on Automation Science and Engineering (CASE), 2015: pp. 401–406. https://doi.org/10.1109/CoASE.2015.7294111.

[76]   S. Wei, H. Ma, T. Lin, S. Chen, Autonomous guidance of initial welding position with "single camera and double positions" method, Sensor Review; Bradford. 30 (2010) 62–68. http://dx.doi.org/10.1108/02602281011010808.

[77]   K. Micallef, G. Fang, M. Dinham, Automatic Seam Detection and Path Planning in Robotic Welding, in: T.-J. Tarn, S.-B. Chen, G. Fang (Eds.), Robotic Welding, Intelligence and Automation, Springer Berlin Heidelberg, 2011: pp. 23–32.

[78]   M. Dinham, G. Fang, Autonomous weld seam identification and localisation using eye-in-hand stereo vision for robotic arc welding, Robotics and Computer-Integrated Manufacturing. 29 (2013) 288–301. https://doi.org/10.1016/j.rcim.2013.01.004.

[79]   M. Dinham, G. Fang, Weld seam detection using computer vision for robotic Arc Welding, in: 2012 IEEE International Conference on Automation Science and Engineering (CASE), 2012: pp. 771–776. https://doi.org/10.1109/CoASE.2012.6386339.

[80]   J.G.D.M. Franca, M.A. Gazziro, A.N. Ide, J.H. Saito, A 3D scanning system based on laser triangulation and variable field of view, in: IEEE International Conference on Image Processing 2005, 2005: p. I–425. https://doi.org/10.1109/ICIP.2005.1529778.

[81]   Z.Y. Zhu, T. Lin, Y.J. Piao, S.B. Chen, Recognition of the initial position of weld based on the image pattern match technology for welding robot, Int J Adv Manuf Technol. 26 (2005) 784–788. https://doi.org/10.1007/s00170-003-2053-8.

[82]   M. Kong, F. Shi, S. Chen, T. Lin, Recognition of the initial position of weld based on the corner detection for welding robot in global environment, in: Robotic Welding, Intelligence and Automation, Springer, 2007: pp. 249–255.

[83]   S.B. Chen, X.Z. Chen, T. Qiu, J.Q. Li, Acquisition of Weld Seam Dimensional Position Information for Arc Welding Robot Based on Vision Computing, J Intell Robot Syst. 43 (2005) 77–97. https://doi.org/10.1007/s10846-005-2966-6.

[84]   Y. Xu, H. Yu, J. Zhong, T. Lin, S. Chen, Real-time seam tracking control technology during welding robot GTAW process based on passive vision sensor, Journal of Materials Processing Technology. 212 (2012) 1654–1662. https://doi.org/10.1016/j.jmatprotec.2012.03.007.

[85]   Y. He, Y. Xu, Y. Chen, H. Chen, S. Chen, Weld seam profile detection and feature point extraction for multi-pass route planning based on visual attention model, Robotics and Computer-Integrated Manufacturing. 37 (2016) 251–261. https://doi.org/10.1016/j.rcim.2015.04.005.

[86]   J.-J. Yang, K.-H. Wang, T.-L. Wu, A.-M. Wei, Image Feature Analysis of Weld Pool in Aluminium Alloy Twin Arc PMIG Welding Based on Snake Model, in: T.-J. Tarn, S.-B. Chen, X.-Q. Chen (Eds.), Robotic Welding, Intelligence and Automation, Springer International Publishing, Cham, 2015: pp. 303–309. https://doi.org/10.1007/978-3-319-18997-0_26.

[87]   J. Zhong, C. Yang, Y. Xu, H. Chen, S. Chen, Research on Reconstruction of Weld Pool Surface Based on Shape from Shading During Robot Aluminum Alloy Pulse GTAW, in: T.-J. Tarn, S.-B. Chen, X.-Q. Chen (Eds.), Robotic Welding, Intelligence and Automation, Springer International Publishing, Cham, 2015: pp. 525–538. https://doi.org/10.1007/978-3-319-18997-0_45.

[88]   J.J. Wang, T. Lin, S.B. Chen, Obtaining weld pool vision information during aluminium alloy TIG welding, Int J Adv Manuf Technol. 26 (2005) 219–227. https://doi.org/10.1007/s00170-003-1548-7.

[89]   H. Dong, M. Cong, Y. Zhang, Y. Liu, H. Chen, Modeling and real-time prediction for complex welding process based on weld pool, Int J Adv Manuf Technol. 96 (2018) 2495–2508. https://doi.org/10.1007/s00170-018-1685-7.

[90]   J. Forest, J. Salvi, E. Cabruja, C. Pous, Laser stripe peak detector for 3D scanners. A FIR filter approach, in: Proceedings of the 17th International Conference on Pattern Recognition, 2004. ICPR 2004., IEEE, 2004: pp. 646–649.

[91]   M. Dinham, G. Fang, J.J. Zou, Experiments on Automatic Seam Detection for a MIG Welding Robot, in: H. Deng, D. Miao, J. Lei, F.L. Wang (Eds.), Artificial Intelligence and Computational Intelligence, Springer Berlin Heidelberg, 2011: pp. 390–397.

[92]   A. Ryberg, M. Ericsson, A.-K. Christiansson, K. Eriksson, J. Nilsson, M. Larsson, Stereo vision for path correction in off-line programmed robot welding, in: 2010 IEEE International Conference on Industrial Technology, 2010: pp. 1700–1705. https://doi.org/10.1109/ICIT.2010.5472442.

[93]   Z. Ye, F. Gu, S. Chen, M. Dinham, A robust algorithm for weld seam extraction based on prior knowledge of weld seam, Sensor Review; Bradford. 33 (2013) 125–133. http://dx.doi.org/10.1108/02602281311299662.

[94]   Y. Xu, G. Fang, S. Chen, J.J. Zou, Z. Ye, Real-time image processing for vision-based weld seam tracking in robotic GMAW, Int J Adv Manuf Technol. 73 (2014) 1413–1425. https://doi.org/10.1007/s00170-014-5925-1.

[95]   Robotics: Joint Sensing Technologies | Lincoln Electric, Lincolnelectric. (n.d.). http://www.lincolnelectric.com/en-gb/support/process-and-theory/Pages/intelligent-robotic-detail.aspx (accessed June 21, 2019).

[96]   R.P. Manorathna, P. Phairatt, P. Ogun, T. Widjanarko, M. Chamberlain, L. Justham, S. Marimuthu, M.R. Jackson, Feature extraction and tracking of a weld joint for adaptive robotic welding, in: 2014 13th International Conference on Control Automation Robotics Vision (ICARCV), 2014: pp. 1368–1372. https://doi.org/10.1109/ICARCV.2014.7064515.

[97]   P. Manorathna, P. Ogun, S. Marimuthu, L. Justham, M. Jackson, Performance evaluation of a three dimensional laser scanner for industrial applications, in: 7th International Conference on Information and Automation for Sustainability, 2014: pp. 1–6. https://doi.org/10.1109/ICIAFS.2014.7069534.

[98]   ARC | EYE - Laser Vision Systems, (n.d.). http://arc-eye.com/ (accessed June 27, 2019).

[99]   Smart Laser Vision Systems for Smart Robots, (n.d.). https://servo-robot.com/ (accessed June 27, 2019).

[100]   Home | Metavision, (n.d.). https://meta-vs.com/ (accessed June 27, 2019).

[101] Liburdi Automation - Custom Engineered Welding Systems, (n.d.). https://www.liburdi.com/welding-systems-automation-custom-engineered-systems-seam-tracker (accessed June 27, 2019).

[102] Wise Welding, (n.d.). http://www.wise-t.com/product-wise-welding.php?lng=en (accessed June 27, 2019).

[103] M. Dinham, G. Fang, A low cost hand-eye calibration method for arc welding robots, in: 2009 IEEE International Conference on Robotics and Biomimetics (ROBIO), IEEE, Guilin, China, 2009: pp. 1889–1893. https://doi.org/10.1109/ROBIO.2009.5420552.

[104] Y. Zou, X. Chen, Hand–eye calibration of arc welding robot and laser vision sensor through semidefinite programming, Industrial Robot: An International Journal. 45 (2018) 597–610. https://doi.org/10.1108/IR-02-2018-0034.

[105] Q. Zhan, X. Wang, Hand–eye calibration and positioning for a robot drilling system, Int J Adv Manuf Technol. 61 (2012) 691–701. https://doi.org/10.1007/s00170-011-3741-4.

[106] W. Li, H. Xie, G. Zhang, S. Yan, Z. Yin, Hand–Eye Calibration in Visually-Guided Robot Grinding, IEEE Transactions on Cybernetics. 46 (2016) 2634–2642. https://doi.org/10.1109/TCYB.2015.2483740.

[107] A. Malti, J.P. Barreto, Robust hand-eye calibration for computer aided medical endoscopy, in: 2010 IEEE International Conference on Robotics and Automation, 2010: pp. 5543–5549. https://doi.org/10.1109/ROBOT.2010.5509331.

[108]   R.Y. Tsai, R.K. Lenz, A new technique for fully autonomous and efficient 3D robotics hand/eye calibration, IEEE Transactions on Robotics and Automation. 5 (1989) 345–358. https://doi.org/10.1109/70.34770.

[109]   R. Tsai, A versatile camera calibration technique for high-accuracy 3D machine vision metrology using off-the-shelf TV cameras and lenses, IEEE Journal on Robotics and Automation. 3 (1987) 323–344. https://doi.org/10.1109/JRA.1987.1087109.

[110]   Z. Zhang, A flexible new technique for camera calibration, IEEE Transactions on Pattern Analysis and Machine Intelligence. 22 (2000) 1330–1334. https://doi.org/10.1109/34.888718.

[111]   Introduction to Destructive Weld Testing | ESAB Knowledge Center, (n.d.). https://www.esabna.com/us/en/education/blog/destructive-testing-of-welds.cfm (accessed March 10, 2022).

[112]   ISO 5817:2014(en), Welding — Fusion-welded joints in steel, nickel, titanium and their alloys (beam welding excluded) — Quality levels for imperfections, (n.d.). https://www.iso.org/obp/ui/#iso:std:iso:5817:ed-3:v1:en (accessed July 3, 2019).

[113] MODUK - DEF STAN 02-773 - Minimum Non-Destructive Examination Acceptance Standards for Welds in HM Submarines and Surface Ships not in Class | Engineering360,   (n.d.). https://standards.globalspec.com/std/1609364/DEF%20STAN%2002-773 (accessed July 3, 2019).

[114] 5.2 Angle Beam Inspection | Olympus IMS, (n.d.). https://www.olympus-ims.com/en/ndt-tutorials/flaw-detection/weld-inspection/ (accessed March 11, 2022).

[115] C. Mineo, C. MacLeod, M. Morozov, S.G. Pierce, T. Lardner, R. Summan, J. Powell, P. McCubbin, C. McCubbin, G. Munro, S. Paton, D. Watson, D. Lines, Fast ultrasonic phased array inspection of complex geometries delivered through robotic manipulators and high speed data acquisition instrumentation, in: 2016 IEEE International Ultrasonics Symposium (IUS), IEEE, Tours, France, 2016: pp. 1–4. https://doi.org/10.1109/ULTSYM.2016.7728746.

[116] Y. Javadi, C.N. MacLeod, S.G. Pierce, A. Gachagan, D. Lines, C. Mineo, J. Ding, S. Williams, M. Vasilev, E. Mohseni, R. Su, Ultrasonic phased array inspection of a Wire + Arc Additive Manufactured (WAAM) sample with intentionally embedded defects, Additive Manufacturing. 29 (2019) 100806. https://doi.org/10.1016/j.addma.2019.100806.

[117] Final Report Summary - MARWIN (Decision making and augmented reality support for automatic welding installations) | Report Summary | MARWIN | FP7-SME | CORDIS | European Commission, (n.d.). https://cordis.europa.eu/project/rcn/101118/reporting/en (accessed February 15, 2019).

[118] Intelligent Robotic Welding Systems for Unique Fabrications | HEPHAESTOS Project | FP2, CORDIS | European Commission. (n.d.). https://cordis.europa.eu/project/id/5369 (accessed January 25, 2021).

[119] Industry KUKA brochure_arc_welding.pdf, (n.d.). https://www.kuka.com/-/media/kuka-downloads/imported/9cb8e311bfd744b4b0eab25ca883f6d3/industry_brochure_arc_welding_en.pdf?rev=d93af2560d294ad5b61fefd8f3c018f0&hash=4CC0E64038CD11CF19E6C7C7979F3884 (accessed May 24, 2022).

[120] Robot simulator CoppeliaSim: create, compose, simulate, any robot - Coppelia Robotics, (n.d.). https://www.coppeliarobotics.com/ (accessed March 2, 2022).

[121] Simulator for industrial robots and offline programming - RoboDK, (n.d.). https://robodk.com/ (accessed March 2, 2022).

[122] Process and Control Today | A comparison of blue and red light sensor technology: which one is best for your application?, (n.d.). https://www.pandct.com/news/a-comparison-of-blue-and-red-light-sensor-technology-which-one-is-best-for-your-application/ (accessed May 24, 2022).

[123] M.-E.M.- info@micro-epsilon.de, Blue Laser triangulation sensors for difficult surface types, Micro-Epsilon Messtechnik. (n.d.). https://www.micro-epsilon.co.uk (accessed May 24, 2022).

[124] mohr, ProPuls, JESS WELDING. (2020). https://www.jess-welding.com/portfolio/propuls/ (accessed April 11, 2022).

[125] T. Era, T. Ueyama, Spatter reduction in GMAW by current waveform control, Welding International. 21 (2007) 496–501. https://doi.org/10.1080/09507110701579647.

[126] S.H. Lee, J.S. Kim, B.Y. Lee, S.Y. Lee, The Effect of External Electromagnetic Force in Gas Metal Arc Welding on the Transfer Mode, Key Engineering Materials. 297–300 (2005) 2825–2830. https://doi.org/10.4028/www.scientific.net/KEM.297-300.2825.

[127] Z. Wang, D. Jiang, J. Wu, M. Xu, A review on high-frequency pulsed arc welding, Journal of Manufacturing Processes. 60 (2020) 503–519. https://doi.org/10.1016/j.jmapro.2020.10.054.

[128] NI-9263 - National Instruments, (n.d.). https://www.ni.com/en-gb/support/model.ni-9263.html (accessed July 24, 2019).

[129] NI-9205 - National Instruments, (n.d.). https://www.ni.com/en-gb/support/model.ni-9205.html (accessed July 24, 2019).

[130] NI-9476 - National Instruments, (n.d.). https://www.ni.com/en-gb/support/model.ni-9476.html (accessed July 24, 2019).

[131] NI-9425 - National Instruments, (n.d.). https://www.ni.com/en-gb/support/model.ni-9425.html (accessed July 24, 2019).

[132] What is LabVIEW?, (n.d.). https://www.ni.com/en-gb/shop/labview.html (accessed February 26, 2022).

[133] JKI, JKI State Machine for LabVIEW, (n.d.). https://resources.jki.net/state-machine (accessed February 26, 2022).

[134] KUKA.RobotSensorInterface, KUKA AG. (n.d.). https://www.kuka.com/en-gb/products/robotics-systems/software/application-software/kuka_robotsensorinterface (accessed February 26, 2022).

[135] C. Mineo, M. Vasilev, B. Cowan, C.N. MacLeod, S.G. Pierce, C. Wong, E. Yang, R. Fuentes, E.J. Cross, Enabling robotic adaptive behaviour capabilities for new Industry 4.0 automated quality inspection paradigms, Insight. 62 (2020) 338–344. https://doi.org/10.1784/insi.2020.62.6.338.

[136] M. Vasilev, C.N. MacLeod, C. Loukas, Y. Javadi, R.K.W. Vithanage, D. Lines, E. Mohseni, S.G. Pierce, A. Gachagan, Sensor-Enabled Multi-Robot System for Automated Welding and In-Process Ultrasonic NDE, Sensors. 21 (2021) 5077. https://doi.org/10.3390/s21155077.

[137] S.-B. Chen, J. Wu, Real-Time Control of Weld Pool Dynamics During Robotic GTAW, in: Intelligentized Methodology for Arc Welding Dynamical Processes, Springer Berlin Heidelberg, Berlin, Heidelberg, 2009: pp. 221–273. https://doi.org/10.1007/978-3-540-85642-9_6.

[138] R.K.W. Vithanage, E. Mohseni, Z. Qiu, C. MacLeod, Y. Javadi, N. Sweeney, G. Pierce, A. Gachagan, A Phased Array Ultrasound Roller Probe for Automated in-Process/Interpass Inspection of Multipass Welds, IEEE Transactions on Industrial Electronics. 68 (2021) 12781–12790. https://doi.org/10.1109/TIE.2020.3042112.

[139] M. Myhr, Industrial new trends: ABB view of the future, in: International Workshop on Industrial Robotics, New Trends and Perspectives (Http://Robotics. Dem. Uc. Pt/Ir99/), Parque Das Nações, Lisbon, 1999.

[140] Y.M. Zhang, R. Kovacevic, L. Li, Adaptive control of full penetration gas tungsten arc welding, IEEE Transactions on Control Systems Technology. 4 (1996) 394–403. https://doi.org/10.1109/87.508887.

[141] C. Doumanidis, Y.-M. Kwak, Multivariable adaptive control of the bead profile geometry in gas metal arc welding with thermal scanning, International Journal of Pressure Vessels and Piping. 79 (2002) 251–262. https://doi.org/10.1016/S0308-0161(02)00024-8.

[142] L. Na, S. Chen, Q. Chen, W. Tao, H. Zhao, S. Chen, Dynamic welding process monitoring based on microphone array technology, Journal of Manufacturing Processes. 64 (2021) 481–492. https://doi.org/10.1016/j.jmapro.2020.12.023.

[143] C. Yang, Z. Ye, Y. Chen, J. Zhong, S. Chen, Multi-pass path planning for thick plate by DSAW based on vision sensor, Sensor Review. 34 (2014) 416–423. https://doi.org/10.1108/SR-04-2013-649.

[144] T.-Y. Huang, L.-W. Fan, Y.-N. Bao, H. Shi, K. Zhang, Multi-pass Route Planning for Thick Steel Plate Using Laser Welding with Filler Wire, in: T.-J. Tarn, S.-B. Chen, X.-Q. Chen (Eds.), Robotic Welding, Intelligence and Automation, Springer International Publishing, Cham, 2015: pp. 551–560. https://doi.org/10.1007/978-3-319-18997-0_47.

[145] H. Zhang, H. Lu, C. Cai, S. Chen, Robot Path Planning in Multi-pass Weaving Welding for Thick Plates, in: T.-J. Tarn, S.-B. Chen, G. Fang (Eds.), Robotic Welding, Intelligence and Automation, Springer, Berlin, Heidelberg, 2011: pp. 351–359. https://doi.org/10.1007/978-3-642-19959-2_43.

[146] S.J. Yan, S.K. Ong, A.Y.C. Nee, Optimal Pass Planning for Robotic Welding of Large-dimension Joints with Deep Grooves, Procedia CIRP. 56 (2016) 188–192. https://doi.org/10.1016/j.procir.2016.10.052.

[147] T.-L. Teng, P.-H. Chang, W.-C. Tseng, Effect of welding sequences on residual stresses, Computers & Structures. 81 (2003) 273–286. https://doi.org/10.1016/S0045-7949(02)00447-9.

[148] C. Heinze, C. Schwenk, M. Rethmeier, Numerical calculation of residual stress development of multi-pass gas metal arc welding, Journal of Constructional Steel Research. 72 (2012) 12–19. https://doi.org/10.1016/j.jcsr.2011.08.011.

[149] A. Erhard, G. Schenk, Th. Hauser, U. Völz, New applications using phased array techniques, Nuclear Engineering and Design. 206 (2001) 325–336. https://doi.org/10.1016/S0029-5493(00)00419-2.

[150] N.T. Burgess, Quality Assurance of Welded Construction., Routledge, Hoboken, 1989. http://public.ebookcentral.proquest.com/choice/publicfullrecord.aspx?p=242049 (accessed October 26, 2020).

[151] Global welder shortage – insight from three continents, Welding Value. (2020). https://weldingvalue.com/2020/11/global-welder-shortage-viewpoints-three-continents/ (accessed July 26, 2021).

[152] B. Reed, What Is the Welder Shortage and How Is It Impacting Businesses?, Summit Steel & Manufacturing, Inc. (2021). https://www.summitsteelinc.com/resources/blog/welder-shortage-impact/ (accessed July 26, 2021).

[153] M. Rajaraman, M. Dawson-Haggerty, K. Shimada, D. Bourne, Automated workpiece localization for robotic welding, in: 2013 IEEE International Conference on Automation Science and Engineering (CASE), 2013: pp. 681–686. https://doi.org/10.1109/CoASE.2013.6654062.

[154] K.T. Gunnarsson, F.B. Prinz, CAD Model-Based Localization of Parts in Manufacturing, Computer. 20 (1987) 66–74. https://doi.org/10.1109/MC.1987.1663663.

[155] Z.H. Xiong, Y.X. Chu, G.F. Liu, Z.X. Li, Workpiece localization and computer aided setup system, in: Proceedings 2001 IEEE/RSJ International Conference on Intelligent Robots and Systems. Expanding the Societal Role of Robotics in the the Next Millennium (Cat. No.01CH37180), 2001: pp. 1141–1146 vol.2. https://doi.org/10.1109/IROS.2001.976322.

[156] G. Schleth, A. Kuss, W. Kraus, Workpiece localization methods for robotic welding - a review, in: ISR 2018; 50th International Symposium on Robotics, 2018: pp. 1–6.

[157] E.B. Njaastad, O. Egeland, Automatic Touch-Up of Welding Paths Using 3D Vision, IFAC-PapersOnLine. 49 (2016) 73–78. https://doi.org/10.1016/j.ifacol.2016.12.164.

[158] A. Kuss, U. Schneider, T. Dietz, A. Verl, Detection of Assembly Variations for Automatic Program Adaptation in Robotic Welding Systems, in: Proceedings of ISR 2016: 47st International Symposium on Robotics, 2016: pp. 1–6.

[159] C.-H. Wu, S.-Y. Jiang, K.-T. Song, CAD-based pose estimation for random bin-picking of multiple objects using a RGB-D camera, in: 2015 15th International Conference on Control, Automation and Systems (ICCAS), 2015: pp. 1645–1649. https://doi.org/10.1109/ICCAS.2015.7364621.

[160] Ø. Skotheim, M. Lind, P. Ystgaard, S.A. Fjerdingen, A flexible 3D object localization system for industrial part handling, in: 2012 IEEE/RSJ International Conference on Intelligent Robots and Systems, 2012: pp. 3326–3333. https://doi.org/10.1109/IROS.2012.6385508.

[161] F. Spenrath, M. Palzkill, A. Pott, A. Verl, Object recognition: Bin-picking for industrial use, in: IEEE ISR 2013, 2013: pp. 1–3. https://doi.org/10.1109/ISR.2013.6695743.

[162] J.J. Rodrigues, J.-S. Kim, M. Furukawa, J. Xavier, P. Aguiar, T. Kanade, 6D pose estimation of textureless shiny objects using random ferns for bin-picking, in: 2012 IEEE/RSJ International Conference on Intelligent Robots and Systems, 2012: pp. 3334–3341. https://doi.org/10.1109/IROS.2012.6385680.

[163] F. Vanegas, F. Gonzalez, Enabling UAV Navigation with Sensor and Environmental Uncertainty in Cluttered and GPS-Denied Environments, Sensors. 16 (2016) 666. https://doi.org/10.3390/s16050666.

[164] G. Zhenglong, F. Qiang, Q. Quan, Pose Estimation for Multicopters Based on Monocular Vision and AprilTag, in: 2018 37th Chinese Control Conference (CCC), 2018: pp. 4717–4722. https://doi.org/10.23919/ChiCC.2018.8483685.

[165] M. Kalaitzakis, B. Cain, S. Carroll, A. Ambrosi, C. Whitehead, N. Vitzilaios, Fiducial Markers for Pose Estimation, J Intell Robot Syst. 101 (2021) 71. https://doi.org/10.1007/s10846-020-01307-9.

[166] X.-S. Gao, X.-R. Hou, J. Tang, H.-F. Cheng, Complete solution classification for the perspective-three-point problem, IEEE Transactions on Pattern Analysis and Machine Intelligence. 25 (2003) 930–943. https://doi.org/10.1109/TPAMI.2003.1217599.

[167] T. Jurgenson, O. Avner, E. Groshev, A. Tamar, Sub-Goal Trees a Framework for Goal-Based Reinforcement Learning, in: Proceedings of the 37th International Conference on Machine Learning, PMLR, 2020: pp. 5020–5030. https://proceedings.mlr.press/v119/jurgenson20a.html (accessed September 9, 2022).

[168] B. Selman, C.P. Gomes, Hill-climbing Search, in: L. Nadel (Ed.), Encyclopedia of Cognitive Science, John Wiley & Sons, Ltd, Chichester, 2006: p. s00015. https://doi.org/10.1002/0470018860.s00015.

[169]   Y.K. Liu, Y.M. Zhang, Model-Based Predictive Control of Weld Penetration in Gas Tungsten Arc Welding, IEEE Transactions on Control Systems Technology. 22 (2014) 955–966. https://doi.org/10.1109/TCST.2013.2266662.